NASA TECHNICAL MEMORANDUM

NASA TM X-73,130

NASA TM X- 73,130

MULTI-STAR PROCESSING AND GYRO FILTERING FOR THE VIDEO INERTIAL POINTING SYSTEM

James Patrick Murphy

Ames Research Center
Moffett Field, California 94035

June 1976

1. Report No.	2. Government Accession No.	3. Recipient's Catalog No.
NASA TM X-73,130		

4. Title and Subtitle	5. Report Date
MULTI-STAR PROCESSING AND GYRO FILTERING FOR THE VIDEO INERTIAL POINTING SYSTEM*	6. Performing Organization Code
7. Author(s)	8. Performing Organization Report No
James Patrick Murphy	A-6595
9. Performing Organization Name and Address	10. Work Unit No
Ames Research Center Moffett Field, California 94035	506-19-15
	11. Contract or Grant No.
12. Sponsoring Agency Name and Address	13. Type of Report and Period Covered
National Aeronautics and Space Administration Washington, D. C. 20546	Technical Memorandum
	14. Sponsoring Agency Code

15. Supplementary Notes

*Thesis submitted to the Dept. of Applied Mechanics, Stanford University, for the degree of Engineer.

16. Abstract

The video inertial pointing (VIP) system is being developed at the Ames Research Center, NASA (Moffett Field, California) to satisfy the acquisition and pointing requirements of astronomical telescopes. VIP uses a single video sensor to provide star position information that can be used to generate three-axis pointing error signals (multi-star processing) and for input to a cathode ray tube (CRT) display of the star field. The pointing error signals are used to update the telescope's gyro stabilization system (gyro filtering). The CRT display facilitates target acquisition and positioning of the telescope by a remote operator.

This work develops and analyzes equations that can be used for the multi-star processing and develops and evaluates a design approach for the gyro filtering. Linearized small angle equations are used for the multi-star processing and a consideration of error performance and singularities leads to star pair location restrictions and equation selection criteria. A discrete steady-state Kalman filter which uses the integration of the gyros is developed and analyzed. The filter includes unit time delays representing asynchronous operations of the VIP microprocessor and video sensor. A digital simulation of a typical gyro stabilized gimbal is developed and used to validate the approach taken to the gyro filtering.

17. Key Words (Suggested by Author(s))	18. Distribution Statement
Spacecraft design Testing and performance	Unlimited STAR Category - 18

19. Security Classif. (of this report)	20. Security Classif. (of this page)	21. No. of Pages	22. Price*
Unclassified	Unclassified	124	$5.25

*For sale by the National Technical Information Service, Springfield, Virginia 22161

TABLE OF CONTENTS

LIST OF SYMBOLS

A	attitude error distribution matrix
D	gyro drift
D_N	covariance of drift rate noise
$E[\ ]$	expected value
$e(t_i)$	gyro filter error
$G(S)$	gyro filter compensation transfer function
G_D	gyro drift
H	measurement matrix
$H(s)$	gyro stabilization compensation transfer function
k_i	ith gyro filter gain
M_θ	pitch or yaw filtered attitude estimate prior to update
N	number of guide star pairs
P	attitude error covariance matrix
P_θ	pitch or yaw filtered attitude estimate at update
Q_d	covariance of gyro attitude noise
Q_g	covariance of gyro rate noise
R	attitude measurement noise covariance matrix
S	Laplace transform
T	gyro filter update cycle time
T_d	torque disturbance
T_{VIP}	VIP microprocessor cycle time
T_{VSI}	video sensor integration time
$u(t_i)$	discrete control input
$v(t_i)$	measurement noise
$v_{i,i\ odd}$	noise in Δx_i measurement
$v_{i,i\ even}$	noise in Δy_i measurement
v_{so}	video sensor simulated output

$w(t_i)$	discrete noise input
x	state vector
x_i	ith star x coordinates
Δx_i	$\Delta x_i \triangleq x_T - x_I$ star i
x_{io}	$x_{io} \triangleq x_I$ star i
$y(t_i)$	attitude measurement
y_i	ith star y coordinate
Δy_i	$\Delta y_i \triangleq y_T - y_I$ star i
y_{io}	$y_{io} \triangleq y_I$ star i
Z	Z-transform
Γ_1	discrete input distribution matrix (control)
Γ_2	discrete input distribution matrix (noise)
Δt	simulation integration period
ε	gyro filter coupling
$\varepsilon_{\theta r,\theta p,\theta y}$	roll, pitch, and yaw attitude error standard deviations
θ	pitch or yaw attitude
$\hat{\theta}$	gyro filter output
θ_b	pitch or yaw joystick bias
θ_I	video sensor integrated attitude
θ_N	attitude measurement noise
$\theta r,\theta p,\theta y$	roll, pitch, and yaw attitude errors
$\hat{\theta}r,\hat{\theta}p,\hat{\theta}y$	best estimate of roll, pitch, and yaw attitude errors
θ_s	delayed (one unit) pitch or yaw attitude
θ_{s1}	delayed (first unit) pitch or yaw attitude
θ_{s2}	delayed (second unit) pitch or yaw attitude
σ	standard deviation of x_i or y_i
ϕ	state transition matrix

X	gyro rate noise covariance for simulation
ω	pitch or yaw attitude rate
ω_g	$\omega_g \triangleq \omega + \omega_{gN}$
ω_{gN}	gyro rate noise
$[\ ]_T$	telescope actual pointing position in vector basis aligned to desired pointing position
$[\ ]_I$	star position in vector basis aligned to desired pointing position

CHAPTER I. INTRODUCTION

A. The Video Inertial Pointing System

The video inertial pointing (VIP) system had its origin in the infrared (IR) astronomy program being conducted at the Ames Research Center, NASA, Moffett Field, California. In the VIP concept, a video sensor is used to provide data for the generation of pointing error signals and for a cathode ray tube (CRT) display of the star field. The CRT display significantly improves the operator/astronomer interaction with the remotely controlled telescope. Because balloon-borne, airborne, or space-borne telescopes are typically gyro stabilized, the pointing error signals are used to update the basic gyro stabilization; hence the term video inertial pointing.

The system concept was originated by Mr. Charles D. Swift of Ames Research Center for use with a balloon-borne IR telescope. This early version of the VIP system [1] consisted of a silicon intensified target (SIT) vidicon boresighted to the telescope. On-board electronics were used to select the 10 brightest stars in the field of view of the SIT vidicon for transmission to the ground station and CRT display. In the ground station, the operator was able to select one guide star for automatic pointing. A joystick was used to surround the selected guide star with cross hairs that had an adjustable deadband. Telemetry was used to adjust the center position and deadband of the cross hairs in the on-board electronics. A coincidence detector determined if the star was in the cross hair deadband. If the star was within the deadband, no command was sent to the gyro stabilization; if the star was outside the deadband, a fixed torquing current was sent to the appropriate gyro to recenter the star. During automatic pointing, the joystick

could be used to move the cross hair position and thereby introduce slewing commands to the telescope. Consequently, this system provided two-axis control (single guide star) and used a simple method of updating the gyro stabilization. Figure 1 is a block diagram of the airborne portion of this system, and figure 2 is a diagram of the ground station controls.

Subsequent to the successful demonstration of this system on several balloon flights, the development of a more advanced version of the VIP system was started. The advanced system will include a charge coupled device (CCD) video sensor, three-axis control, and more sophisticated means of combining the pointing error signals with the gyro stabilization.

B. Design Considerations

The purpose of this work is to develop and evaluate a design method for the use of the video sensor and gyro data in updating the telescope's gyro stabilization. The task is broken into two parts: (1) the use of the video sensor multi-star position measurements to determine the three-axis pointing errors; and (2) the use of the pointing error signals combined with gyro data to update the gyro stabilization. The development of the multi-star processing and gyro filtering must take into account different control system analytical approaches and the performance goals and hardware limitations of the VIP system. Performance considerations for a telescope pointing system include steady pointing state accuracy, pointing jitter or noise, and dynamic response to disturbance torques and slewing commands.

The multi-star processing will directly affect the pointing accuracy and noise; the gyro filter will directly affect the pointing jitter, and will also affect the dynamic response and the basic gyro stabilization. The gyro filter will not, however, directly affect the steady-state pointing accuracy.

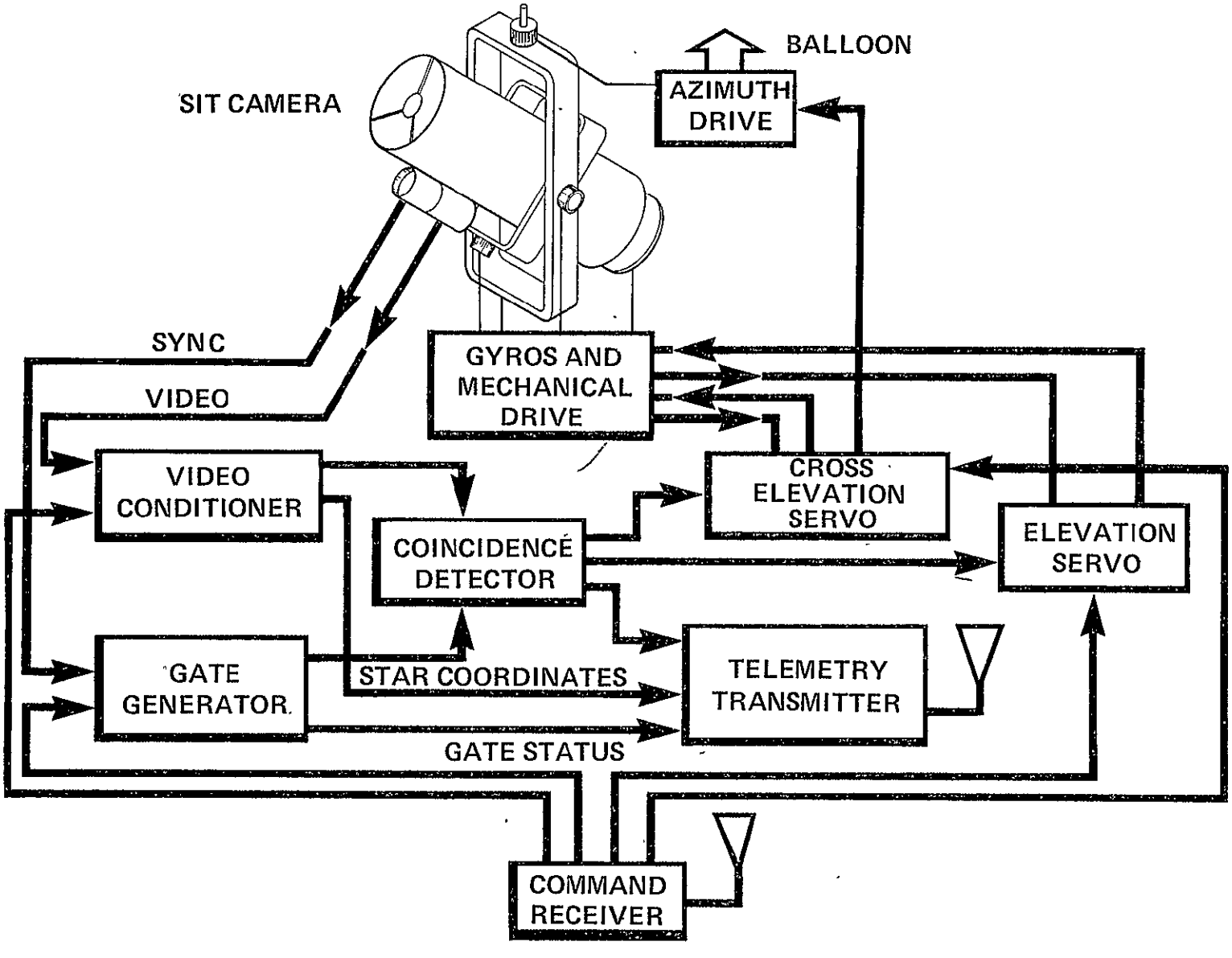

Figure 1.- First generation VIP system - airborne portion.

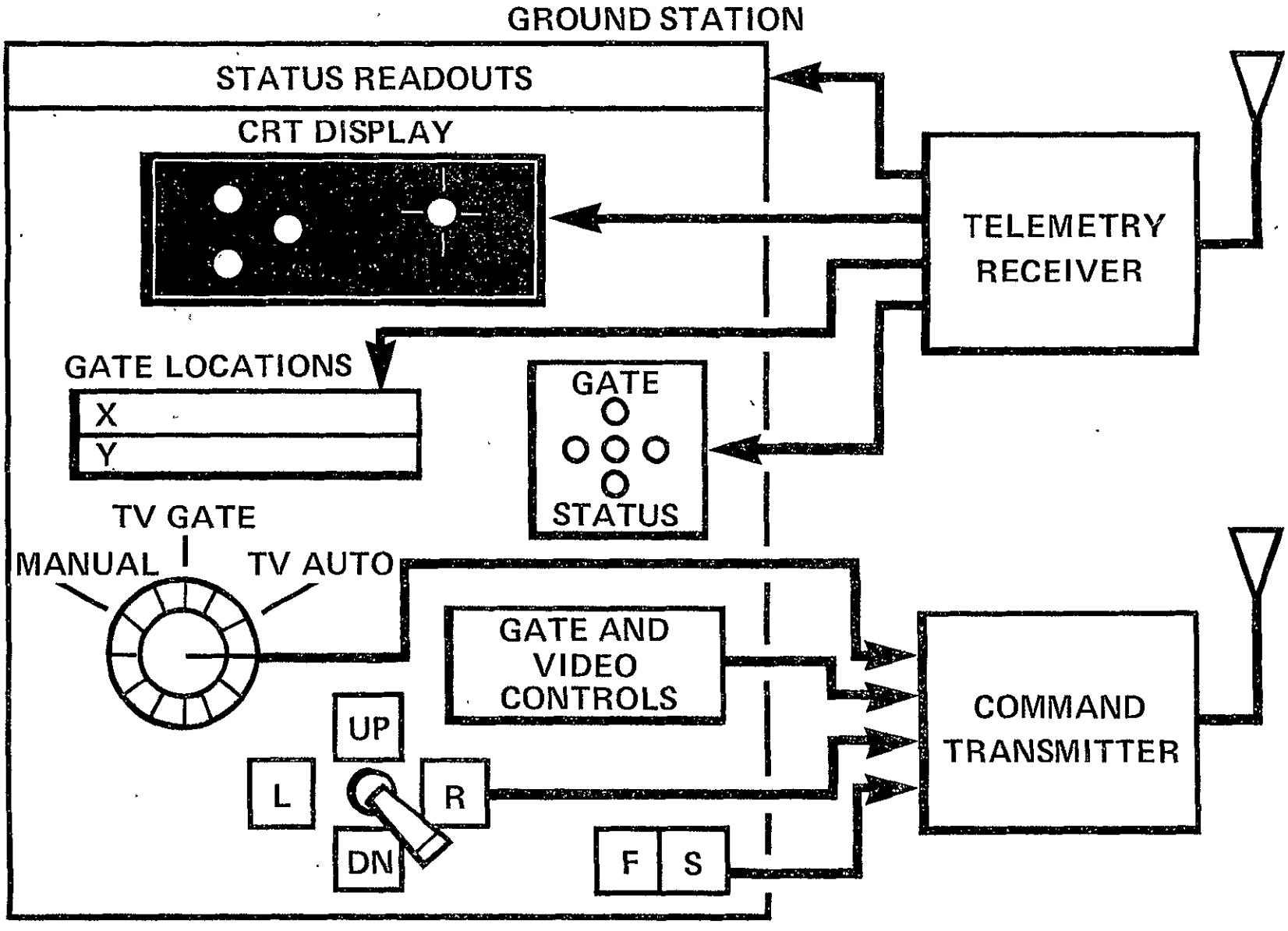

Figure 2.- First generation VIP system - ground station.

The primary hardware limitation imposed by the VIP system is the use of a small digital computer to perform the multi-star processing and gyro filtering. Multi-star processing equations must be developed that do not require excessive computation time as this will adversely affect the overall system dynamics. Selection of an approach to the gyro filter must consider the computation time associated with the multi-star processing. Because the VIP system is intended to interface with a telescope's basic gyro stabilization, an approach to the gyro filter design which does not require redesign of the gyro stabilization is desired.

Although VIP may eventually be used with a variety of telescope gyro stabilization systems, the first use will be with a system that uses analog rate integrating gyros (RIGs) [2]. Consequently, filter designs developed in this work assume that use of the RIG-type of gyro and design parameters for this existing telescope gyro stabilization are used for the filter evaluation.

Based on the limitations of the VIP microprocessor, the analytic approaches that can be used for the multi-star processing are somewhat limited. Consequently, small-angle, linearized equations are used and consideration is given to singularities and error performance. The resulting multi-star processing equations and selection criteria are believed to be unique. For the gyro filtering, a discrete filter, using the VIP microprocessor, is suggested due to the discrete nature of the video sensor star position measurements. Previous work [3] has considered the gyro filter design independently of the design of the basic gyro stabilization and that is the approach used here. Additional justification for this approach is developed using a continuous filter. The use of the RIG integration in a continuous filter has been

previously suggested [3] and this is extended to the discrete filter. Since the video sensor and multi-star processing introduces time delays into the attitude error measurements, these must be included in the filter model. Design charts and analyses for a discrete filter with a similar application have been developed [4] but no consideration has been given to the inclusion of time delays or filter dynamics. A digital computer program, DISC [5], based on the eigenvector decomposition solution of the steady-state, optional filter problem is used to analyze the different filter models. Both noise performance and dynamics are included in the filter analysis.

C. Outline

Chapter II describes the advanced VIP system hardware, operations, the CCD video sensor, and the operation of the CCD sensor.

The development of the multi-star processing equations used to obtain the three-axis pointing error signals from the video sensor's multiple star position data is contained in Chapter III. Several different methods are discussed and the resulting equations are examined for sensitivity and singularities. Based on the singularities, guide star and equation selection criteria are developed. The resulting equations are evaluated for accuracy performance using characteristics of the CCD video sensor. Performance improvement versus processing time is discussed and a summary of the multi-star processing approach concludes the chapter.

Chapter IV describes the development of the gyro filter. A continuous filter is used to gain insight into and to justify an approach to the filter design which does not affect the gyro stabilization. A steady-state discrete Kalman filter is developed for the VIP computer. Consideration of the system operation, video sensor, and multi-star

processing is used to determine what time delays must be included in the filter model. Six filters are developed that include different time delays and drift; they are analyzed for noise and pole locations for different combinations of sensor noise. Conclusions are drawn with respect to selection of sensor characteristics and resulting system performance. A digital simulation is developed which models the gyro stabilization and telescope dynamics and includes a model of the video sensor and discrete filters. The simulation is used to verify the approach taken to the filter design and provides data that can be used to select filter characteristics for the VIP system hardware.

Chapter V presents results and conclusions; a discussion of areas in which further work is needed is included.

CHAPTER II. DESCRIPTION OF THE ADVANCED VIP SYSTEM

A. System Description

The advanced VIP system [6] consists of three primary subsystems: (1) a CCD video sensor whose optical axis is coaligned with the telescope optical axis; (2) an electronics package, which includes a microprocessor and interface electronics; and (3) a control console with CRT display from which the system is operated. Figure 3 shows the VIP system and its primary subsystems.

The video sensor used by VIP is a key element of the system. Two important features of the VIP are dependent on the video sensor: the ability to provide three-axis control with a single sensor, and a CRT display of the telescope field of view for use by the operator. The CCD video sensor is an all solid-state device which uses interpolation techniques in order to obtain improved resolution. A microprocessor (in addition to the VIP microprocessor) in the CCD sensor electronics contains algorithms for the digital interpolation.

The VIP electronics package has two main sections: a national semiconductor IMP-16 microprocessor, and a group of circuits that interface the microprocessor to the video sensor, telescope stabilization system, and VIP control console. Figure 4 is a block diagram of the VIP electronics.

The microprocessor plays a central role in the VIP system. In addition to converting video sensor data into three-axis error signals via the multi-star processing algorithm, it performs all of the logic sequences necessary to initialize and track, it drives the CRT display, and it interrogates VIP control console switches to perform operator-controlled functions. The VIP microprocessor also communicates directly

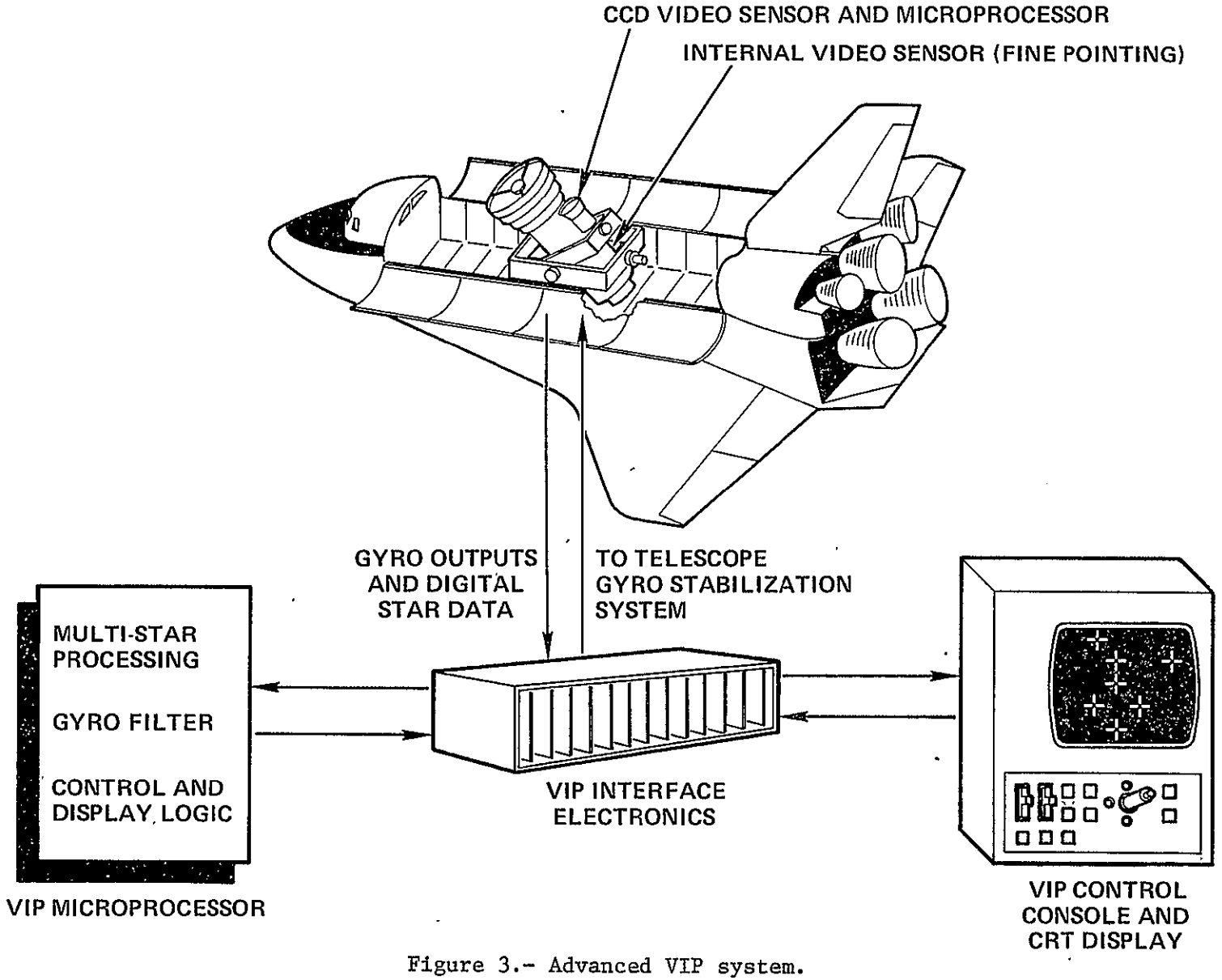

Figure 3.- Advanced VIP system.

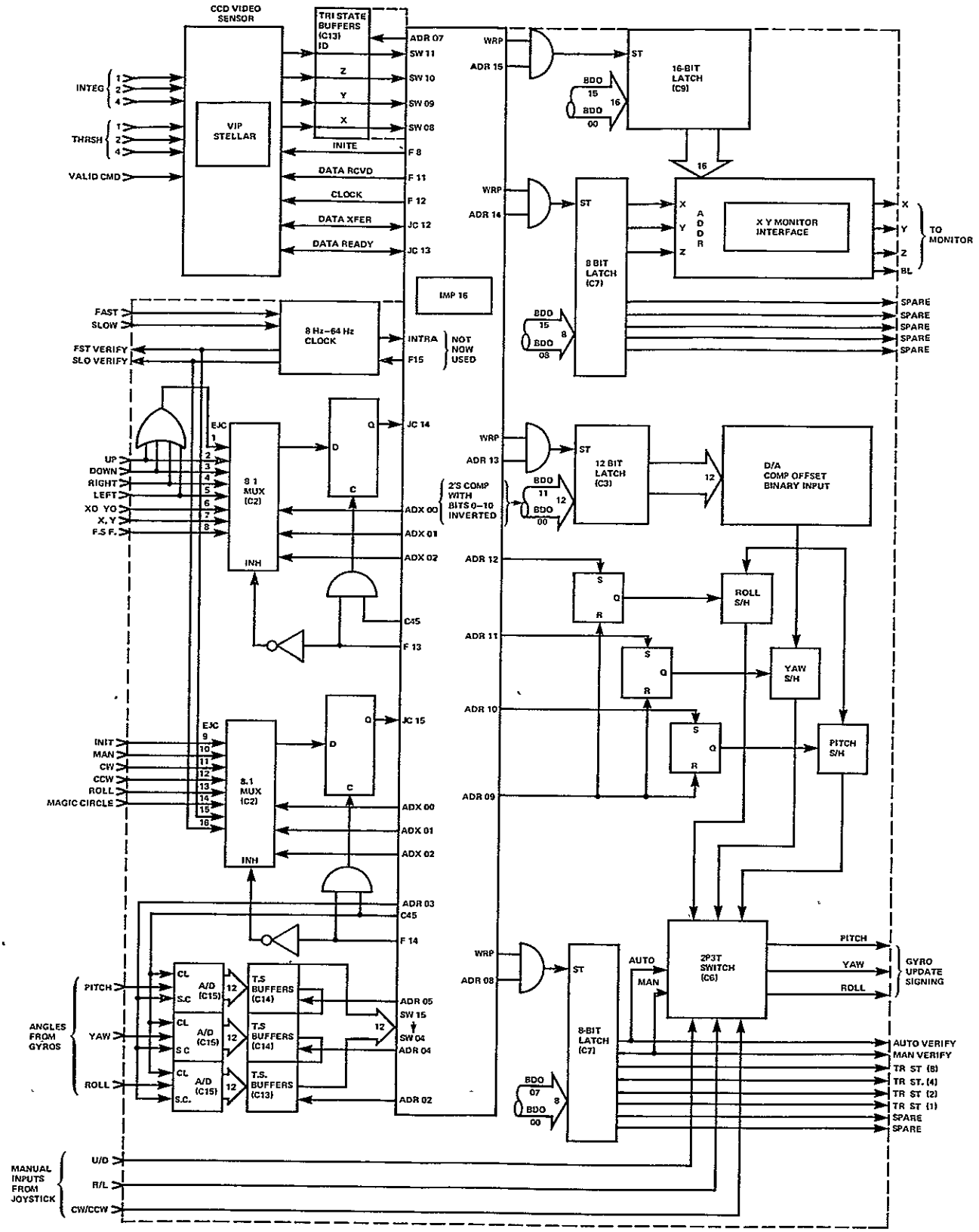

Figure 4.- Block diagram of the VIP microprocessor and interface electronics.

with the video sensor's microprocessor in order to effect data transfer as well as control the integration time and threshold level of the sensor.

The operator controls the position of the telescope line of sight with the joystick on the VIP control panel and may observe a variety of star-field presentations on the CRT display. Switches controlling VIP operation, auto/manual select, fast/slow slew rate, and star-field display options, surround the joystick controller. Threshold level and integration period for the star tracker are selected by means of two thumbwheel switches on the operator's left.

Operation of a VIP-controlled telescope begins with coarse acquisition of the target star field. This is accomplished by slewing the telescope to a pre-computed orientation and making an initial alignment with the joystick controller in the manual mode (joystick commands gyros directly). The star field, as viewed by the video sensor, is displayed on the CRT and the operator orients the telescope by comparing the CRT picture with a star chart. Alternatively, a computer-stored star map of the desired viewing area may be presented. When the target has been identified, the automatic mode is selected by pushing the "initialize" button located on the end of the joystick. This commands the VIP microprocessor to store the x-y locations of all of the stars being tracked by the video sensor. The pointing error in all three axes is calculated by comparing these current star positions from the video sensor with those stored in memory upon the "initialize" command. The calculated attitude error and the gyroscopically measured attitude error are then combined in the microprocessor gyro filter to provide the updates to each of the three gyros.

The operator may continue to reposition the telescope optical axis during automatic operation using the joystick to change the stored star positions. A display option may be selected in which only the star field in its desired location is presented. Joystick activation moves this pattern on the CRT screen to whatever new position is desired. The dynamics of telescope motion are not seen (since only commanded star field position is displayed) thereby enabling very precise positioning. Simultaneous selection of current telescope position for the display indicates to the operator how close the telescope is to pointing in the desired direction. The CRT will show two star fields in this mode, a bright one for actual position and a dimmer field for the desired position. When the two fields are coincident, the telescope is on target.

A digital indicator on the control console informs the operator of the number of stars currently being used for tracking. Another display option permits viewing only these stars. As new stars enter or depart the field of view, VIP can display them without disturbing the tracking function, and it can keep the operator continually informed of the number and location of tracked stars. If, because of slewing or tracker parameter changes, the number or position of tracked stars is unsatisfactory, the operator may reinitialize the system by pressing the "initialize" button again.

B. CCD Sensor Description.

The advanced VIP system is designed to use a sensor employing a charge coupled device (CCD) detector [7]. The face of the CCD detector is divided into a rectilinear pattern of discrete photosensitive elements, each connected to readout registers also located on the front

surface. As photons strike the detector, the charge build up in each element is transferred to the readout registers after a selectable period of integration, the charge being directly proportional to the number of photons striking an element during the integration period. Since the location of each element is uniquely specified, it is possible to obtain the precise coordinates, within the resolution of the photosensitive-element matrix, of any stars being imaged on the surface of the CCD.

The current state of the art for CCDs is a matrix of about 400 elements square. Commercially available CCDs are about 200 elements on a side. Thus, even the most advanced units cannot obtain resolution better than 0.5 arc min for 3° FOV optics. However, it is possible through a process of interpolation to improve the resolution by an order of magnitude.

The interpolation scheme requires that the output of a four by four matrix of elements be sampled and averaged each time the CCD is scanned. This array is centered on that element which first exceeds a pre-selected threshold during the initial scan of the device. Thus, for each star image, there is a corresponding four by four matrix for which the charge "center of mass" is computed. It is possible, therefore, to obtain computed star locations that are not centered on an element. The effect of this procedure is to increase the resolution by artificially increasing the element density.

The interpolation algorithm and the data formatting for use by the control system are complex, and their implementation requires extensive data handling. This is accomplished through the use of a microprocessor built into the electronics of the CCD video sensor. Raw data from the

CCD are read at the end of each integration period by the microprocessor; the microprocessor then computes the locations of the 10 brightest stars in the field of view. Each star is assigned an identification number and the four pieces of data for each star (x, y, brightness, and i.d.) are transferred to the VIP computer when the star tracker microprocessor completes the data for all of the stars in a frame. Logic within the microprocessor automatically takes care of stars entering or leaving the field of view so that while it is always possible to display all stars in the field of view, the VIP controller only accepts data for valid stars. A valid star is one that has met several criteria, both in the video sensor and within the VIP software. Attitude information is generated using only valid stars. Initializations of the star tracker may be accomplished at any time at the option of the operator with a pushbutton located on the VIP joystick.

The integration time and threshold are also controlled by the video sensor's microprocessor. Seven levels of both functions are selectable from thumbwheel switches on the VIP control panel. Figure 5 is a cutaway view of the star tracker that shows the major components. A modular approach has been taken to the optical and mechanical design so that the tracker may be easily modified to fit a variety of missions requirements. A Peltier-effect cooler is included for CCD operation on the ground; operation of the cooler during high altitude or orbital flight is not required.

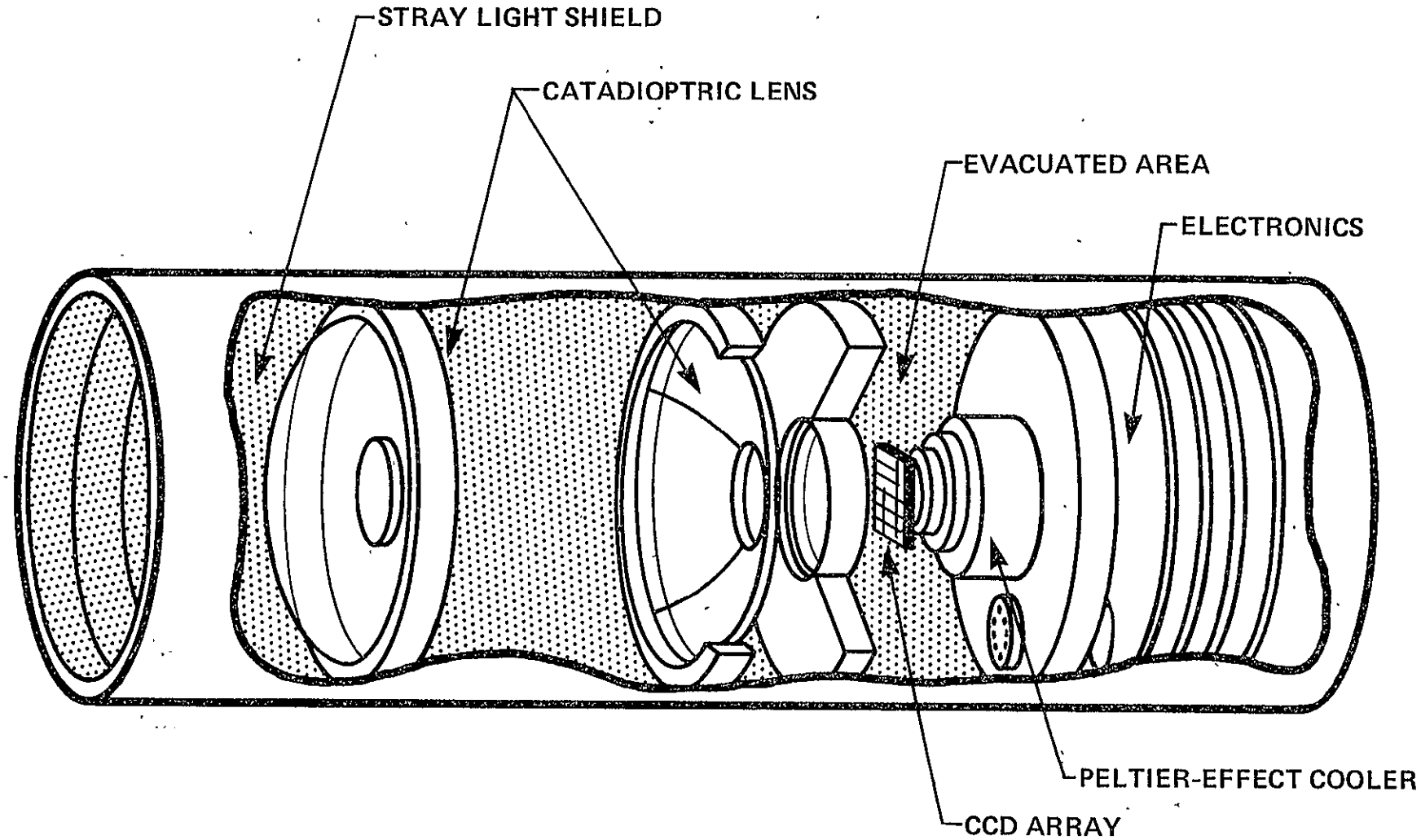

Figure 5.- CCD video sensor.

CHAPTER III. MULTI-STAR PROCESSING

A. Introduction

In order to determine the pointing error signals needed to point a telescope in three axes, measurements of the position of at least two known guide stars are required. A single guide star would provide pointing information for two axes perpendicular to the telescope's line of sight, and gyro information, subject to drift, would have to be relied on to orient the telescope about its line of sight. The video sensor used by the VIP system provides position measurements of several stars and these can be used to generate the complete three-axis pointing error. Since only two stars are required to determine the three-axis pointing errors, other stars can be used to generate additional estimates of the pointing error, and averaging or statistical techniques can be used to reduce the effects of errors in the video sensor.

There are several approaches that can be used to calculate the pointing error signals when the positions of two guide stars are measured by the video sensor (video sensor boresighted to telescope line of sight). One approach would use quaternions to relate the measured and desired pointing location; this method would be valid for large pointing errors, and for large angles between the guide stars and the video sensor. Alternatively, direction cosines could be used with the same result. Neither of these methods is desirable because the resulting equations involve trigonometric functions which are very time-consuming for a small digital computer such as the VIP microprocessor. Moreover, because the guide stars used by VIP are within a small angular distance of the telescope and the desired pointing location (video sensor has relatively narrow field of view), the large angle advantage provided by

these methods is not required. Consequently, small-angle approximations to coordinate transformations are used to develop the basic equations that provide the three-axis pointing error signals from position measurements of a guide star pair.

B. Basic Equations

If the position of a guide star is known with respect to the desired telescope pointing position and if the actual telescope pointing position is in error by a small amount,

$$\begin{bmatrix} x \\ y \\ z \end{bmatrix}_T = \begin{bmatrix} 1 & \theta r & -\theta y \\ -\theta r & 1 & \theta p \\ \theta y & -\theta p & 1 \end{bmatrix} \begin{bmatrix} x \\ y \\ z \end{bmatrix}_I \tag{1}$$

where $[\ ]_I$ is defined to be the star direction in a vector basis aligned to the desired telescope pointing position and $[\ ]_T$ is the actual telescope pointing position in the same vector basis. z_T is aligned to the telescope line of sight and x_T and y_T are the transverse directions (yaw and pitch, respectively). Since the video sensor measures only x_T and y_T, then

$$x_T = x_I + \theta r y_I - \theta y z_I\,, \qquad y_T = -\theta r x_I + y_I + \theta p z_I \tag{2}$$

If x_I and y_I are the desired location of the star, then the measured quantities (x_T, y_T) and the desired quantities (x_I, y_I) can be subtracted

$$\Delta x \triangleq x_T - x_I\,, \qquad \Delta y \triangleq y_T - y_I \tag{3}$$

to relate known quantities to the pointing errors (θr, θp, θy). Since the star direction can be considered a unit vector, $z_I = 1$ and

$$\Delta x = \theta r y_I - \theta y\,, \qquad \Delta y = -\theta r x_I + \theta p \tag{4}$$

Examination of these equations makes it apparent that one guide star provides two measurements related to the three unknowns, θr, θp, and θy, and as expected at least two guide stars must be used to uniquely determine the three-axis pointing errors.

C. Processing Options

The measurements of guide star position provided by the video sensor will be corrupted by errors caused by noise and nonlinearities in the sensor and by the errors resulting from the interpolation computations performed in the video sensor's microprocessor. If the combination of errors is assumed to result in a Guassian distribution of star position measurement errors, then there are several options available for using equations (4) for determining the pointing errors from several star position measurements. These options are discussed below.

Option 1. Process all star measurement data simultaneously using a least mean squares approach (LMS) assuming prior knowledge of the error statistics associated with the star position measurements. For example, for three stars,

$$\begin{bmatrix} \Delta x_1 \\ \Delta y_1 \\ \Delta x_2 \\ \Delta y_2 \\ \Delta x_3 \\ \Delta y_3 \end{bmatrix} = A \begin{bmatrix} \theta r \\ \theta p \\ \theta y \end{bmatrix} + \begin{bmatrix} v_1 \\ v_2 \\ v_3 \\ v_4 \\ v_5 \\ v_6 \end{bmatrix} \tag{5}$$

and

$$\begin{bmatrix} \hat{\theta} r \\ \hat{\theta} p \\ \hat{\theta} y \end{bmatrix} = P A^T R^{-1} \begin{bmatrix} \Delta x_1 \\ \Delta y_1 \\ \Delta x_2 \\ \Delta y_2 \\ \Delta x_3 \\ \Delta y_3 \end{bmatrix} \tag{6}$$

where

$$P^{-1} = A^T R^{-1} A , \quad R = E[VV^T] , \quad P = E[(\hat{\theta} - \theta)(\hat{\theta} - \theta)^T] \tag{7}$$

and

$$A = \begin{bmatrix} y_{10} & 0 & -1 \\ -x_{10} & 1 & 0 \\ y_{20} & 0 & -1 \\ -x_{20} & 1 & 0 \\ y_{30} & 0 & -1 \\ -x_{30} & 1 & 0 \end{bmatrix} \tag{8}$$

Option 2. Process star pair measurements using an LMS approach and then average the resulting pointing error estimates to obtain a final pointing error estimate. In a similar fashion to equations (5), (6), and (7), for two stars:

$$\begin{bmatrix} \Delta x_1 \\ \Delta y_1 \\ \Delta x_2 \\ \Delta y_2 \end{bmatrix} = A \begin{bmatrix} \theta r \\ \theta p \\ \theta y \end{bmatrix} + \begin{bmatrix} v_1 \\ v_2 \\ v_3 \\ v_4 \end{bmatrix} \tag{9}$$

and

$$\hat{\theta} = PA^T R^{-1} \begin{bmatrix} \Delta x_1 \\ \Delta y_1 \\ \Delta x_2 \\ \Delta y_2 \end{bmatrix} \tag{10}$$

Assuming independent errors for the x and y values of the star position measurements, the resulting equations for $\hat{\theta}r$, $\hat{\theta}p$, and $\hat{\theta}y$ for each star pair are

$$\hat{\theta}r = \frac{\left(\frac{1}{R_2}+\frac{1}{R_4}\right)\left(\frac{1}{R_1}+\frac{1}{R_3}\right)}{\Delta}\left(\frac{y_{10}}{R_1}\Delta x_1 - \frac{x_{10}}{R_2}\Delta y_1 + \frac{y_{20}}{R_3}\Delta x_2 - \frac{x_{20}}{R_4}\Delta y_2\right)$$

$$+ \frac{\left(\frac{x_{10}}{R_2}+\frac{x_{20}}{R_4}\right)\left(\frac{1}{R_1}+\frac{1}{R_3}\right)}{\Delta}\left(\frac{\Delta y_1}{R_1}+\frac{\Delta y_2}{R_4}\right) \tag{11}$$

$$\hat{\theta}p = \left(\frac{x_{10}}{R_2}+\frac{x_{20}}{R_4}\right)\left(\frac{1}{R_1}+\frac{1}{R_3}\right)\left(\frac{y_{10}}{R_1}\,\Delta x_1 - \frac{x_{10}}{R_2}\,\Delta y_1 + \frac{y_{20}}{R_3}\,\Delta x_2 - \frac{x_{20}}{R_4}\,\Delta y_2\right)$$

$$+ \frac{1}{\Delta}\left[\left(\frac{y_{10}^2}{R_1}+\frac{x_{10}^2}{R_2}+\frac{y_{20}^2}{R_3}+\frac{x_{20}^2}{R_4}\right)\left(\frac{1}{R_1}+\frac{1}{R_3}\right) - \left(\frac{y_{10}}{R_1}+\frac{y_{20}}{R_3}\right)^2\right]\left(\frac{\Delta y_1}{R_2}+\frac{\Delta y_2}{R_4}\right)$$

$$+ \frac{\left(\frac{x_{10}}{R_2}+\frac{x_{20}}{R_4}\right)\left(\frac{y_{10}}{R_1}+\frac{y_{20}}{R_3}\right)}{\Delta}\left(-\frac{\Delta x_1}{R_1} - \frac{\Delta x_2}{R_3}\right) \qquad (12)$$

$$\hat{\theta}y = \frac{\left(\frac{y_{10}}{R_1}+\frac{y_{20}}{R_3}\right)\left(\frac{1}{R_2}+\frac{1}{R_4}\right)}{\Delta}\left(\frac{y_{10}}{R_1}\,\Delta x_1 - \frac{x_{10}}{R_2}\,\Delta y_1 + \frac{y_{20}}{R_3}\,\Delta x_2 - \frac{x_{20}}{R_4}\,\Delta y_2\right)$$

$$+ \frac{\left(\frac{x_{10}}{R_2}+\frac{x_{20}}{R_4}\right)\left(\frac{y_{10}}{R_1}+\frac{y_{20}}{R_3}\right)}{\Delta}\left(\frac{\Delta y_1}{R_2} + \frac{\Delta y_2}{R_4}\right)$$

$$+ \frac{1}{\Delta}\left[\left(\frac{y_{10}^2}{R_1}+\frac{x_{10}^2}{R_2}+\frac{y_{20}^2}{R_3}+\frac{x_{20}^2}{R_4}\right)\left(\frac{1}{R_2}+\frac{1}{R_4}\right) - \left(\frac{x_{10}}{R_2}+\frac{x_{20}}{R_4}\right)^2\right]\left(-\frac{\Delta x_1}{R_1} - \frac{\Delta x_2}{R_4}\right) \qquad (13)$$

where

$$\Delta = \left(\frac{y_{10}^2}{R_1}+\frac{x_{10}^2}{R_2}+\frac{y_{20}^2}{R_3}+\frac{x_{20}^2}{R_4}\right)\left(\frac{1}{R_2}+\frac{1}{R_4}\right)\left(\frac{1}{R_1}+\frac{1}{R_2}\right)$$

$$- \left(\frac{x_{10}}{R_2}+\frac{x_{20}}{R_4}\right)^2\left(\frac{1}{R_1}+\frac{1}{R_3}\right) - \left(\frac{y_{10}}{R_1}+\frac{y_{20}}{R_3}\right)^2\left(\frac{1}{R_3}+\frac{1}{R_4}\right) \qquad (14)$$

Option 3. Process star pair data algebraically using equations (4) and then average the pointing error estimates obtained for each star pair to obtain the final pointing error. Since for two stars there are four equations in three unknowns, there are several independent ways to solve for θr, θp, and θy. The resulting equations are:

$$\theta r = \frac{\Delta x_1 - \Delta x_2}{y_{10} - y_{20}} \tag{15a}$$

or $$\frac{\Delta y_1 - \Delta y_2}{x_{20} - x_{10}} \tag{15b}$$

$$\theta p = \frac{x_{10}\Delta y_2 - x_{20}\Delta y_1}{x_{10} - x_{20}} \tag{16a}$$

or $$- \frac{y_{10}\Delta y_1 + x_{10}\Delta x_2 + y_{20}\Delta y_1 - x_{10}\Delta x_1}{y_{20} - y_{10}} \tag{16b}$$

or $$\frac{x_{20}\Delta x_1 - y_{20}\Delta y_2 - x_{20}\Delta x_2 + y_{10}\Delta y_2}{y_{10} - y_{20}} \tag{16c}$$

$$\theta y = \frac{y_{10}\Delta x_2 - y_{20}\Delta x_1}{y_{20} - y_{10}} \tag{17a}$$

or $$\frac{y_{10}\Delta y_2 - x_{10}\Delta x_1 + x_{20}\Delta x_1 - y_{10}\Delta y_1}{x_{10} - x_{20}} \tag{17b}$$

or $$- \frac{x_{20}\Delta x_2 + y_{20}\Delta y_1 + x_{10}\Delta x_2 - y_{20}\Delta y_2}{x_{20} - x_{10}} \tag{17c}$$

D. Comparison of Options

The important items to be considered in comparing the three options are the number of arithmetic operations required and the pointing error performance. Option 1 can be eliminated at the ouset due to the large number of operations for the matrix multiplications and inversions when more than two guide stars are available. A comparison of the number of operations required for Options 2 and 3 can be made by considering the θp equation (12) and the θp equation (16b) or (16c). Table 1 summarizes the number of algebraic operations for each equation, and it is easy to see that Option 3 offers considerable savings in computation

TABLE 1. COMPARISON OF OPERATIONS REQUIRED FOR STAR PAIR SOLUTION

Operation	$\hat{\theta}_p$ Option 2 LMS	θ_p Option 3 Algebraic
Multiplication	24	4
Division	43	1
Addition Subtraction	25	4

time. The number of operations for θ_p assumes that the R_i's for each star are known ahead of time but combinations such as $[(1/R_1) + (1/R_3)]$ must be computed in real time after star pairs are selected.

In addition to the number of arithmetic operations, pointing error performance of the two options must be considered. A simple comparison can be made by considering two stars on the x axis of the video sensor equally spaced about the origin ($x_{10} = -x_{20}$). With this positioning of the stars, equation (16a) can be used for θ_p and the variances of the error in θ_p and $\hat{\theta}_p$ are

$$E[\varepsilon^2_{\theta_p}] = \frac{R_4 + R_2}{4}, \quad E[\varepsilon^2_{\hat{\theta}_p}] = \frac{R_2 R_4}{R_2 + R_4} \tag{18}$$

From these, the ratio

$$\frac{E[\varepsilon^2_{\theta_p}]}{E[\varepsilon^2_{\hat{\theta}_p}]} = \frac{(R_4 + R_2)^2}{4R_2R_4} \tag{19}$$

can be used to compare the relative performance of the two options. If $R_4 = R_2$, then $(E[\varepsilon^2_{\theta_p}]/E[\varepsilon^2_{\hat{\theta}_p}]) = 1$ indicating no performance advantage for Option 2 when the star position measurement errors have equal

variances. When $R_4 = 2R_2$, then $(E[\varepsilon^2_{\theta p}]/E[\varepsilon^2_{\hat{\theta} p}]) = 1.125$ and there is still no large improvement, considering the large amount of extra computation time required.

Based on this comparison, Option 3 appears to be the best approach. Examination of the equations for Option 3 reveals that there are singularities associated with each equation depending on the relative locations of stars associated with each guide star pair. Consequently, consideration must be given to these singularities in the selection of which equation to use and in the selection of guide star pairs.

E. Selection of Equations and Guide Stars

Determination of which equations to use for θr, θp, θy and how to select guide star pairs can be made by considering the variances of the equations (15)-(17). If the errors associated with each Δx_i and Δy_i measurement are assumed to be identically distributed and independent with

$$E[\Delta x_i^2] = E[\Delta y_i^2] = \sigma^2$$

then, as an example

$$E[\varepsilon^2_{\theta r}] = \frac{2\sigma^2}{(y_{10} - y_{20})^2}$$

for equation (15a). Table 2 summarizes the θr, θp, and θy pointing error equations and their variances.

The variances of the θr pointing error equations, (15a) and (15b), depend on $1/(y_{10} - y_{20})^2$ and $1/(x_{20} - x_{10})^2$, respectively. A nondimensionalized plot of $1/(x_{10} - y_{20})^2$ is shown in figure 6. Although not shown, the first and third quadrants, and second and fourth quadrants are identical and there is clearly a discontinuity at the origin. A similar figure would hold for $1/(y_{10} - y_{20})^2$. The key feature of the diagram is the singularity when $x_{10} = x_{20}$ or $y_{10} = y_{20}$ and the larger

TABLE 2. SUMMARY OF POINTING ERROR EQUATIONS

$E[\Delta xi^2] = E[\Delta yi^2] = \sigma^2$

	Attitude error equation	E [Attitude error^2][a]	Singularities	
θr	$\frac{\Delta x_1 - \Delta x_2}{y_{10} - y_{20}}$ 15a	$\frac{2\sigma^2}{(y_{10} - y_{20})^2}$	$y_{10} = y_{20}$	Best performance y_{10} and y_{20} are opposite sign
	$\frac{\Delta y_1 - \Delta y_2}{x_{20} - x_{10}}$ 15b	$\frac{2\sigma^2}{(x_{20} - x_{10})^2}$	$x_{10} = x_{20}$	Best performance x_{10} and x_{20} are opposite sign
θp	$\frac{x_{10}\Delta y_2 - x_{20}\Delta y_1}{k(x_{10} - x_{20})}$ 16a	$\frac{\sigma^2(x_{10}^2 + x_{20}^2)}{k^2(x_{10} - x_{20})^2}$	$x_{10} = x_{20}$	Amplification of error when x_{10} and x_{20} same sign
	$\frac{-y_{10}\Delta y_1 + x_{10}\Delta x_2 + y_{20}\Delta y_1 - x_{10}\Delta x_1}{k(y_{20} - y_{10})}$ 16b	$\frac{\sigma^2[(y_{20}^2 + y_{10}^2) + 2x_{10}^2]}{k^2(y_{20} - y_{10})^2}$	$y_{10} = y_{20}$	Amplification of error when y_{10} and y_{20} same sign
	$\frac{x_{20}\Delta x_1 - y_{20}\Delta y_2 - x_{20}\Delta x_2 + y_{10}\Delta y_2}{k(y_{10} - y_{20})}$ 16c	$\frac{\sigma^2[(y_{20}^2 + y_{10}^2) + 2x_{20}^2]}{k^2(y_{20} - y_{10})^2}$	$y_{10} = y_{20}$	Amplification of error when y_{10} and y_{20} same sign
θy	$\frac{y_{10}\Delta x_2 - y_{20}\Delta x_1}{k(y_{20} - y_{10})}$ 16a	$\frac{\sigma^2(y_{10}^2 + y_{20}^2)}{k^2(y_{20} - y_{10})^2}$	$y_{10} = y_{20}$	Amplification of error when y_{10} and y_{20} same sign
	$\frac{y_{10}\Delta y_2 - x_{10}\Delta x_1 + x_{20}\Delta x_1 - y_{10}\Delta y_1}{k(x_{10} - x_{20})}$ 16b	$\frac{\sigma^2[(x_{10}^2 + x_{20}^2) + 2y_{10}^2]}{k^2(x_{10} - x_{20})^2}$	$x_{10} = x_{20}$	Amplification of error when x_{10} and x_{20} same sign
	$\frac{-x_{20}\Delta x_2 + y_{20}\Delta y_1 + x_{10}\Delta x_2 - y_{20}\Delta y_2}{k(x_{20} - x_{10})}$ 16c	$\frac{\sigma^2[(x_{10}^2 + x_{20}^2) + 2y_{20}^2]}{k^2(x_{10} - x_{20})^2}$	$x_{10} = x_{20}$	Amplification of error when x_{10} and x_{20} same sign

[a]Assumes Δx_i and Δy_i are identically distributed independent random variables.

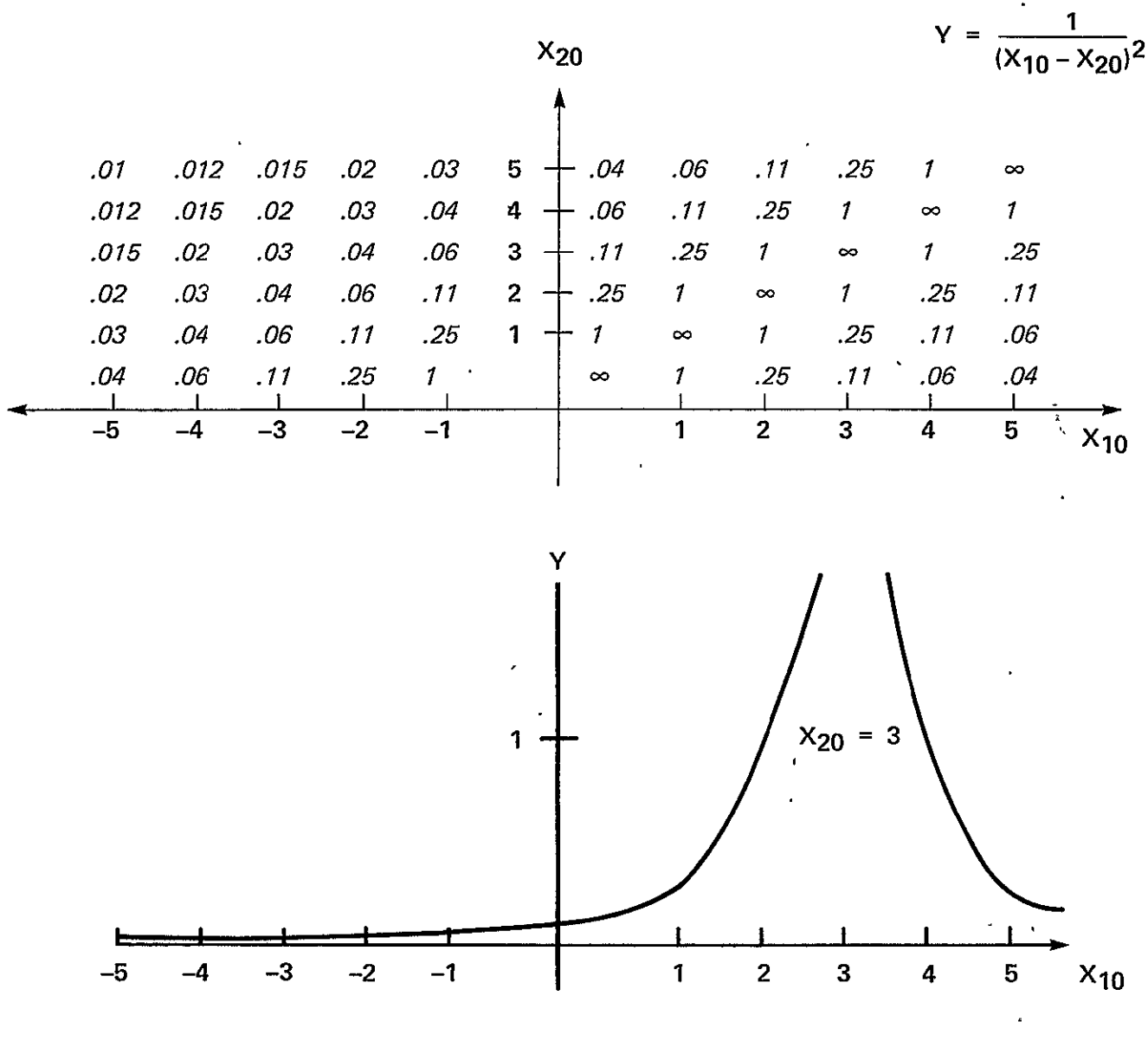

Figure 6.- Plot of $1/(x_{10} - x_{20})^2$.

values when x_{10} and x_{20}, or y_{10} and y_{20} are the same sign. Consequently, when the x coordinates of the guide star pair are the same sign, equation (15a) should be used, and when the y coordinates are the same sign, equation (15b) should be used for θr. This selection is summarized in table 3. The case where two stars are in the same quadrant is eliminated by this selection strategy and results in a slight reduction in the probability of obtaining useful guide stars in a given field of view. This is not a serious problem and can be taken into account when designing the optics of the video sensor by considering lens size and field of view versus sensitivity and star densities.

In a similar fashion, selection of the appropriate equation for θp or θy can be determined. Since the basic form of the equations is the same for θp and θy, the selection rules for θp can be used for θy by observing the proper symmetry. Considering θp, the variance of equation (16a) depends on

$$\frac{x_{10}^2 + x_{20}^2}{(x_{10} - x_{20})^2}$$

and a nondimensionalized plot of this equation is shown in figure 7. Again, the first and third, and second and fourth quadrants are identical and there is a discontinuity at the origin. The key features are the singularity when $x_{10} = x_{20}$ and the larger errors resulting when x_{10} and x_{20} are the same sign. The variances of equations (16b) and (16c) for θp can be rewritten as

$$\text{(16b)} \qquad \frac{\sigma^2(y_{20}^2 + y_{10}^2)}{(y_{20} - y_{10})^2} + \frac{2\sigma^2 x_{10}^2}{(y_{20} - y_{10})^2} \qquad (20)$$

TABLE 3. STAR PAIR AND EQUATION SELECTION CRITERIA

Case	θr	θp	θy
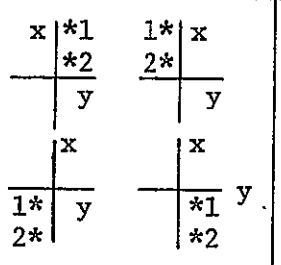	Not selected as valid star pair due to singularities and amplification of errors		
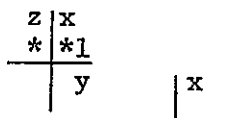	15a	16b If $\lvert x_{20}\rvert > \lvert x_{10}\rvert$ 16c If $\lvert x_{10}\rvert > \lvert x_{20}\rvert$	17a
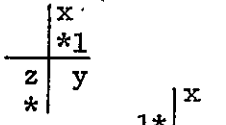	15a If $\lvert y_{10} - y_{20}\rvert > \lvert x_{10} - x_{20}\rvert$ 15b If $\lvert x_{10} - x_{20}\rvert > \lvert y_{10} - y_{20}\rvert$	16a	17a
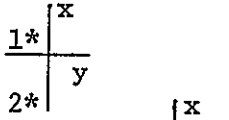	15b	16a	17b If $\lvert y_{20}\rvert > \lvert y_{10}\rvert$ 17c If $\lvert y_{10}\rvert > \lvert y_{20}\rvert$

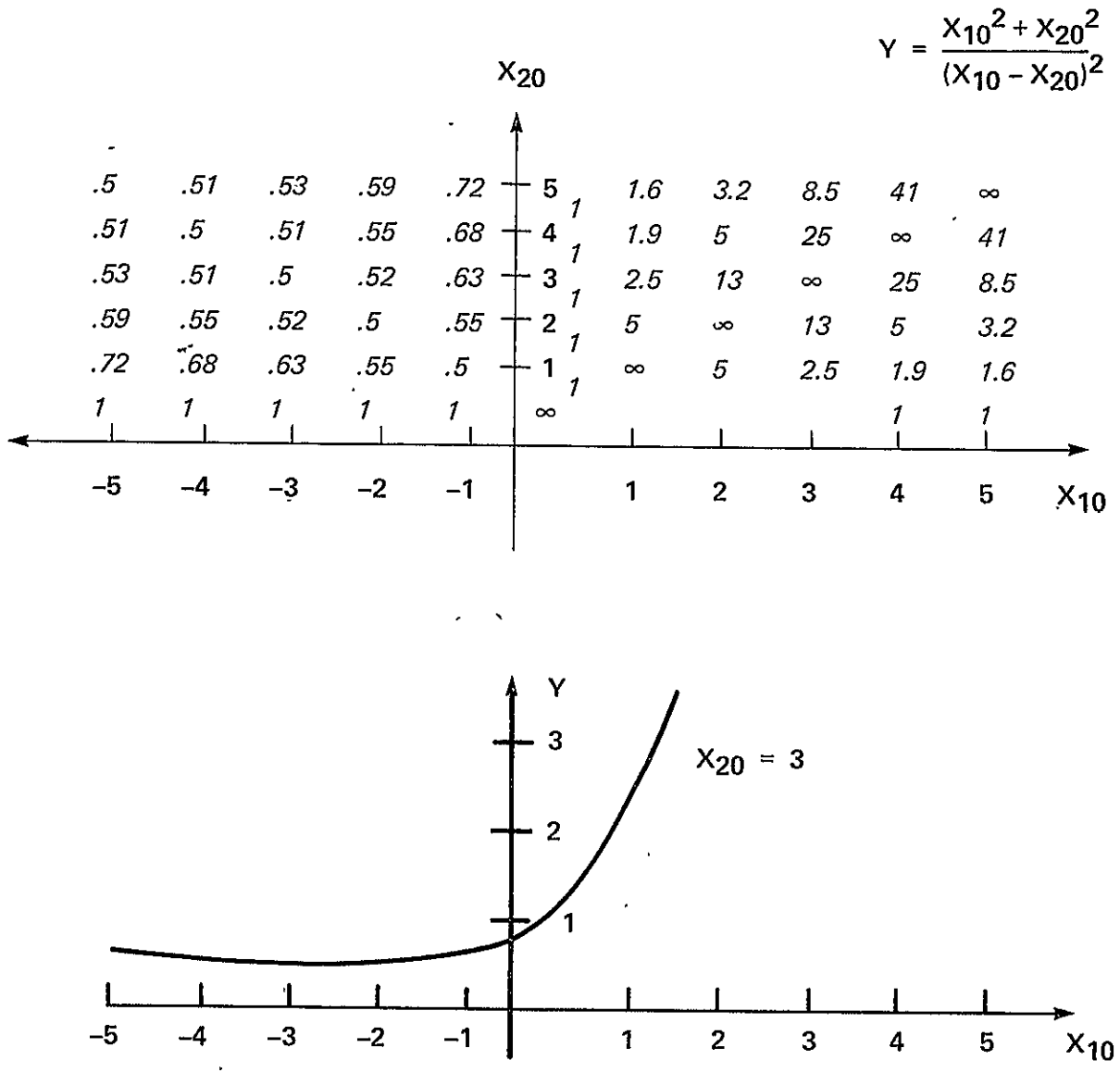

Figure 7.- Plot of $(x_{10}^2 + x_{20}^2)/(x_{10} - x_{20})^2$.

(16c) $$\frac{\sigma^2(y_{20}^2 + y_{10}^2)}{(y_{20} - y_{10})^2} + \frac{2\sigma^2 x_{20}^2}{(y_{20} - y_{10})^2} \qquad (21)$$

so that these equations have the same singularities when $y_{20} = y_{10}$ and the same amplification of error when y_{10} and y_{20} are the same sign. Consequently, when the x coordinates of the guide star pair are the same sign, equation (16b) should be used if $|x_{10} \leq |x_{20}|$. Alternatively, equation (16c) should be used if $|x_{20}| < |x_{10}|$. If the y coordinates of the guide stars are the same sign, then (16a) should be used. The case where both guide stars are in the same quadrant is eliminated in a way similar to that of θr. Table 3 also summarizes the θr, θp, and θy guide star and the equation selection process.

F. Roll Sensitivity

Although the selection process described in the previous section can be used, an additional criterion should be considered for the selection of guide star pairs for θr. Comparing the variance of equation (15b) (θr) with (16a) (θp) we find that

$$\frac{E[\varepsilon_{\theta r}^2]}{E[\varepsilon_{\theta p}^2]} = \frac{2}{(x_{10} - x_{20})^2} \qquad (22)$$

and if the x_{10} and x_{20} values are measured in degrees then

$$\frac{E[\varepsilon_{\theta r}^2]}{E[\varepsilon_{\theta p}^2]} = \frac{2(57.3)^2}{(x_{10} - x_{20})^2} \qquad (23)$$

Consequently, the roll pointing errors are much larger than the pitch and yaw errors unless the guide stars are far from the origin. This result is not unique to the equations used, but is a result of the geometry of using stars close to the desired pointing direction to determine the pointing error for the axis (θr) aligned to the line of sight. This suggests an additional criterion for selection of roll guide star pairs;

select roll guide star pairs where one of the stars is outside of a radius with a pre-selected diameter. For this criterion, figure 8 can be used to determine an upper bound on the θr errors as a function of this radius.

G. Performance and System Tradeoffs

Ultimate pointing performance of the system is a direct function of the video sensor errors, both steady state and noise, the multi-star processing, the gyro noise and gyro filtering. Video sensor noise sources include random events in the photoelectric processes, electronics noise, and quantization levels in the sensor's microprocessor. The number of bits used in the sensor's microprocessor and in the electronics can be designed so that the primary noise source is the photoelectric process. Video sensor steady-state errors result from nonlinearities in the sensor and from the accuracy with which the sensor performs the interpolation calculations.

The multi-star processing will improve both the noise and steady-state errors associated with the video sensor star position measurements. The reduction in errors results from the averaging and thus depends on the number of guide star pairs used. As an example of this, we can consider the CCD sensor. The largest error for the CCD sensor is the accuracy of the interpolation algorithms, and well spacing and non-uniformities limit the CCD interpolation accuracy to 10% of the CCD array well size [7]. If the interpolation error is assumed to be uniformly distributed then

$$E[\Delta x_i^2 \quad \text{or} \quad \Delta y_i^2] = \frac{a^2}{3} \triangleq \sigma^2 \tag{24}$$

where a is 0.1 times the well dimension in arc sec. Referring to table 2, and assuming guide star pairs that allow use of the "a"

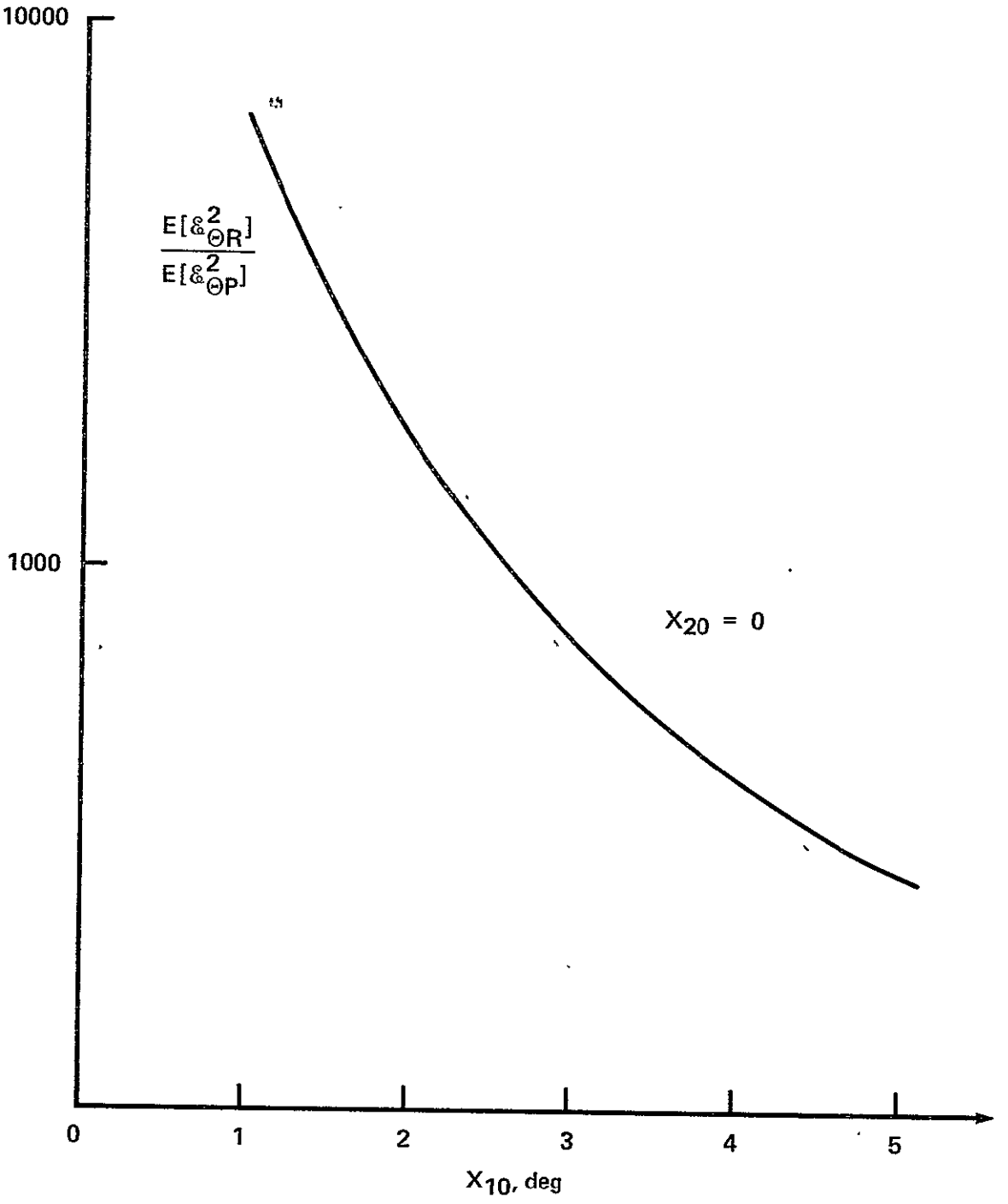

Figure 8.- Roll pointing error comparison.

equations for pitch and yaw

$$E[\theta p^2 \quad \text{or} \quad \theta y^2] \leq \sigma^2 \triangleq \sigma p^2 \quad \text{or} \quad \sigma y^2 \tag{25}$$

since

$$\frac{x_{10}^2 + x_{20}^2}{(x_{10} - x_{20})^2} \leq 1\,, \qquad \frac{y_{10}^2 + y_{20}^2}{(y_{10} - y_{20})^2} \leq 1 \tag{26}$$

from figure 7. If four guide star pairs are assumed then

$$E[\varepsilon_{\theta p_{AVE}}^2 \quad \text{or} \quad \varepsilon_{\theta y_{AVE}}^2] \leq \frac{\sigma^2}{N}\,, \qquad N = 4 \tag{27}$$

Similarly, if guide star pairs with one star of each pair are assumed to be at least 2° from the origin

$$E[\varepsilon_{\theta r}^2] \leq \frac{2(57.3)^2\sigma^2}{4} \tag{28}$$

from figure 6. If four guide star pairs are assumed then

$$E[\varepsilon_{\theta r_{AVE}}^2] \leq \frac{2\sigma^2(57.3)^2}{4N}\,, \qquad N = 4 \tag{29}$$

Table 4 summarizes the 1-σ roll, pitch, and yaw pointing errors resulting from the interpolation error for a CCD array size of 400 × 400 elements. The relatively poor roll performance is a result of geometry, as explained earlier.

TABLE 4. 1-σ POINTING ERRORS (ARC SEC) USING FOUR GUIDE STAR PAIRS

Array size (field of view)	a	σ_R	$\sigma_{R_{AVE}}$	$\sigma_{p,y}$	$\sigma_{p,y_{AVE}}$
400 × 400 (2° × 2°)	1.8	≤44	≤22	≤1.0	≤0.5

The effect of the multi-star processing averaging is shown in table 4 and provides a $1/\sqrt{N}$ (N number of guide star pairs) improvement in the 1-σ values of the pointing error signals. However, the time required to process the additional guide star pairs and to perform the averaging, increase proportional to N. Figure 9 shows these two effects, and it is clear that the computation time increases significantly faster than the errors improve. As discussed earlier, there are two components of the overall system pointing error: steady-state and noise or jitter. The video sensor's star position measurements contain both steady-state and noise errors and the averaging in the multi-star processing reduces both types of error equally. However; while the gyro filter does not affect steady-state pointing error of the system, one of its primary purposes is to combine the pointing error signals from the multi-star processing with the gyro signal to obtain a low noise estimate of the pointing error signals. As discussed in the gyro filtering section, the time required to perform the multi-star processing increases the delay between actual star position measurement and the time at which the resulting pointing error signals are used to update the gyro filter. It is shown that larger time delays increase the noise of the gyro filter's pointing error estimate. Consequently, in a final system design, a careful tradeoff must be made between the reduction in steady-state errors provided by using additional guide star pairs in the multi-star processing and the effect on noise performance of the gyro filter caused by the increased time delay.

H. Summary of Multi-Star Processing Technique

The technique developed for the multi-star processing using the linearized small angle equations can be summarized as follows:

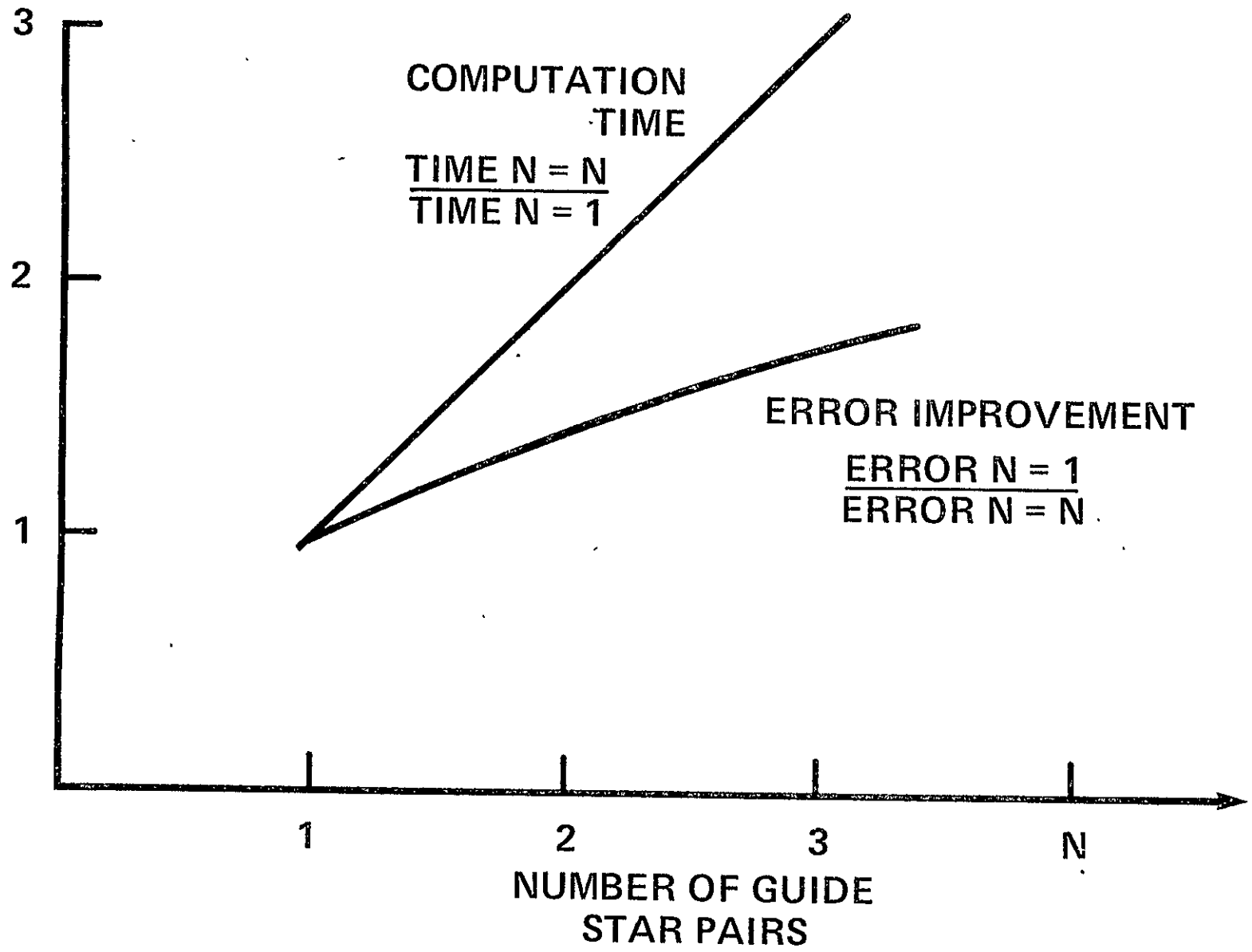

Figure 9.- Comparison of computation time and error improvement versus number of guide star pairs.

1. Select valid guide star pairs from those stars provided by the video sensor eliminating as pairs those stars that are in the same quadrant. Additional criteria for roll is the elimination of potential guide star pairs unless one of the stars is farther from the origin than a pre-selected angle.

2. For each guide star pair for pitch and yaw, select the appropriate equation (table 3) and solve for θp and θy. For the roll guide star pairs, again select the appropriate equation and solve for θr for each guide star pair.

3. Average the θr, θp, and θy pointing errors obtained for each guide star pair to obtain a final estimate of the three axis pointing errors.

CHAPTER IV. GYRO FILTERING

A. Introduction

The multiple star measurements from the video sensor are used in the VIP microprocessor to derive the three-axis pointing error signals. These signals are then available for use in the overall telescope control system. For a typical telescope pointing system, both gyro and star sensor measurements are available. A typical system will include a basic gyro stabilized gimbal using a high performance gyro with the star sensor measurements used to update the gyro. Since the system that will be used for the VIP system demonstrations and development uses analog rate integrating gyros (RIGs), the goal is to develop a gyro filter that will combine the three-axis pointing error signals available in the VIP microprocessor with the RIGs to provide the best possible performance.

The approach to be taken is to develop a discrete steady-state Kalman filter that combines the attitude error signals with the data from the RIG in the VIP microprocessor to provide update signals to the RIG and the stabilization system. Because it is intended that the VIP system be able to interface with different telescope pointing systems (i.e., the basic gyro stabilized gimbal), the filter design and implementation must not affect the basic gyro stabilization. The design of the filter must take into account the processing delays associated with the video sensors processing and interpolation and the multi-star processing time in the VIP microprocessor.

B. Design Considerations (Continuous Filter)

Although the attitude measurements from the video sensor and the multi-star processing are available at discrete intervals and although

a discrete filter will be developed, some of the key aspects of the design approach can be most easily illustrated by considering a continuous filter. Figure 10 represents a basic gyro stabilized gimbal. If continuous measurements of θ are available, then a simple filter can be developed to combine the attitude measurements with the RIG to provide a best estimate of θ for use in the gyro stabilization loop. If

$$\dot{\theta} = \omega , \qquad \omega_g = \omega + \omega_{gN} \tag{30}$$

where $\omega_{gN} \triangleq$ gyro rate noise, and $\omega_g \triangleq$ gyro rate signal, then

$$\dot{\theta} = \omega_g - \omega_{gN} \tag{31}$$

and if the attitude measurement

$$y = \theta + \theta_N \tag{32}$$

where $\theta \triangleq$ telescope attitude and $\theta_N \triangleq$ attitude measurement noise, then a simple filter can be developed as

$$\dot{\hat{\theta}} = \omega_g + K_1(z - \hat{\theta}) \tag{33}$$

where K_1 can be selected based on the desired noise and dynamic response. A block diagram of this filter is shown in figure 11 and it is easily seen that the filter can be incorporated into the gyro stabilization loop as shown in figure 12, where the RIG provides the integration required in the filter. This result has been previously noted [3].

Some important properties of this system can be derived considering simple RIG and telescope dynamics as shown in figure 13, where K_1 has been generalized to $G(S)$. The first item of interest is the disturbance response, θ/T_d, and it is easily shown that

$$\frac{\theta}{T_d} = \frac{1}{s^2 + H(s)} \tag{34}$$

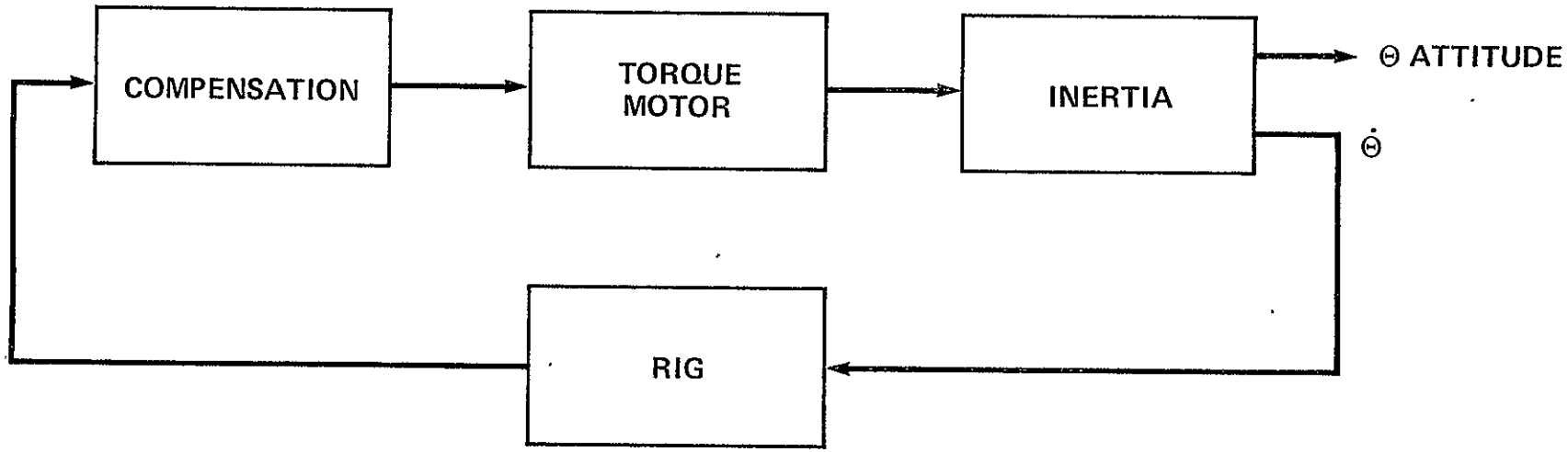

Figure 10.- Gyro stabilized gimbal.

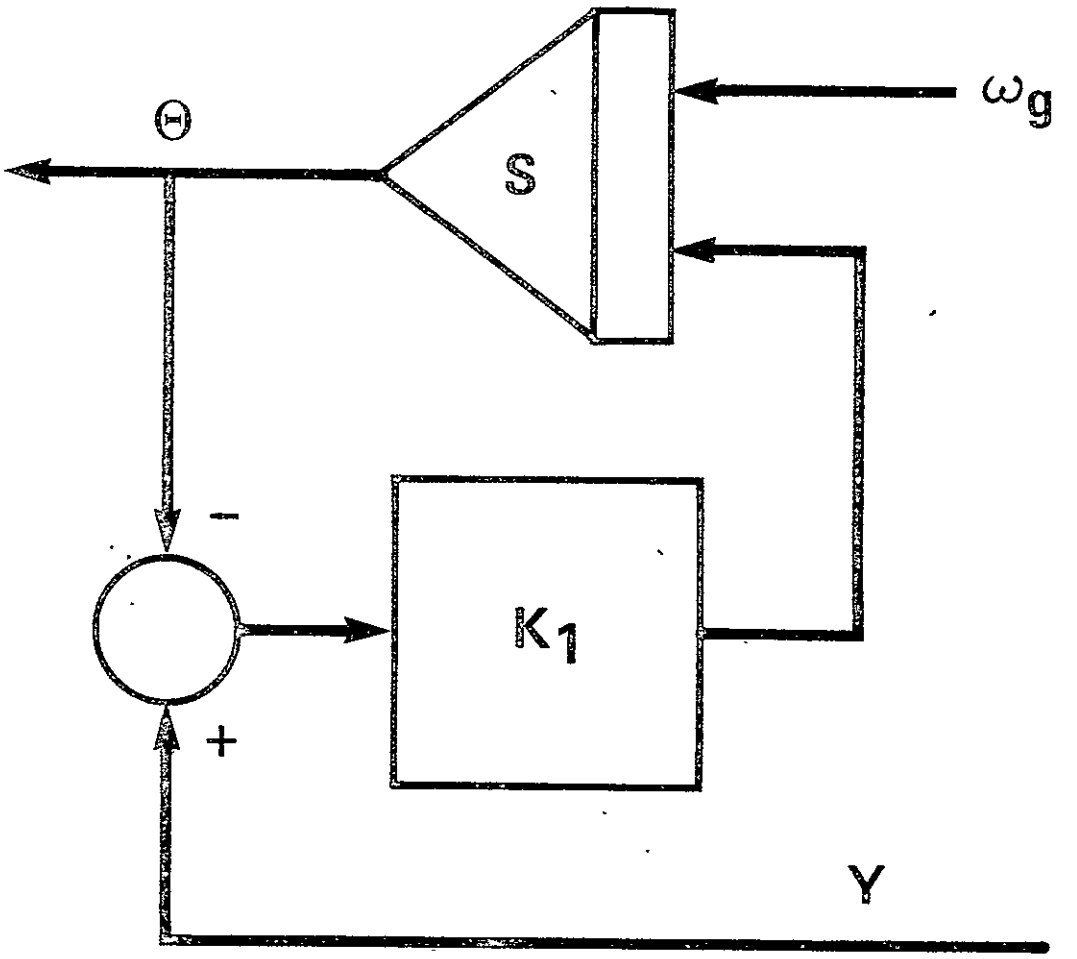

Figure 11.- Continuous filter.

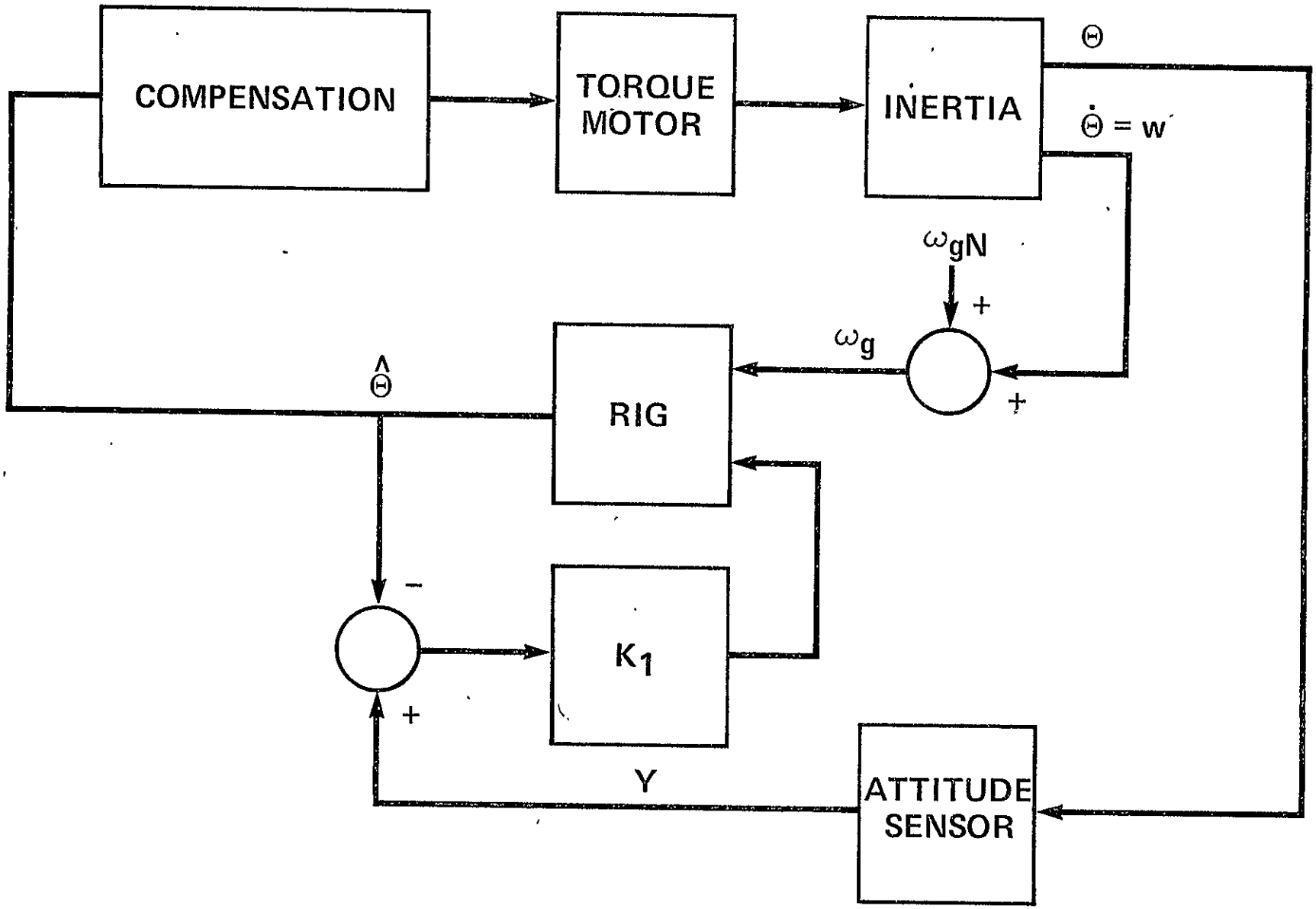

Figure 12.- Gyro stabilization with filter.

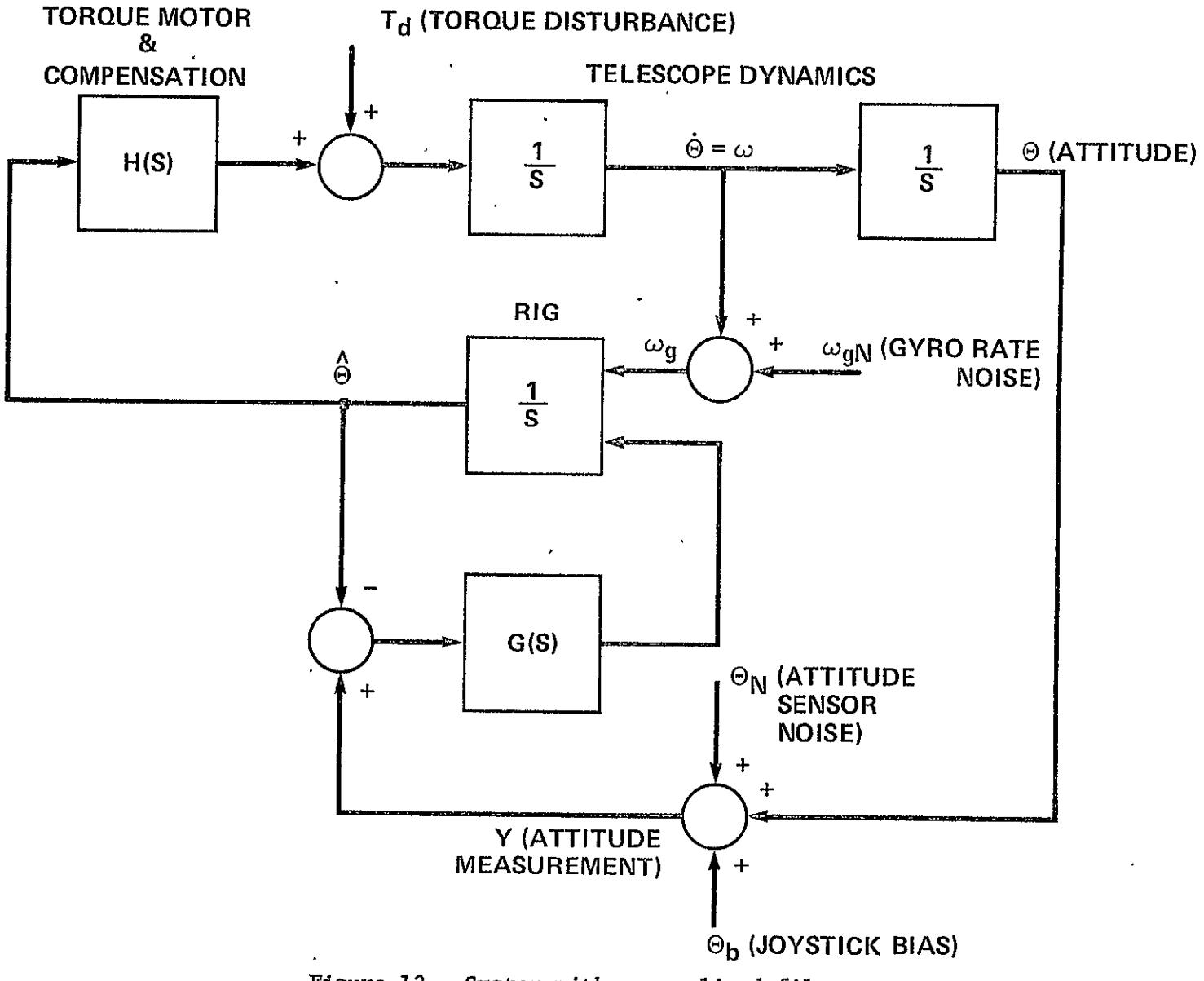

Figure 13.- System with generalized filter.

showing that the disturbance response is unaffected by the filter dynamics. For response of the telescope to a change in bias pointing position,

$$\frac{\theta}{\theta_s} = \frac{G(S)H(s)}{[s + G(S)][s + H(s)]} \tag{35}$$

indicating dependence on both the gyro stabilization and filter dynamics as expected and showing a separation effect, where the system closed loop poles are the poles of the filter and the poles of the basic gyro stabilization obtained independently.

Considering the noise performance of the system,

$$\frac{\theta}{\theta_N} = \frac{G(S)H(s)}{[s + G(S)][s + H(s)]} \tag{36}$$

and

$$\frac{\theta}{\omega_{gN}} = \frac{H(s)}{[s + G(S)][s + H(s)]} \tag{37}$$

If the performance of the filter, removed from the system, is considered,

$$\frac{\hat{\theta}}{\omega_{gN}} = \frac{1}{s + G(S)} \tag{38}$$

and

$$\frac{\hat{\theta}}{\theta_N} = \frac{G(S)}{s + G(S)} \tag{39}$$

If the gain and bandwidth of $H(s)$, the gyro stabilization compensation, are sufficiently high as is usually the case

$$\frac{H(s)}{s^2 + H(s)} \cong 1$$

over the frequency range of interest. This implies that the overall noise performance of the system will be close to the noise level predicted by the filter analysis.

The conclusions drawn from this analysis are:

1. The disturbance torque response of the system is determined by the gyro stabilization dynamics and is not affected by the filter dynamics.

2. The system response to a bias change in attitude is determined by both the filter and gyro stabilization dynamics.

3. The overall noise response of the system (gyro and video sensor noise) will be closely predicted by the noise given by the filter analysis.

These conclusions suggest that the filter can be designed independently of the basic gyro stabilization, and this approach will be used in the following sections. Although a continuous system was used for the discussion, the general results carry over to the discrete filter, as long as the basic structure used in the analysis applies. Furthermore, the conclusions are valid only insofar as the filter design adequately reflects the actual dynamics of the system. This will be an important consideration when the time delays associated with the video sensor and multi-star processing are considered, and these time delays will have to adequately modeled in the filter.

C. Discrete Filter

Since the attitude error signals are available at discrete instants rather than continuously, and since a digital computer is available, a discrete filter is suggested. From equations (30), a discrete model of the system is

$$\left.\begin{aligned} \theta(t_{i+1}) &= \theta(t_i) + \int_{t_i}^{t_{i+1}} (\omega_g - \omega_{gN})dt \\ y(t_{i+1}) &= \theta(t_{i+1}) + \theta_N(t_{i+1}) \end{aligned}\right\} \qquad (40)$$

and a discrete "Kalman" filter for this system is

$$\left.\begin{aligned} \hat{\theta}(t_{i+1})^- &= \hat{\theta}(t_i)^+ + \int_{t_i}^{t_{i+1}} \omega_g \, dt \\ \hat{\theta}(t_{i+1})^+ &= \hat{\theta}(t_{i+1})^- + K_1[y(t_{i+1}) - \hat{\theta}(t_{i+1})^-] \end{aligned}\right\} \tag{41}$$

Although the attitude error measurements are available only at discrete times, the gyro operates in continuous fashion, and it is desirable to implement the discrete filter making use of the gyro integration but not disturbing the basic gyro stabilization. Figure 14 is a block diagram of an implementation of the discrete filter that accomplishes this. The integration of the gyro is used to provide $\int_{t_i}^{t_{i+1}} \omega_g \, dt$ and the output of the gyro plus the update is the best estimate of the attitude error. The gyro output plus the last update provides the best estimate of the attitude error in between updates. The discrete Kalman filter can be used taking advantage of the gyro integration in a way similar to that of the continuous filter, and without breaking the basic high bandwidth gyro stabilization loop. Thus, analysis techniques available for the discrete Kalman filter can be used to obtain noise and dynamic performance and this filter can be properly mechanized.

More complex filters, which include gyro drift and time delays, can now be developed and analyzed. Time varying Kalman gains will not be considered because their computation would place an additional time burden on the VIP microprocessor, and constant gains should provide adequate response times.

Gyro dynamics will not be included in the filter models, because typical RIGs used in gyro stabilization loops have fast response, and the gyro dynamics will have little effect on the filter performance.

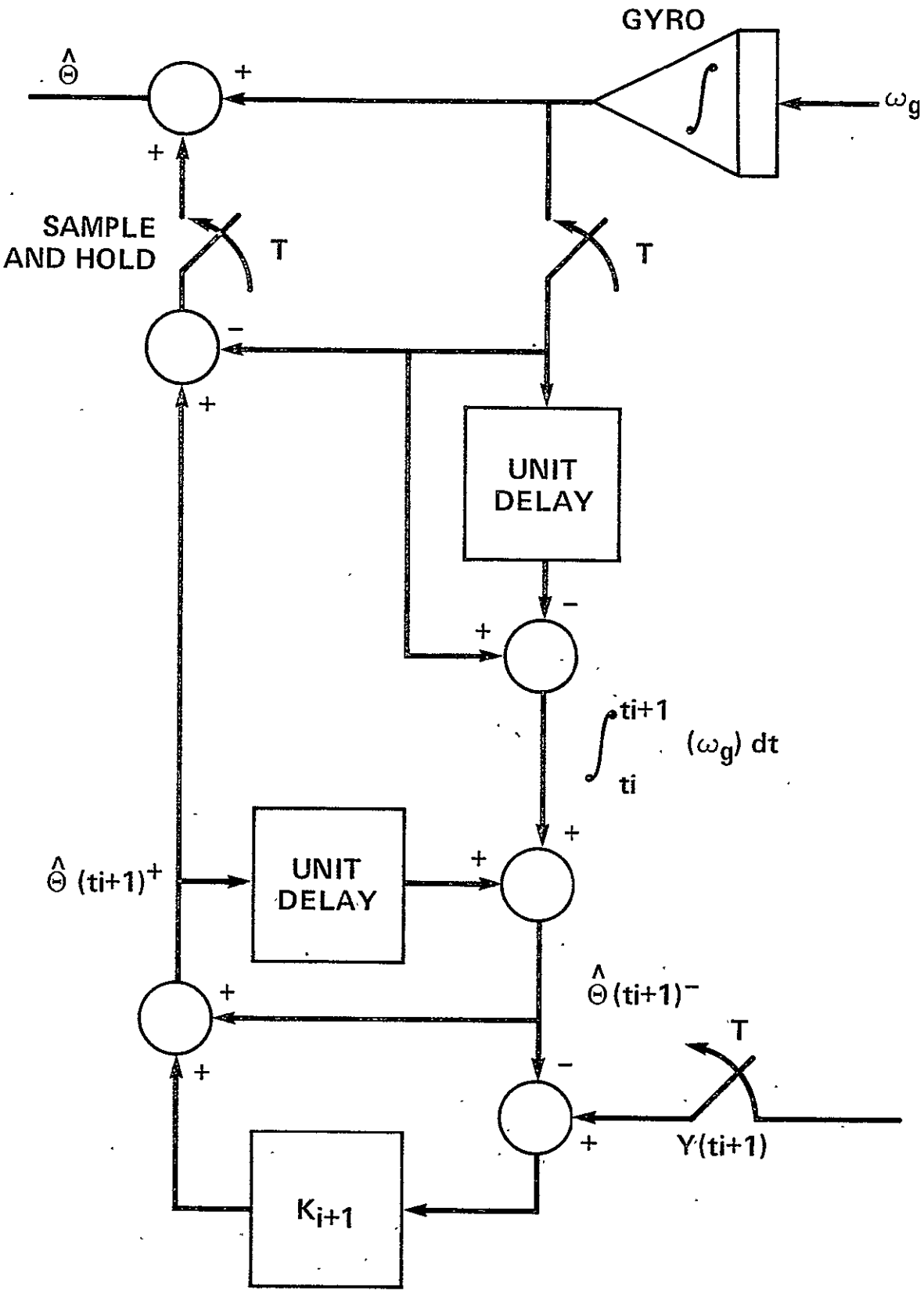

Figure 14.- Implementation of discrete filter.

D. Time Delays

Before proceeding to the design and analysis of the digital filters, the time delays to be represented in the filters must be defined. These time delays result from the interpolation performed by the video sensor, and from the multi-star processing performed in the VIP microprocessor.

The video sensor has a selectable integration time ranging from approximately 100 msec to 1 sec. Larger integration times provide increased sensitivity and allow the use of dimmer stars. After an integration cycle is complete, data are read from the CCD array and processed in the sensor's microprocessor to provide the interpolated position of the 10 brightest stars above a selected threshold. The interpolation process takes place during the next integration cycle; this operation is illustrated in figure 15. The minimum integration time for the video sensor is set by the time required for the data transfers and interpolation.

The VIP microprocessor takes the multi-star position data from the video sensor; it then performs the multi-star processing and the gyro filter equations, outputs data to a CRT display and gyros, and interrogates the control panel for commands. The VIP microprocessor operates asynchronously with the video sensor. When multi-star position measurements are available, the VIP microprocessor stops other activities and enters the data into memory. The most recent star position data are used in the multi-star processing. Upon completion of the multi-star processing, the gyro update equations are completed.

Because outputting the CRT display data and interrogating the control panel are interspersed with the multi-star processing, the multi-star processing requires almost the full cycle time of the VIP microprocessor. This cycle time depends on both the number of stars processed and on the

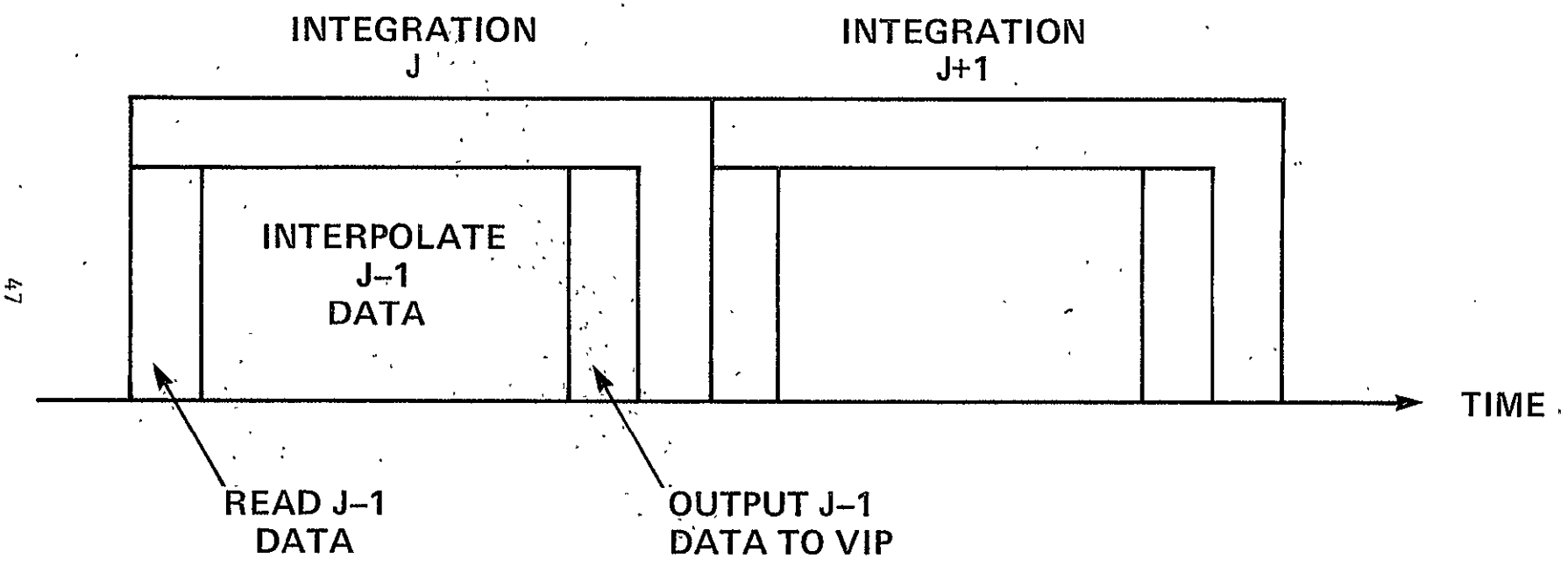

Figure 15.- Video sensor operation.

number of display options, and is generally constant once a particular display mode and number of guide stars have been selected. The cycle time of the VIP microprocessor will range between 300 and 500 msec. It is assumed that the time required for the gyro filter update is a very small portion of this time. The asynchronous operation of the two microprocessors is illustrated in figure 16. The result of this asynchronous operation is the occasional loss of star position data when the video sensor integration time is less than the VIP microprocessor time, and the occasional use of old data when the integration time is longer than the VIP microprocessor cycle time.

The ultimate time delay associated with the pointing error signals used to update the gyro filter in the VIP microprocessor depends on several things. One delay that is constant from cycle to cycle (VIP microprocessor) is the multi-star processing time which can be modeled as a unit delay of the VIP microprocessor cycle time. The other principal delay depends on when the star position data have been read into the VIP microprocessor. This delay is variable from cycle to cycle due to the asynchronous operation of the two microprocessors and will vary from the video sensor's interpolation time up to the full video sensor integration time; this is shown in figure 16. This does not count the time during which the star data to be used are being integrated in the video sensor; and this integration process is not modeled here.

The actual time delay will be variable from cycle to cycle (VIP microprocessor) and will range approximately from T_{VIP} to $T_{VIP} + T_{VSI}$ where $T_{VIP} \triangleq$ the VIP microprocessor cycle time and $T_{VSI} \triangleq$ the selected video sensor integration time. The approach used will be to model the

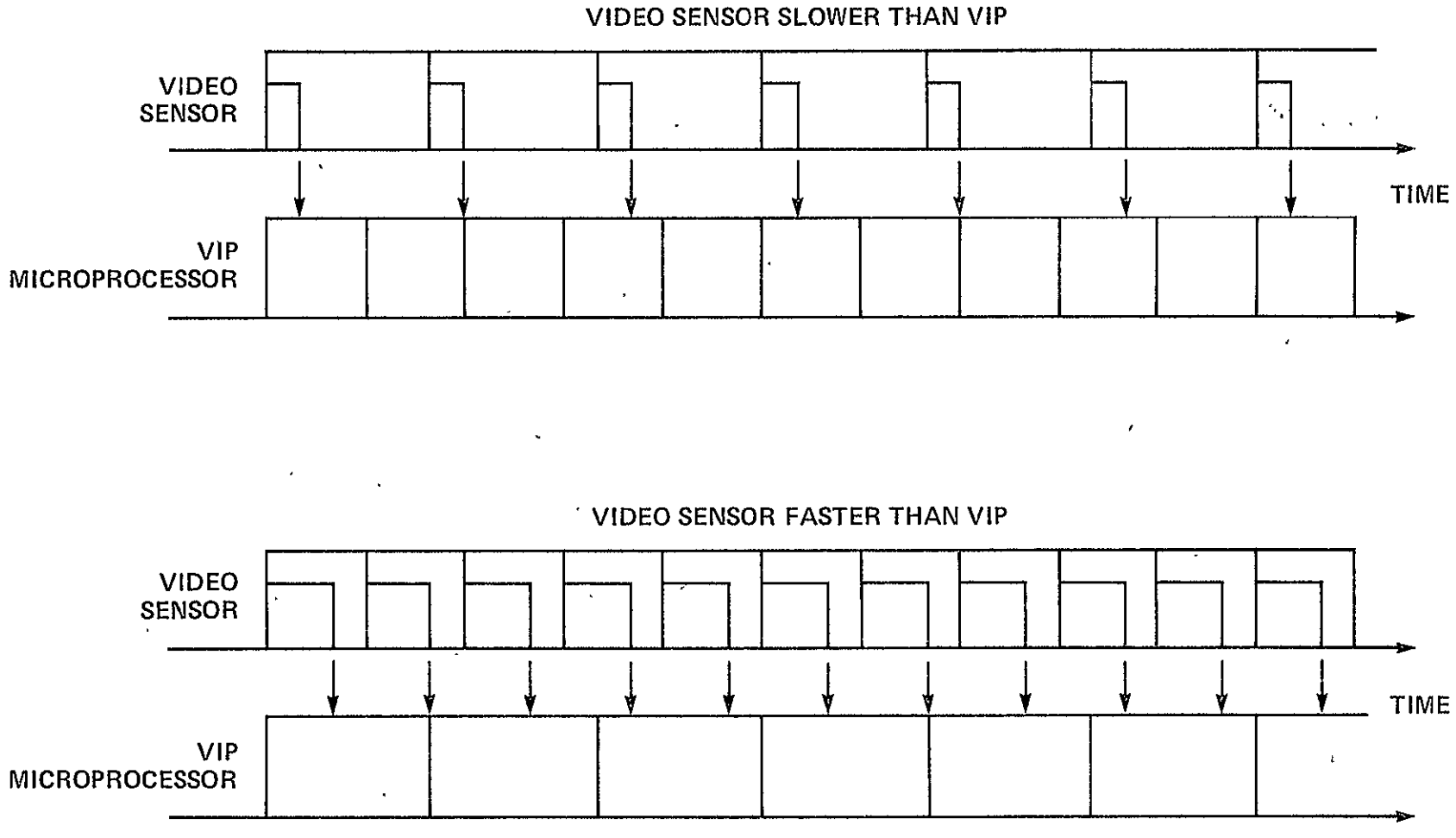

Figure 16.- Asynchronous operation.

time delay as unit delays of the VIP microprocessor, because the time delay is variable from cycle to cycle. For the case where $T_{VSI} < T_{VIP}$, a filter with one-unit delay should be satisfactory, and when $T_{VSI} > T_{VIP}$, two-unit delays will probably be required. A more complex approach would be to use electronic circuits separate from the VIP microprocessor to determine when the video sensor data were available, and thus determine the actual time delay for each cycle. These data could be used at each gyro filter update to select a filter model or gains for the exact delay. It is not thought that this complexity is needed, and the simulation results given later in this chapter verify the approach taken.

E. Filter Models

In the approach used here for the filter design and analysis, we start with the simplest filter and examine successively more complex filters. This provides better insight into the changes in filter noise performance and dynamics as a function of the complexity, and will ultimately allow a better understanding of how to select filters for the actual hardware. Gyro drift will be included in the filter models along with zero unit delays, or one- or two-unit delays. The integration process of the video sensor and the gyro high frequency dynamics are not included.

With these assumptions, there are six filter models of interest; they are listed below with the simplest model listed first.

1. One-State Filter

   θ Attitude

2. Two-State Filter

   θ Attitude

   D Gyro Drift

3. Two-State Filter

θ Attitude

θ_s Delayed Attitude (Unit Delay)

4. Three-State Filter

θ Attitude

D Gyro Drift

θ_s Delayed Attitude (Unit Delay)

5. Three-State Filter

θ Attitude

θ_{s1} Delayed Attitude (Unit Delay)

θ_{s2} Delayed Attitude (Unit Delay)

6. Four-State Filter

θ Attitude

D Gyro Drift

θ_{s1} Delayed Attitude (Unit Delay)

θ_{s2} Delayed Attitude (Unit Delay)

For each filter, DISC [5] will be used to analyze filter noise and dynamic performance, and, therefore, the state models must be developed. For use in the actual VIP hardware, the implementation of each filter similar to figure 14 must also be developed. The input to DISC is in the form

$$\left.\begin{aligned} \theta(t_{i+1}) &= \phi\theta(t_i) + \Gamma_1 u(t_i) + \Gamma_2 \omega(t_i) \\ y(t_i) &= H\theta(t_i) + v(t_i) \end{aligned}\right\} \qquad (42)$$

For filters that do not include drift, $\omega(t_i) \rightarrow N(0,Q_d)$ where Q_d depends on the time between updates and is the integral of the gyro rate noise. If $\omega_{gN} \rightarrow N(0,Q_g)$, then $Q_d = TQ_g$ where T is the time between updates. For filters that include drift,

$$\omega(t_i) = \begin{bmatrix} Q_g T + \frac{1}{3} D_N T^3 & -\frac{1}{2} D_N T^2 \\ -\frac{1}{2} D_N T^2 & D_N T \end{bmatrix}, \tag{43}$$

where Q_g is the gyro rate noise as before and D_N is the drift rate noise [4].

The unit time delays are included as shown below for filter 3:

Model:

$$\left.\begin{aligned} \theta(t_{i+1}) &= \theta(t_i) + \int_{t_i}^{t_{i+1}} (\omega_g - \omega_{gN})dt \\ \theta_s(t_{i+1}) &= \theta(t_i) \\ y(t_{i+1}) &= \theta_s(t_{i+1}) + v(t_{i+1}) \end{aligned}\right\} \tag{44}$$

Filter:

$$\left.\begin{aligned} \hat{\theta}(t_{i+1})^- &= \hat{\theta}(t_i)^+ + \int_{t_i}^{t_{i+1}} \omega_g \, dt \\ \hat{\theta}_s(t_{i+1})^- &= \hat{\theta}(t_i)^+ \\ \hat{\theta}(t_{i+1})^+ &= \hat{\theta}(t_{i+1})^- + K_1[y(t_{i+1}) - \hat{\theta}_s(t_{i+1})^-] \\ \hat{\theta}_s(t_{i+1})^+ &= \hat{\theta}(t_{i+1})^- + K_2[y(t_{i+1}) - \hat{\theta}_s(t_{i+1})^-] \end{aligned}\right\} \tag{45}$$

Table 5 shows the DISC models for the filters and figures 17 through 21 show the hardware implementations.

F. Observability

The filters which include the unit time delays have a singular ϕ matrix. Consider filter 3 (θ, θ_s)

$$\phi = \begin{bmatrix} 1 & 0 \\ 1 & 0 \end{bmatrix} \tag{46}$$

which is clearly singular due to the zero column. For processes defined by

$$\dot{x} = Fx \tag{47}$$

where F is finite, the resulting state transition matrix ϕ is nonsingular and

TABLE 5. DISC MODELS

$u_i \triangleq 0$

Filter	ϕ	Γ_2	H	w_{ti}	v_{ti}	x
$1(\theta)$	$[1]$	$[1]$	$[1]$	$[Q_d]$	$[R]$	$[\theta]$
$2(\theta,D)$	$\begin{bmatrix} 1 & -T \\ 0 & 1 \end{bmatrix}$	$\begin{bmatrix} 1 & 0 \\ 0 & 1 \end{bmatrix}$	$[1 \quad 0]$	$\begin{bmatrix} Q_d+\frac{1}{3}D_N T^3 & -\frac{1}{2}D_N T^2 \\ -\frac{1}{2}D_N T^2 & D_N T \end{bmatrix}$	$[R]$	$\begin{bmatrix} \theta \\ D \end{bmatrix}$
$3(\theta,\theta_s)$	$\begin{bmatrix} 1 & 0 \\ 1 & 0 \end{bmatrix}$	$\begin{bmatrix} 1 \\ 0 \end{bmatrix}$	$[0 \quad 1]$	$[Q_d]$	$[R]$	$\begin{bmatrix} \theta \\ \theta_s \end{bmatrix}$
$4(\theta,D,\theta_s)$	$\begin{bmatrix} 1 & -T & 0 \\ 0 & 1 & 0 \\ 1 & 0 & 0 \end{bmatrix}$	$\begin{bmatrix} 1 & 0 \\ 0 & 1 \\ 0 & 0 \end{bmatrix}$	$[0 \quad 0 \quad 1]$	$\begin{bmatrix} Q_d+\frac{1}{3}D_N T^3 & -\frac{1}{2}D_N T^2 \\ -\frac{1}{2}D_N T^2 & D_N T \end{bmatrix}$	$[R]$	$\begin{bmatrix} \theta \\ D \\ \theta_s \end{bmatrix}$
$5(\theta,\theta_{s1},\theta_{s2})$	$\begin{bmatrix} 1 & 0 & 0 \\ 1 & 0 & 0 \\ 0 & 1 & 0 \end{bmatrix}$	$\begin{bmatrix} 1 \\ 0 \\ 0 \end{bmatrix}$	$[0 \quad 0 \quad 1]$	$[Q_d]$	$[R]$	$\begin{bmatrix} \theta \\ \theta_{s1} \\ \theta_{s2} \end{bmatrix}$
$6(\theta,D;\theta_{s1},\theta_{s2})$	$\begin{bmatrix} 1 & -T & 0 & 0 \\ 0 & 1 & 0 & 0 \\ 1 & 0 & 0 & 0 \\ 0 & 1 & 0 & 0 \end{bmatrix}$	$\begin{bmatrix} 1 & 0 \\ 0 & 1 \\ 0 & 0 \\ 0 & 0 \end{bmatrix}$	$[0 \quad 0 \quad 0 \quad 1]$	$\begin{bmatrix} Q_d+\frac{1}{3}D_N T^3 & -\frac{1}{2}D_N T^2 \\ -\frac{1}{2}D_N T^2 & D_N T \end{bmatrix}$	$[R]$	$\begin{bmatrix} \theta \\ D \\ \theta_{s1} \\ \theta_{s2} \end{bmatrix}$

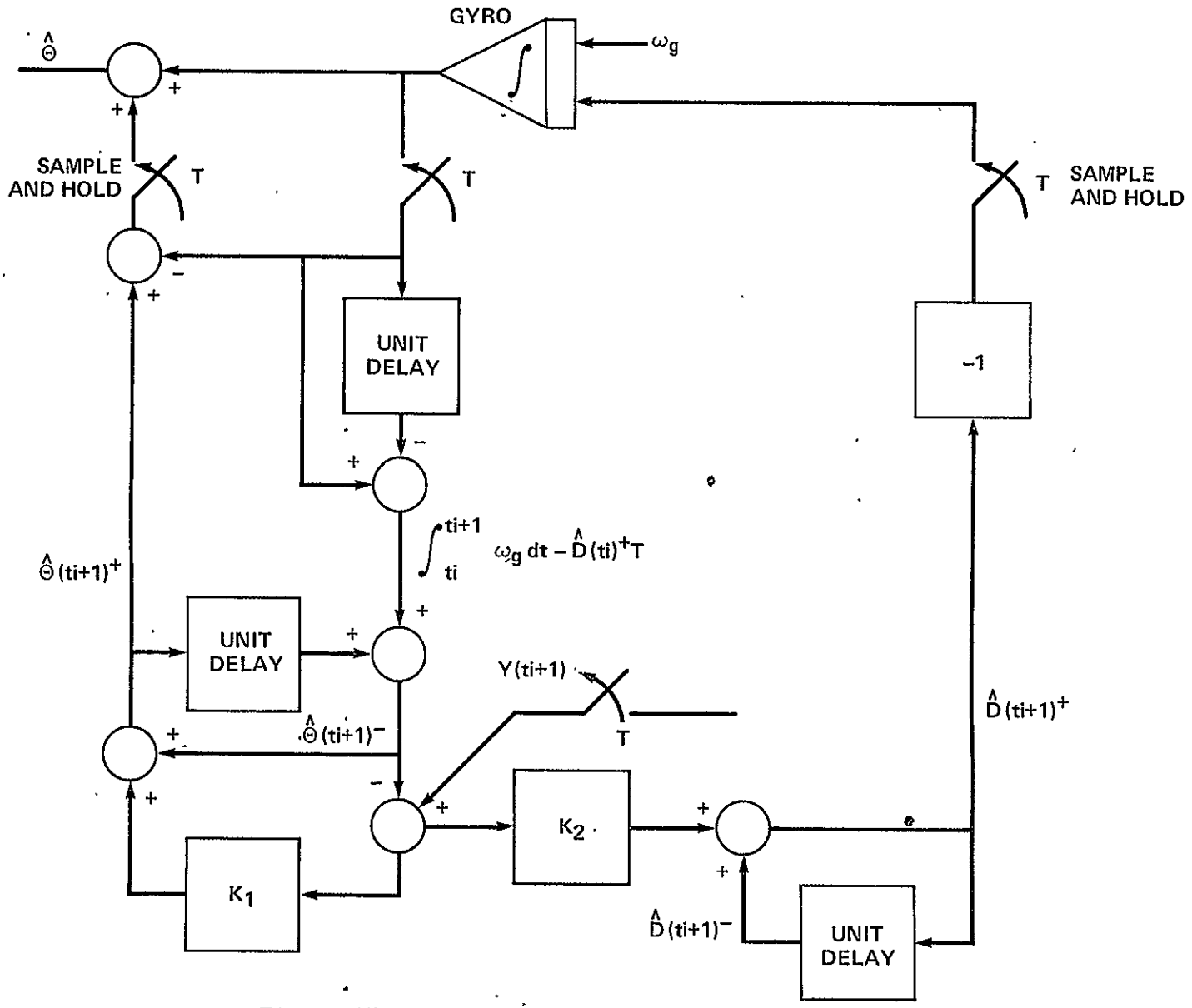

Figure 17.- Implementation of filter 2 (θ,D).

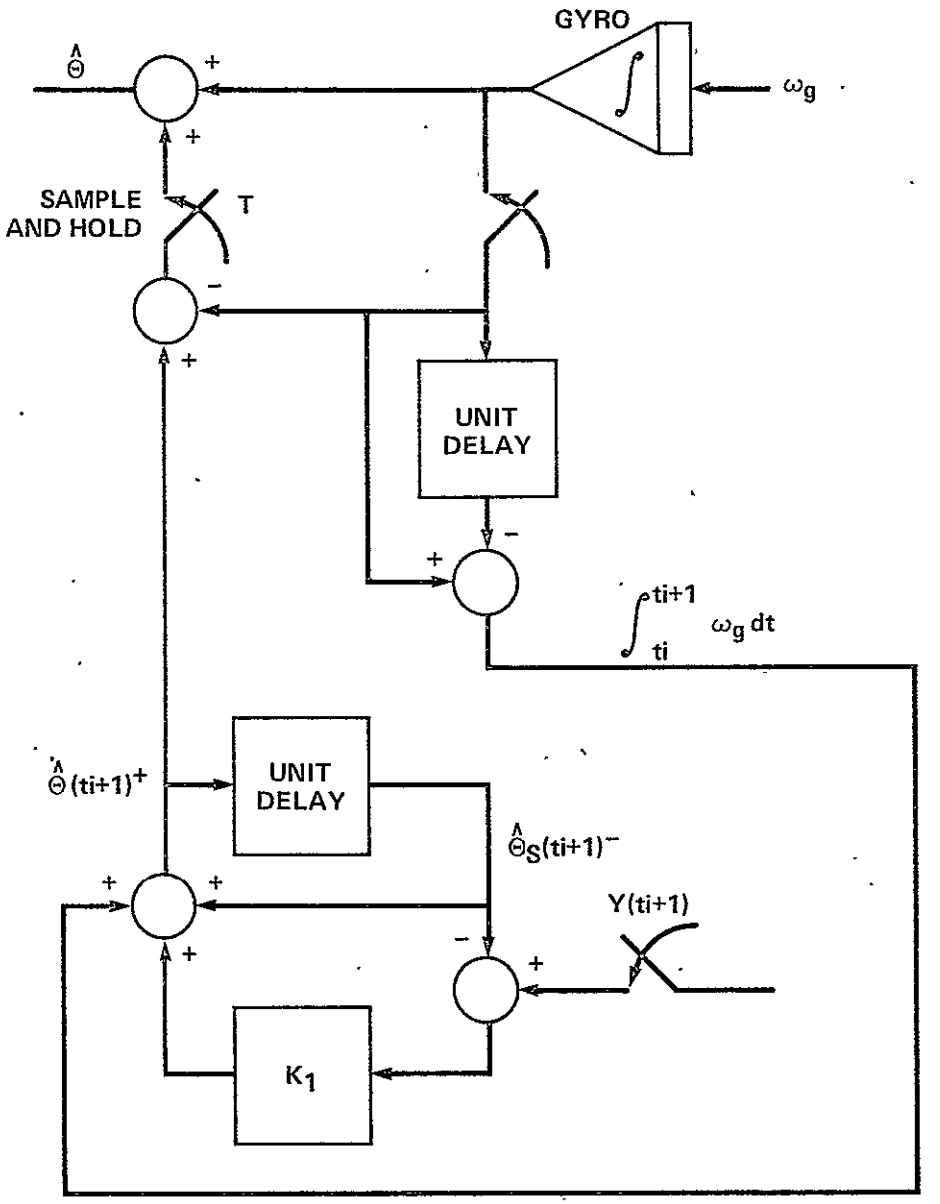

Figure 18.- Implementation of filter 3 (θ,θ_s).

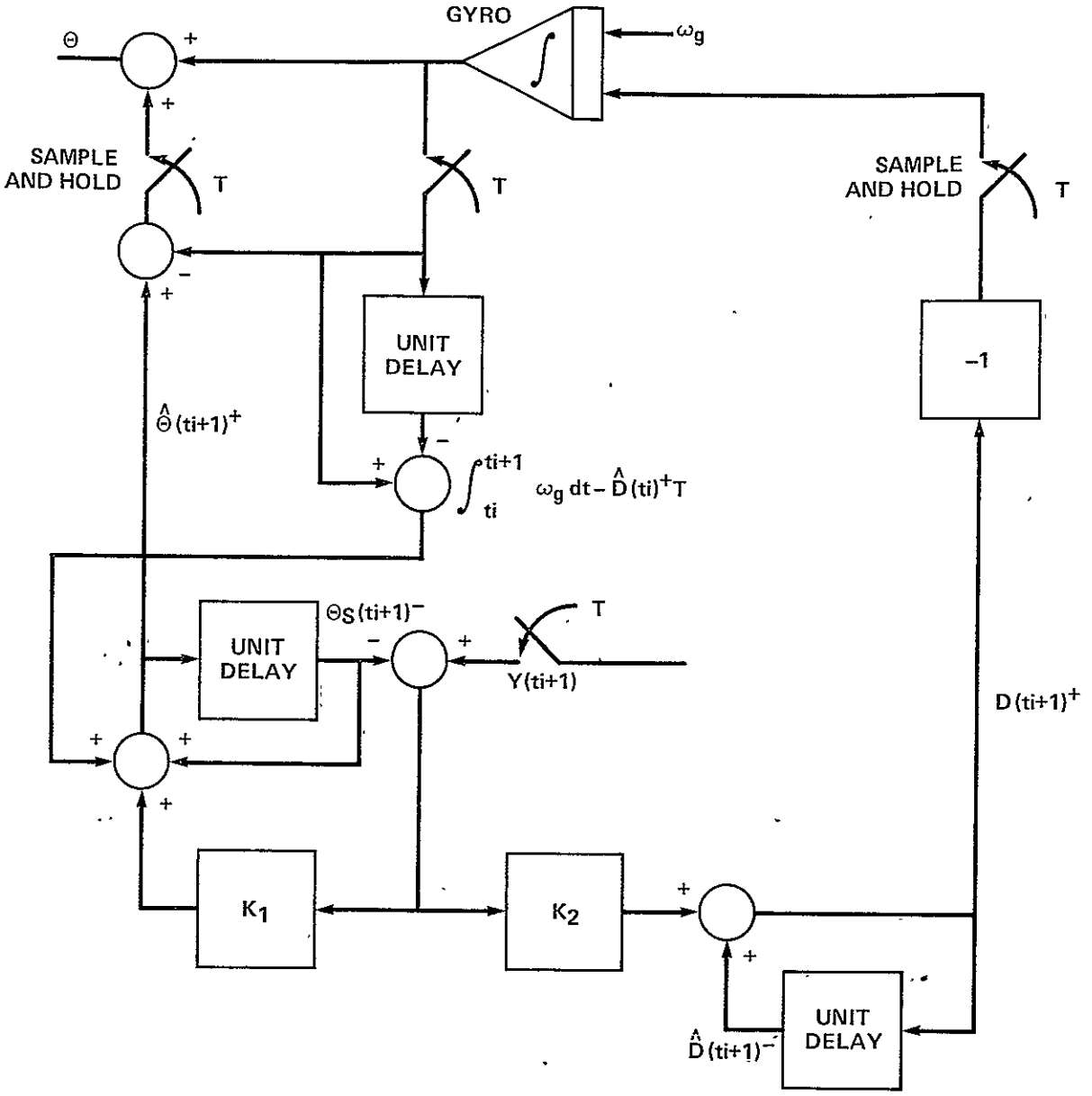

Figure 19.- Implementation of filter 4 (θ,D,θ_s).

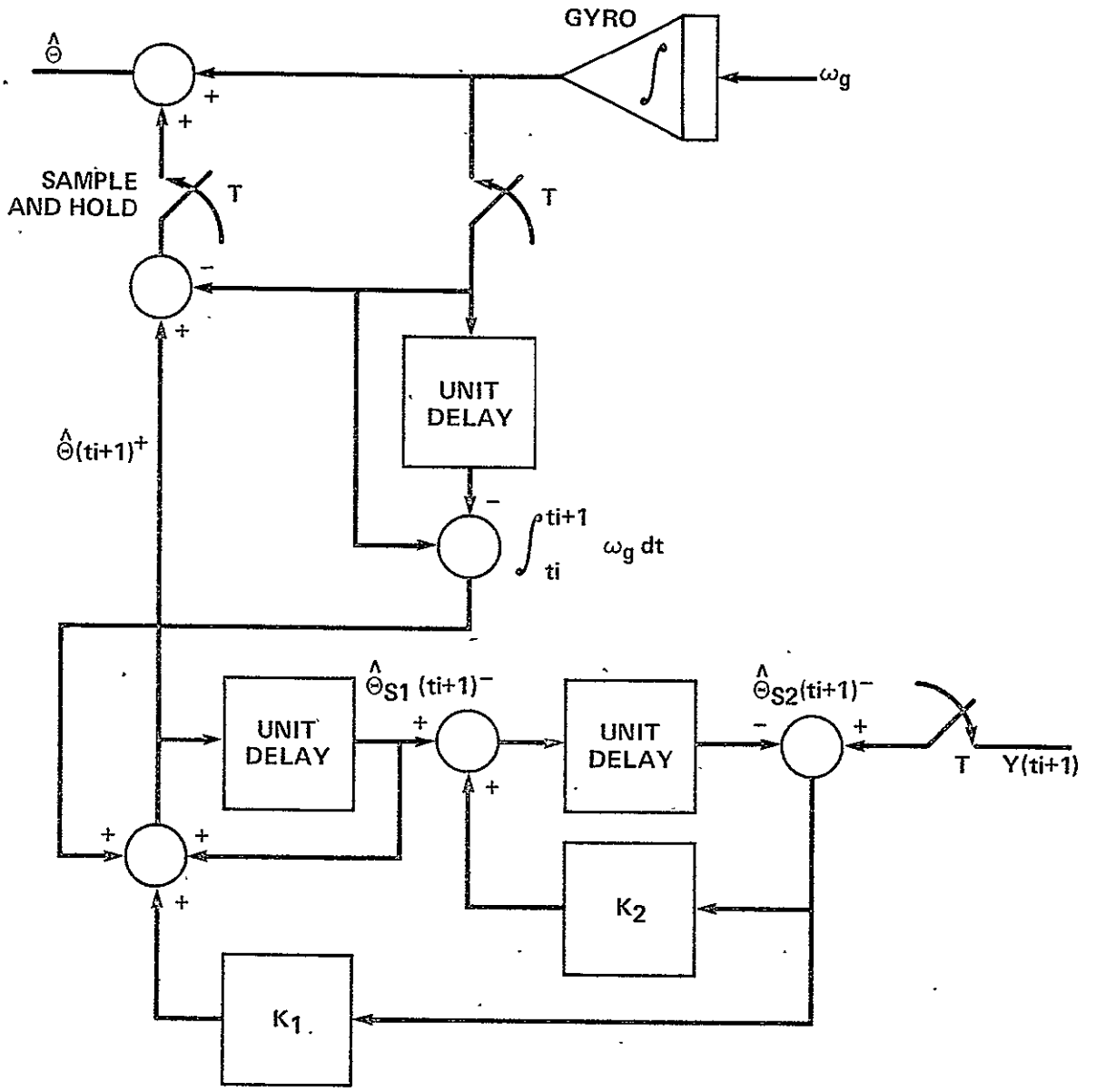

Figure 20.- Implementation of filter 5 ($\theta, \theta_{s1}, \theta_{s2}$).

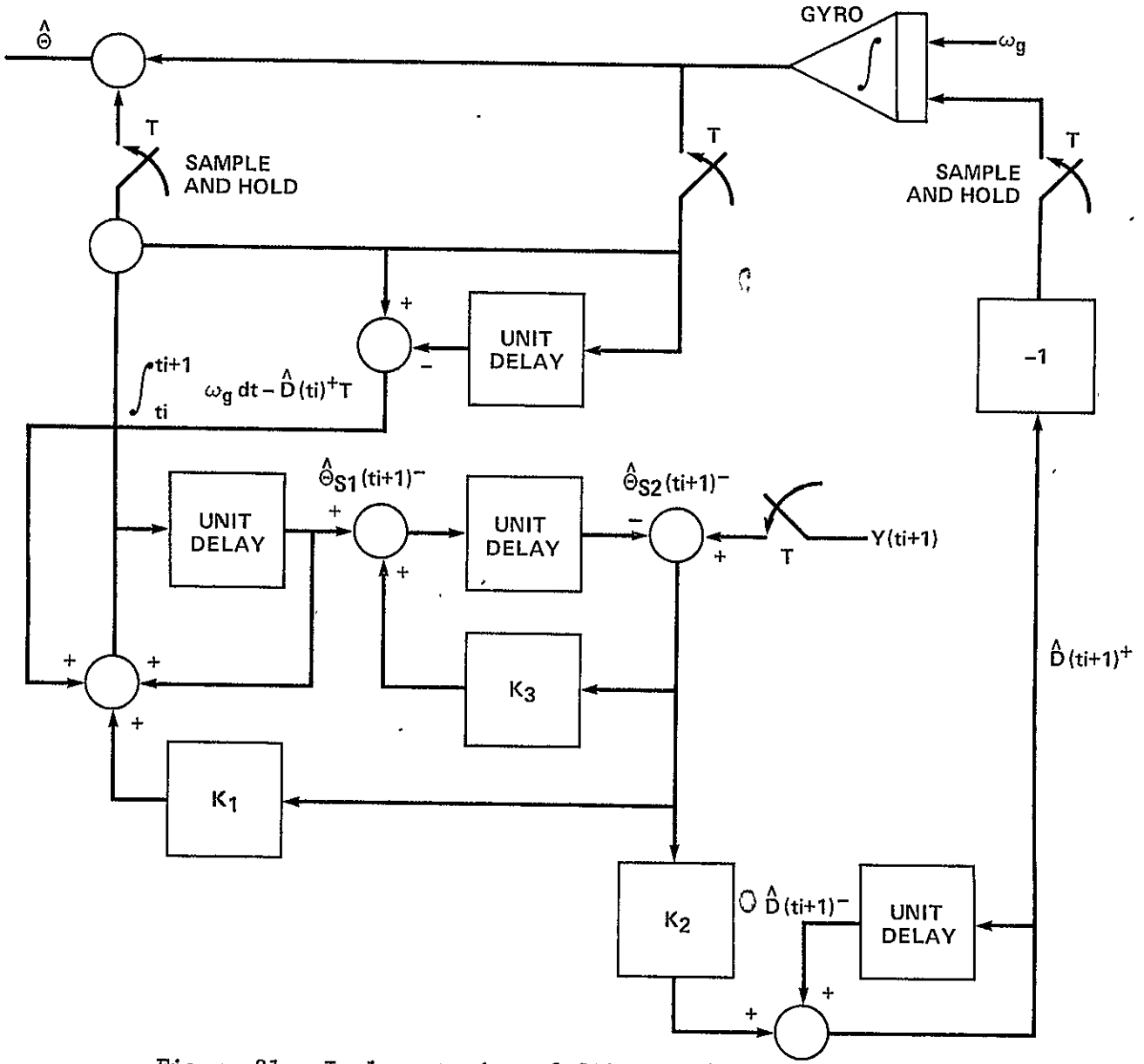

Figure 21.- Implementation of filter 6 (θ,D,θ_{s1},θ_{s2}).

$$\phi(t_2, t_1) = \phi^{-1}(t_1, t_2) \tag{48}$$

Therefore, $x(t_2)$ can be found given $x(t_1)$, or $x(t_1)$ can be found given $x(t_2)$. For our situation, the model is sufficient to find $x(t_2)$, given $x(t_1)$ by delaying, but the model is not sufficient to find $x(t_1)$, given $x(t_2)$; that is, $\phi^{-1}(t_2, t_1)$ does not exist. Considering the error equation for the filter

$$e(t_{i+1}) = [\phi - KH\phi]e(t_i) \tag{49}$$

where

$$[\phi - KH\phi] = \begin{bmatrix} 1-K_1 & 0 \\ 1-K_2 & 0 \end{bmatrix} \tag{50}$$

and the characteristic equation is $Z(Z + K_1 - 1)$. Clearly the roots of the error equation cannot be arbitrarily selected since K_2 has no effect and one root is always at the origin. The system is observable, however, since the rank [8] of

$$[H^T \mid \phi^T H^T] = \begin{bmatrix} 0 & 1 \\ 1 & 0 \end{bmatrix} \tag{51}$$

is two.

The singular ϕ matrix does present a problem for the use of DISC, because DISC calculates ϕ^{-1} [5]. This problem can be eliminated by introducing a small coupling term in ϕ,

$$\phi = \begin{bmatrix} 1 & 0 \\ 1 & \varepsilon \end{bmatrix} \tag{52}$$

Results from DISC for filter 3, using different values of ε, are shown in table 6 and show the insensitivity to ε. As ε gets smaller, one pole gets closer to the origin. For values of ε below 0.00001, the resulting M and P matrices begin to get unsymmetrical. It is interesting that $K_2 = K_1$ which is apparently important for minimization of

TABLE 6. DISC RESULTS (FILTER 3) VERSUS COUPLING TERM (ε); $Q_d = R = 1$

ε	M_θ	P_θ	K_1	K_2	Pole 1	Pole 2
0.01	2.6	1.6	0.62	0.62	0.37	0.01
0.001	2.6	1.6	0.62	0.62	0.38	0.001
0.00001	2.6	1.6	0.62	0.62	0.38	0.00001

the filter noise response, but K_2 has no apparent effect on the pole locations. Also K_2 is between 0 and 1 since if $K_2 = 0$

$$\hat{\theta}_s(t_{i+1})^+ = \hat{\theta}_s(t_{i+1})^- = \hat{\theta}(t_i)^+ \tag{53}$$

which ignores the current measurement, and if $K_2 = 1$

$$\hat{\theta}_s(t_{i+1})^+ = y(t_{i+1}) \tag{54}$$

which ignores past measurements.

This approach can be further justified by considering the error equation for filter 3 with the coupling term,

$$e(t_{i+1}) = \begin{bmatrix} 1 - K_1 & -\varepsilon K_1 \\ 1 - K_2 & -\varepsilon K_2 \end{bmatrix} e(t_i) \tag{55}$$

and the characteristic equation is

$$Z^2 + (K_1 - 1 + \varepsilon K_2)Z - \varepsilon(K_2 - K_1) \tag{56}$$

As ε gets small, the equation reduces to the characteristic equation obtained without the coupling term, and for small ε the roots are approximately $Z_1 = 1 - K_1$ and $Z_2 = 0$.

The approach to be taken, then, will be to use DISC for the filter analysis with small coupling terms for those filters that include the unit time delays. For filters 3 and 4, which include one delay, $\varepsilon = 0.00001$ is used, and for filters 5 and 6, which have two delays, an

ε is required for each delay and $\varepsilon = 0.01$ is used. A higher value of ε is required when the filter includes two delays because ε^2 terms result in the calculations and DISC has problems at correspondingly higher values of ε. This approach allows the use of DISC for the optimal filter analysis which provides a filter optimized for minimum noise response. The filters that include the unit delays do not allow arbitrary selection of filter poles. But the DISC analysis is not oriented to this design approach and the poles, which cannot be adjusted, are at or very close to $Z = 0$, and $Z = 0$ is associated with deadbeat response; that is, a response that decays in one cycle.

G. Filter Analysis

The purpose in this section is to analyze each of the six filters with DISC for various combinations of gyro and video sensor noise to obtain the filter noise performance (primarily θ) and dynamics. As previously stated, the system noise performance will closely approximate the filter noise performance (θ), if other sources, such as random disturbances and torque motor stiction, are neglected. The filter dynamics will play a large role in determining the overall closed loop response to step changes in the command attitude or joystick bias.

Each of the six filters is analyzed so that an intuitive feel for the effects of additional time delays and the inclusion of gyro drift can be gained. Appendix A contains a summary of the DISC runs made for each of the six filters. Table 7 shows the combinations of Q_d and R used for each filter. For filter 2, the values of

$$\omega(t_i) = \begin{bmatrix} Q_d + \frac{1}{3} D_N T^3 & -\frac{1}{2} D_N T^2 \\ -\frac{1}{2} D_N T^2 & D_N T \end{bmatrix} \tag{57}$$

TABLE 7. COMBINATIONS OF Q_d AND R FOR FILTER ANALYSIS

Q_d	0.1	1	10	100
R	0.1	0.1	0.1	0.1
	1	1	1	1
	10	10	10	10
	100	100	100	100

$Q_d \triangleq (\text{arc sec/sec})^2$

$R \triangleq (\text{arc sec})^2$

are tabulated in table 8. Gyro drift rate noise, D_N, must be included so that all filter states are driven by some disturbance noise. The DISC analysis for filters 4 and 6 was performed only with $D_N = 1$ because the results from filter 2 with $D_N = 0.1$ indicated poor role locations and slow filter dynamics.

Results for the one-state filter can be examined first since the more complex filters will relate to these results. It should be remembered that M_θ is the covariance of the attitude estimate just prior to a filter update, and that P_θ is the covariance just after a filter update. The total system (filter plus gyro stabiliation) noise response depends on both M_θ and P_θ since the gyro is the primary reference between filter updates, and M_θ is closely related to the gyro rate noise.

For presentation of the data, M_θ and P_θ can be normalized with respect to R; figure 22 is a plot of M_θ/R and P_θ/R for various Q_d/R. For large Q_d/R, M_θ approaches Q_d, and P_θ approaches R as expected. For Q_d/R small, M_θ approaches P_θ in between Q_d and R. Figure 23 is a plot of M_θ/P_θ versus Q_d/R, and illustrates these conclusions. Figure 24 is a plot of pole location versus Q_d/R; for

TABLE 8. VALUES OF ω_i for Q_d, D_N, and T

$D_N = 1$

Q_d \ T	0.25	0.5
0.1	$\begin{bmatrix} 0.1021 & -0.0125 \\ -0.0125 & 0.1 \end{bmatrix}$	$\begin{bmatrix} 0.1083 & -0.025 \\ -0.025 & 0.1 \end{bmatrix}$
1	$\begin{bmatrix} 1.0021 & -0.0125 \\ -0.0125 & 0.1 \end{bmatrix}$	$\begin{bmatrix} 1.0083 & -0.025 \\ -0.025 & 0.1 \end{bmatrix}$
10	$\begin{bmatrix} 10.0021 & -0.0125 \\ -0.0125 & 0.1 \end{bmatrix}$	$\begin{bmatrix} 10.0083 & -0.025 \\ -0.025 & 0.1 \end{bmatrix}$
100	$\begin{bmatrix} 100.0021 & -0.0125 \\ -0.0125 & 0.1 \end{bmatrix}$	$\begin{bmatrix} 100.00833 & -0.025 \\ -0.025 & 0.1 \end{bmatrix}$

$D_N = 1$

Q_d \ T	0.25	0.5
0.1	$\begin{bmatrix} 0.121 & -0.125 \\ -0.125 & 1 \end{bmatrix}$	$\begin{bmatrix} 0.183 & -0.25 \\ -0.25 & 1 \end{bmatrix}$
1	$\begin{bmatrix} 1.021 & -0.125 \\ -0.125 & 1 \end{bmatrix}$	$\begin{bmatrix} 1.083 & -0.25 \\ -0.25 & 1 \end{bmatrix}$
10	$\begin{bmatrix} 10.021 & -0.125 \\ -0.125 & 1 \end{bmatrix}$	$\begin{bmatrix} 10.083 & -0.25 \\ -0.25 & 1 \end{bmatrix}$
100	$\begin{bmatrix} 100.021 & -0.125 \\ -0.125 & 1 \end{bmatrix}$	$\begin{bmatrix} 100.083 & -0.25 \\ -0.25 & 1 \end{bmatrix}$

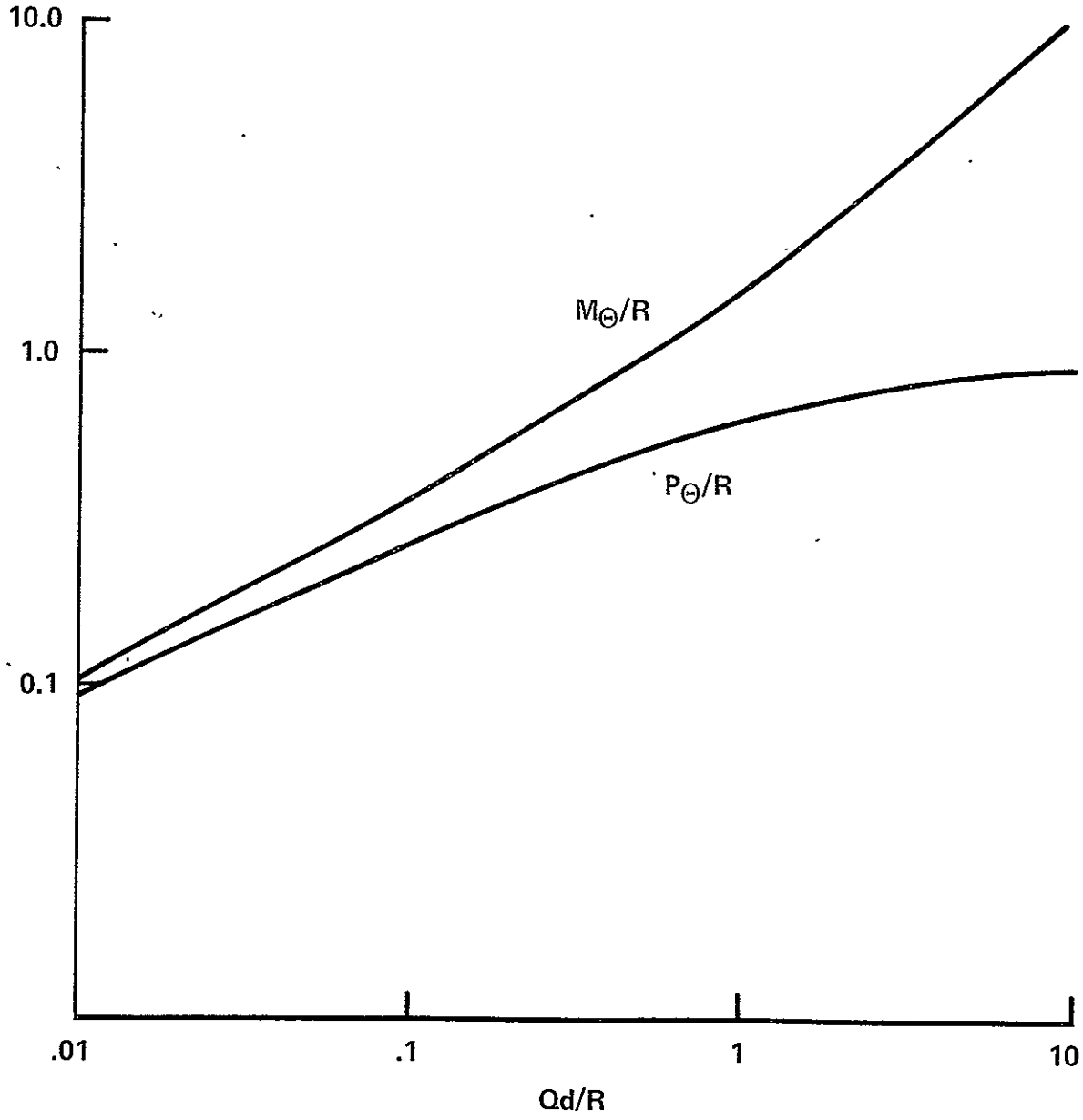

Figure 22.- Plot of M_θ/R and P_θ/R for filter 1 (θ) versus Q_d/R.

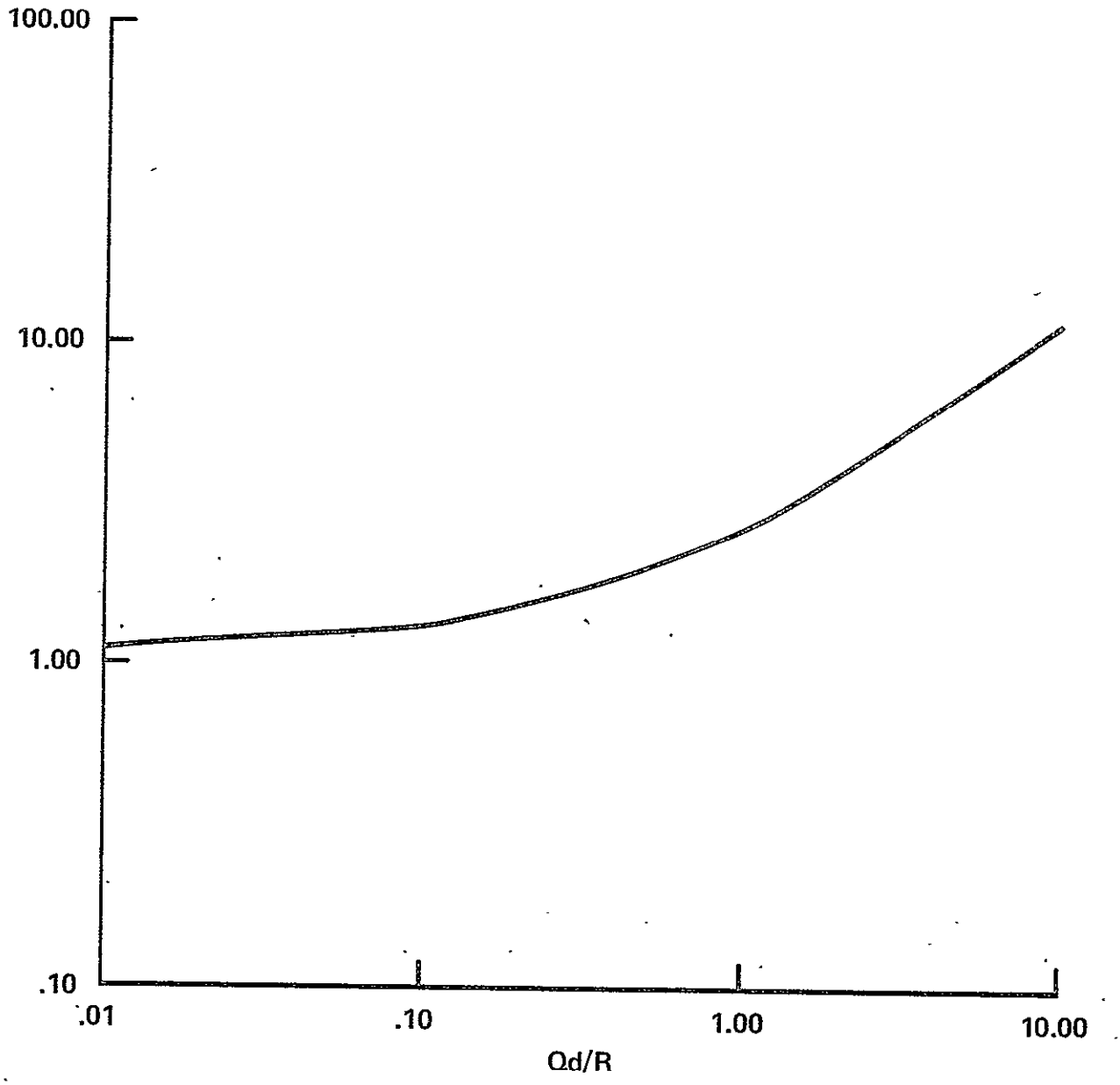

Figure 23.- Plot of M_θ/P_θ for filter 1 (θ) versus Q_d/R.

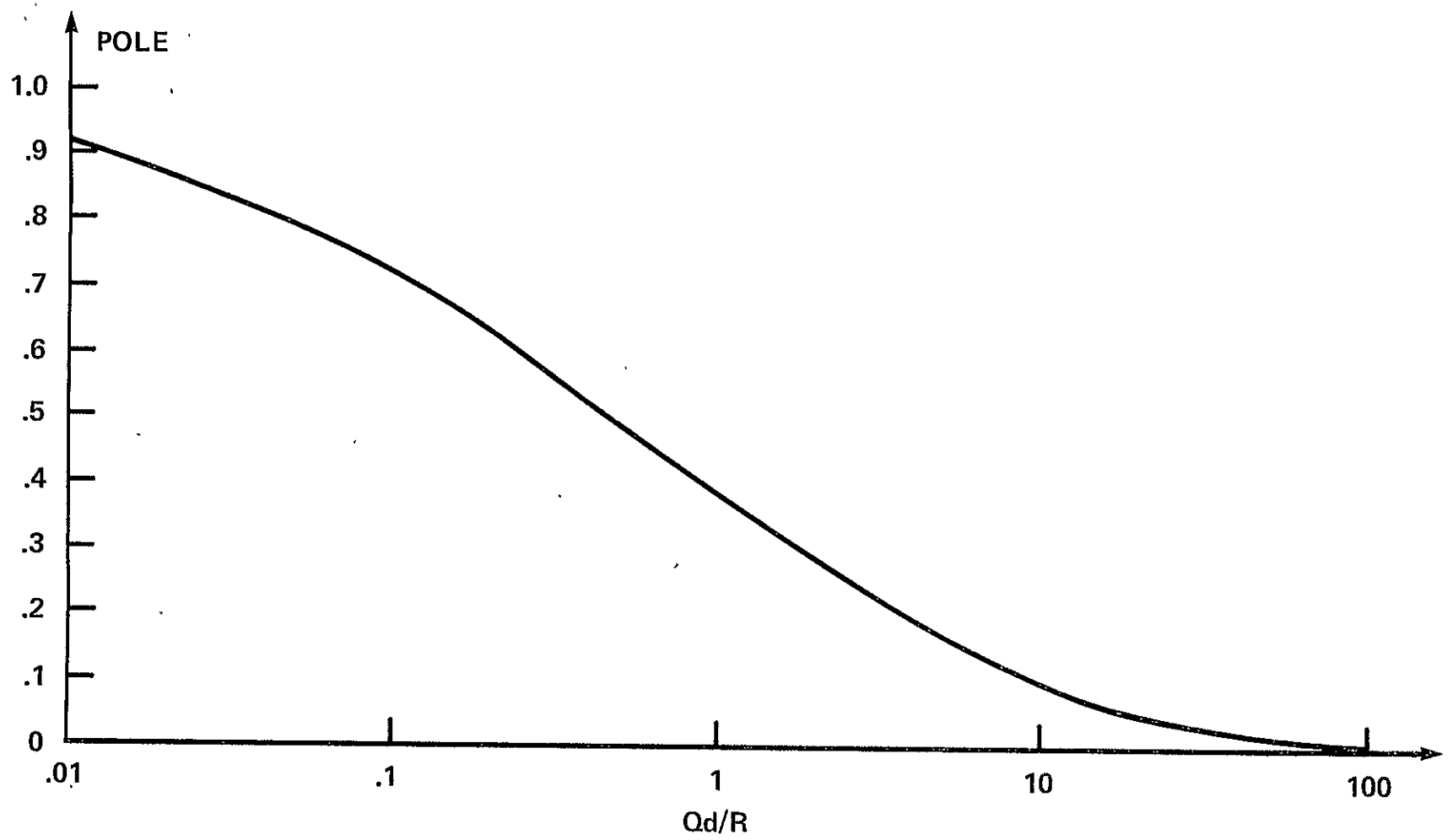

Figure 24.- Plot of pole location for filter 1 (θ) versus Q_d/R.

large Q_d/R, the pole is close to $Z = 0$ indicating rapid decay of initial condition errors and for Q_d/R small, the pole is close to $Z = 1$ indicating slow response.

From these data, it can be concluded that Q_d/R should be selected so that

$$0.1 < \frac{Q_d}{R} < 10$$

This is because of the following:

(1) If $Q_d/R > 10$, pole location will be good but M_θ/P_θ will be large indicating that the filter is not performing much smoothing. $P_\theta/R \sim 1$, that is, at the filter updates the filter follows the video sensor data. Since M_θ/P_θ is large, system noise performance will not have been improved a great deal by the filter.

(2) If $Q_d/R < 0.1$, M_θ/P_θ will be close to 1, but pole location will be close to $Z = 1$ and dynamic performance will be poor.

For filter 2 (θ,D), the results are similar to those for filter 1 with the exception of the additional pole and somewhat larger M_θ and P_θ. The poles generally consist of two real poles, one of which depends on Q_d/R and is near or equal to the pole of filter 1, and the drift estimator pole which depends on D_N/Q_d, as shown in figure 25. For large Q_d/D_N the additional pole approaches $Z = 1$ and the filter response would be sluggish. For values of Q_d/D_N small, M_θ and P_θ are somewhat larger than for filter 1 and the effect is worse for larger values of T. For Q_d/D_N large, M_θ and P_θ are close to the values obtained from filter 1.

From filter 3 (θ,θ_s) and filter 5 $(\theta,\theta_{s1},\theta_{s2})$, which include one- and two-unit delays, respectively, the primary effect is poorer noise performance; that is, larger values of M_θ and P_θ relative to filter 1.

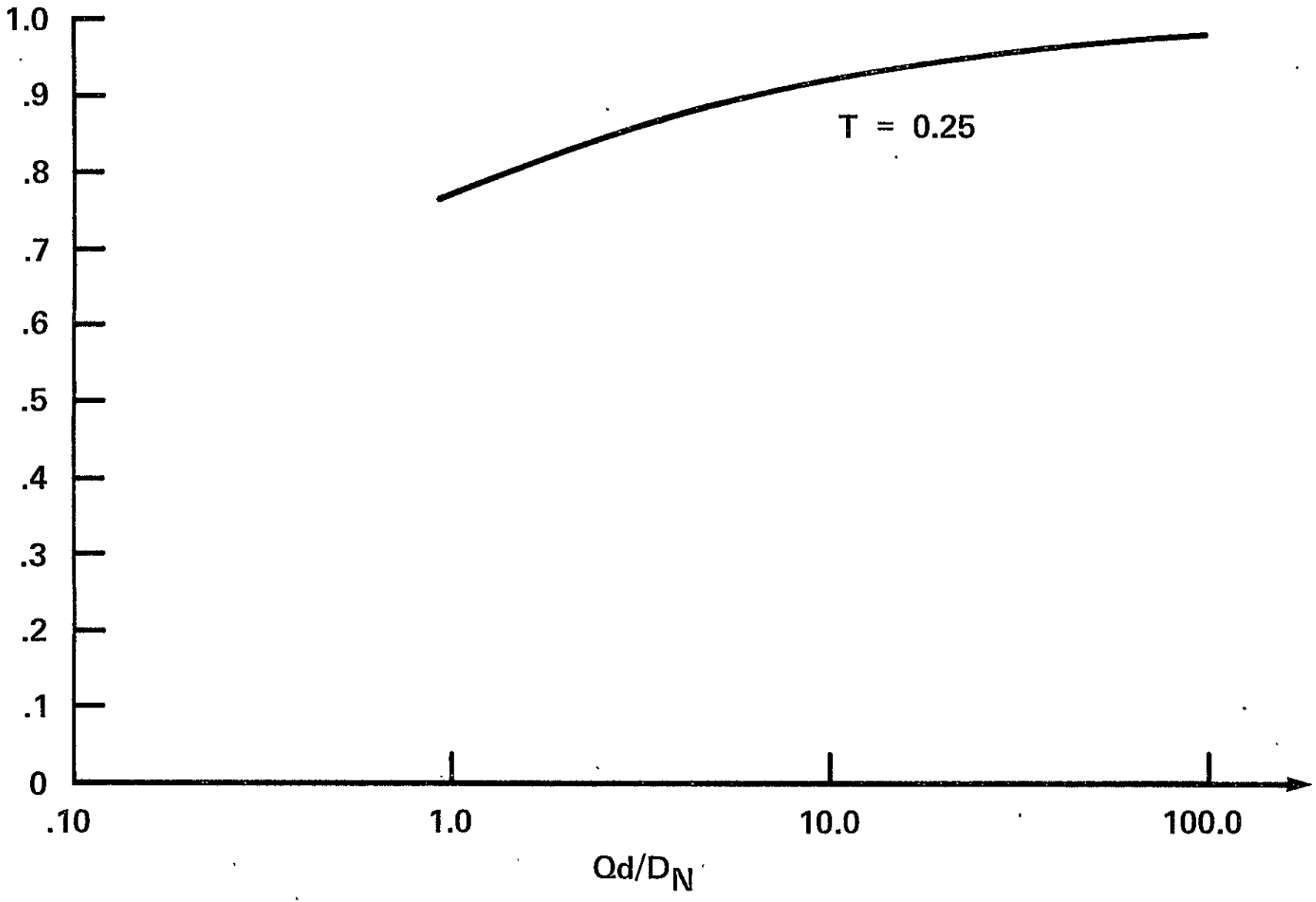

Figure 25.- Plot of drift estimate pole location for filter 2 (θ,D) versus Q_d/D_N.

For both filters, the gains are identical and equal to the gain obtained for filter 1. The response consists of one or two poles close to or at the origin plus the real pole obtained from filter 1. Figure 26 is a comparison of M_θ for filters 3 and 5 versus filter 1, and figure 27 is a similar P_θ comparison. For small Q_d/R, the time delays do not have great effect while for large Q_d/R, the effect is pronounced, particularly on P_θ.

For filter 4 (θ,D,θ_s) and filter 6 $(\theta,D,\theta_{s1},\theta_{s2})$, which include both drift and one- and two-unit delays, respectively, the results are generally a composite of the simpler filters. Only the cases with drift noise $D_N = 1$ were used since it was found with filter 2 that $D_N = 0.1$ results in a pole close to $Z = 1$, even for values of $Q_d = 0.1$ and 1.0. For filter 4, the pole locations are generally close to the pole locations for filter 2, with the addition of a pole close to $Z = 0$ due to the unit delay. Noise performance (M_θ,P_θ) is generally worse than that of filter 3 (θ,θ_s) at low values of Q_d/D_N, and approaches the values of filter 3 for large Q_d/D_N (see fig. 28). A similar comparison can be made between filters 6 and 2 for pole location, and between filters 6 and 5 for noise performance (see fig. 29).

It is important to note for the filters that contain gyro drift rate noise, D_N, that the large relative value of D_N used for the DISC is not representative of the physical situation. For most medium to high performance rate integrating gyros, D_N will be much less than Q_d. For filters 4 and 6, this is representative of values of $Q_d = 10$ or 100 where $D_N = 1$, and for these cases, noise performance is relatively unaffected by D_N, and closely approximates the noise performance obtained for filters 3 and 5. The only problem with large Q_d/D_N is the low drift gain and pole approaching $Z = 1$, which will cause poor

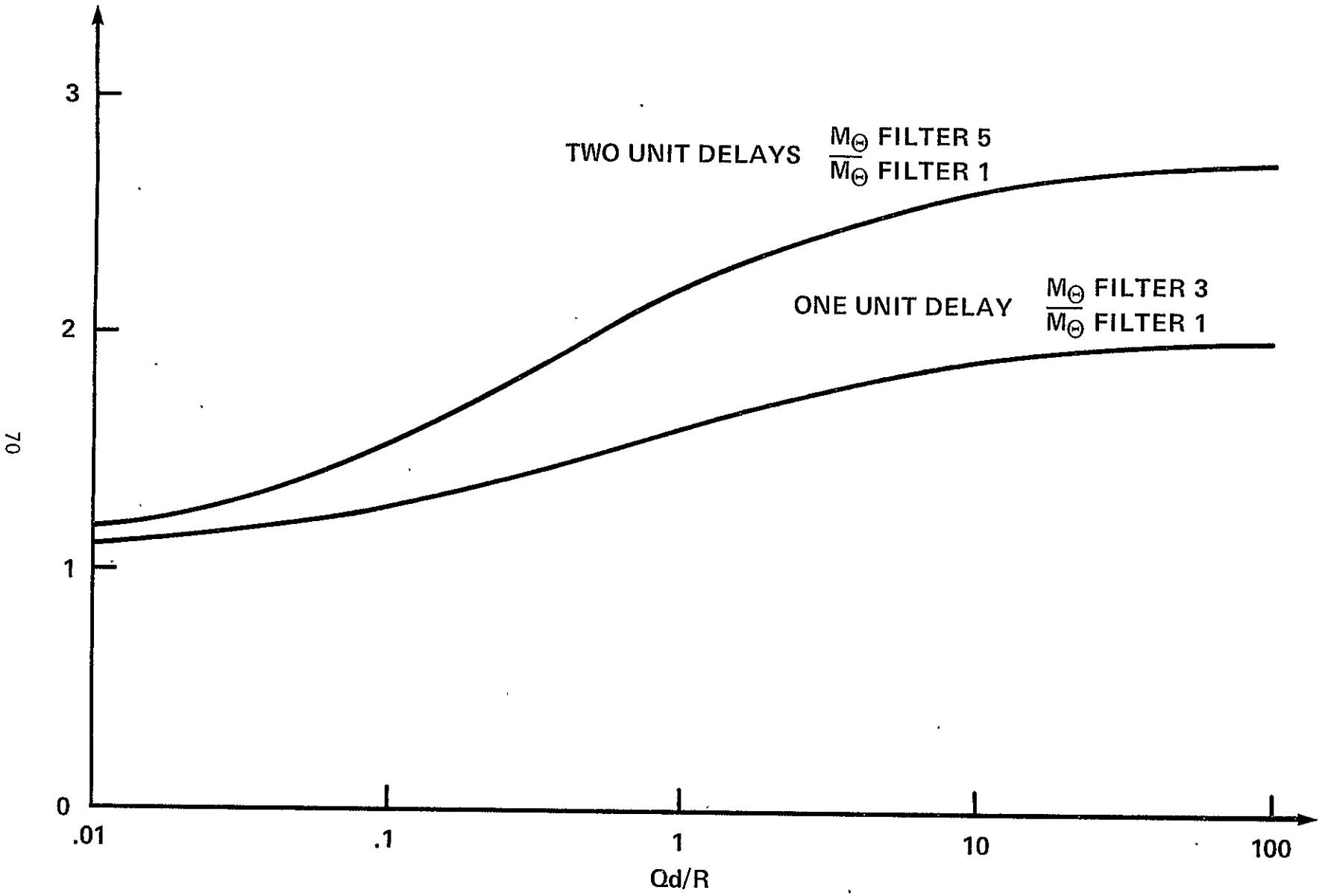

Figure 26.- M_θ comparison.

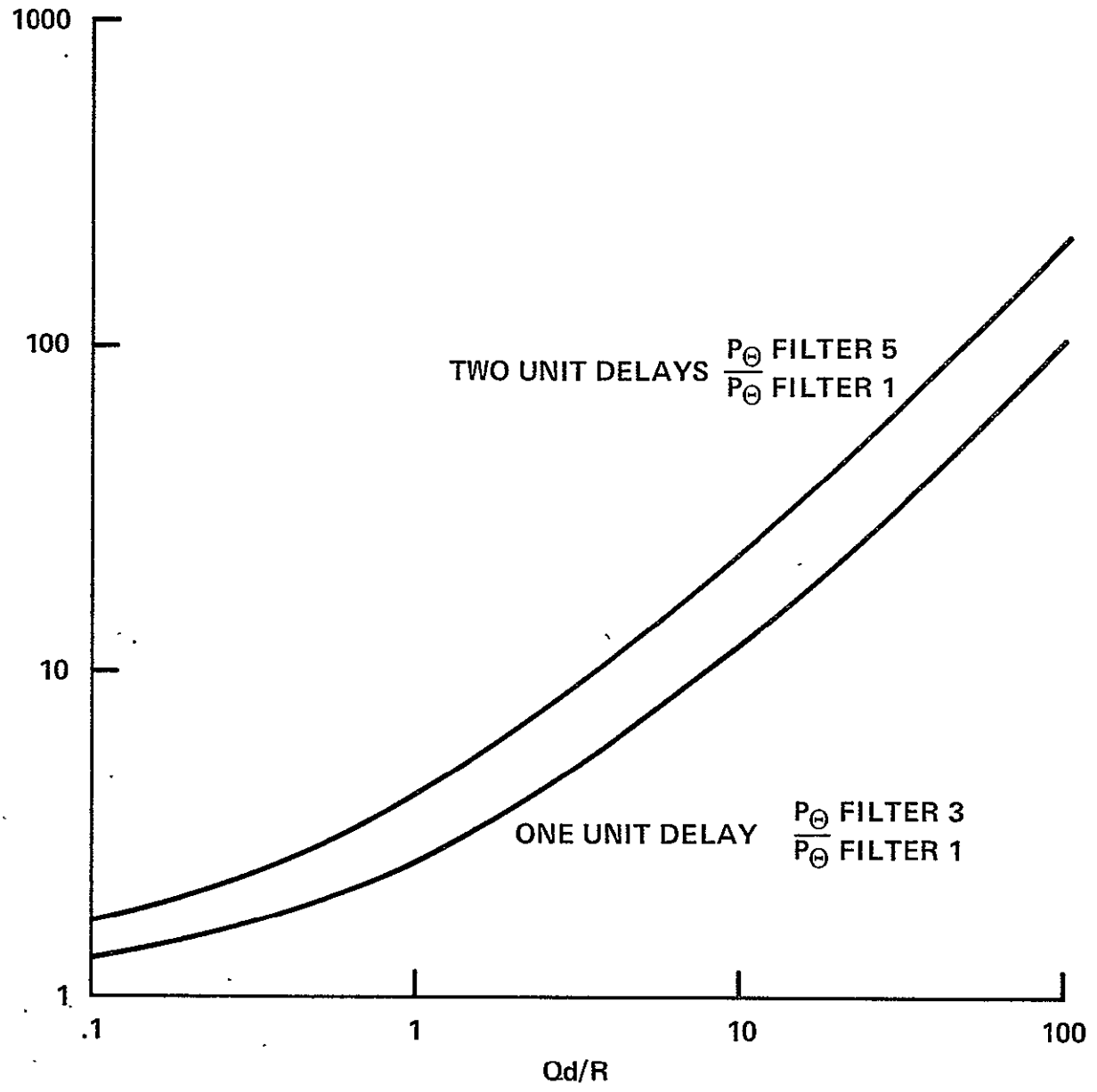

Figure 27.- P_θ comparison.

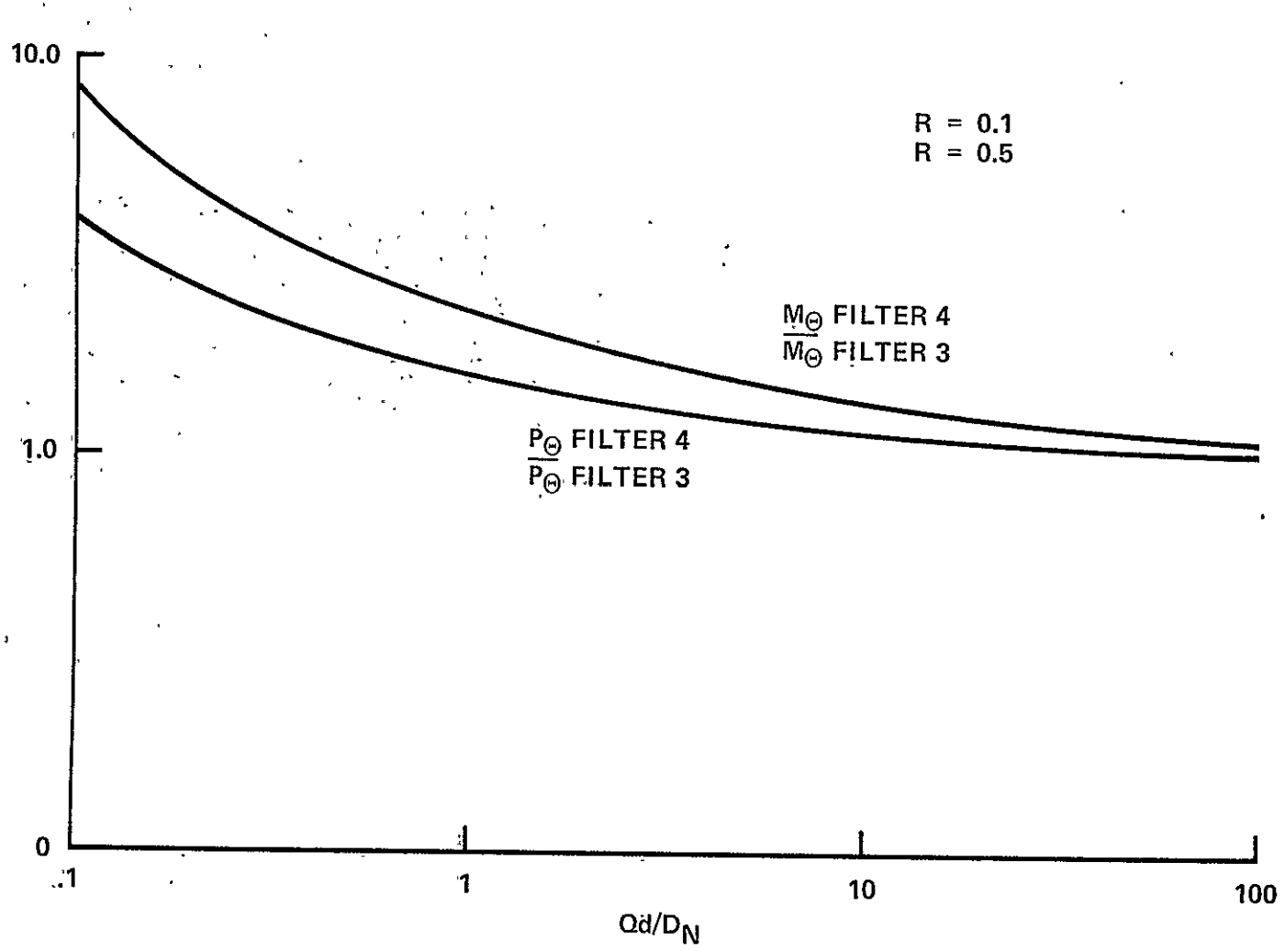

Figure 28.- Filter 4 (θ,D,θ_s) comparison to filter 3 (θ,θ_s).

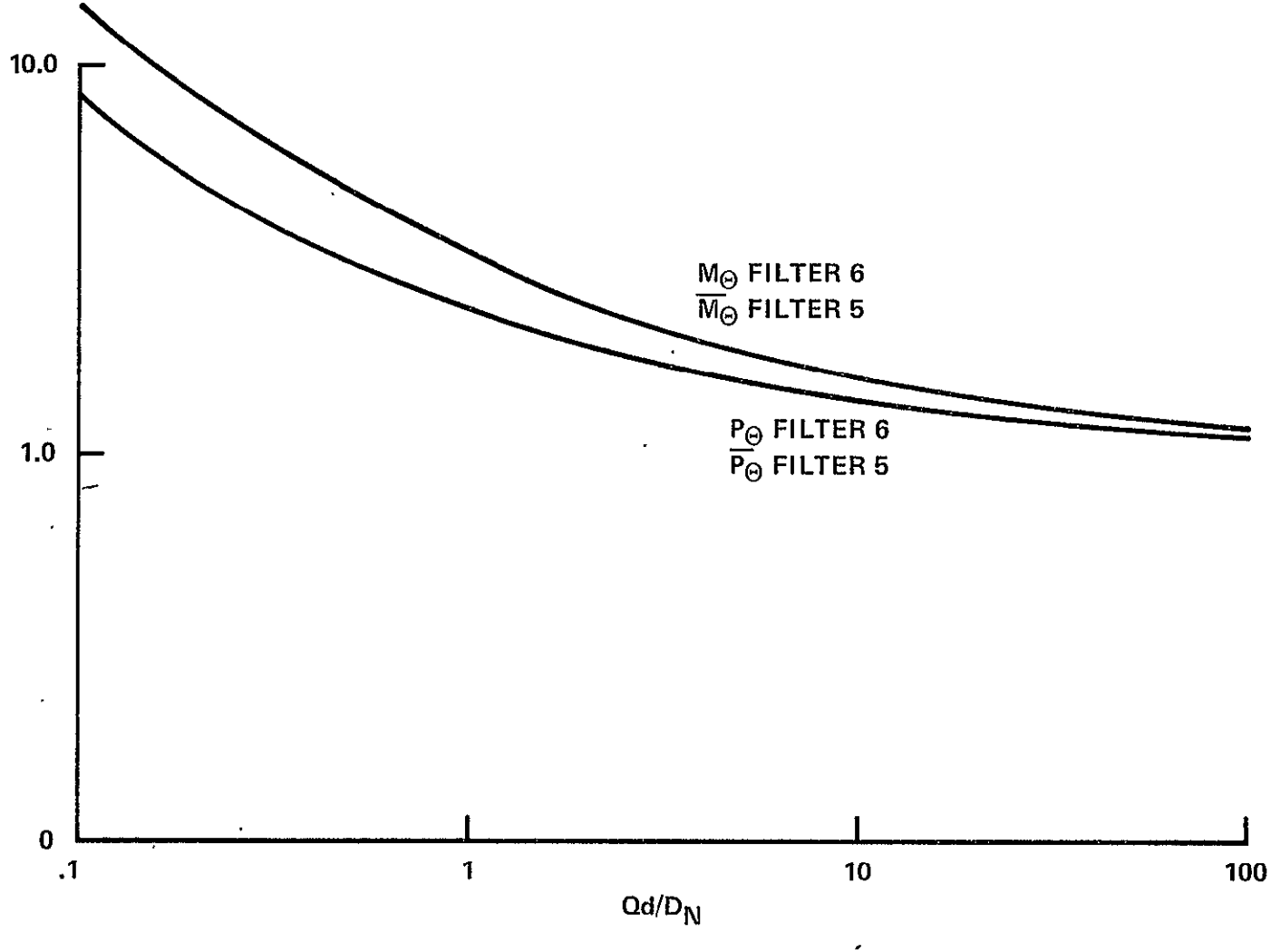

Figure 29.- Filter 6 $(\theta,D,\theta_{s1},\theta_{s2})$ comparison to filter 5 $(\theta,\theta_{s1},\theta_{s2})$.

dynamic response of the filter because the drift estimate pole appears in the transfer function for $\hat{\theta}$. This problem can be eliminated, however, by proper selection of the drift estimate gain. The comparison of filters 1 and 2 indicated that the drift estimate gain and associated pole location depend primarily on Q_d/D_N, while the gain and pole location for the attitude estimate depends primarily on Q_d/R. The implication is that the drift estimate gain can be selected for a reasonable pole location independent of the selection of pole location of the attitude estimate. This will provide good dynamic response of the filter but there will be some increase in M_θ and P_θ for the attitude estimate; this can be seen by comparing the results in Appendix A for filters 1 and 2.

The analysis of filter 1 suggested that $0.1 < Q_d/R < 10$ for good filter dynamic and noise performance. The analysis for the filters that include time delays showed that the ratio of P_θ with time delays to P_θ for filter 1 increased rapidly with Q_d/R. Because P_θ is relatively more important than M_θ, a further reduction in the acceptable range of Q_d/R (fig. 30) where $0.1 < Q_d/R < 1$, is suggested.

H. Simulation and Results

In order to verify the approach taken to the filter design and the results of the DISC analysis, a simulation of a typical gyro stabilized gimbal was developed for use on an IBM 360 digital computer. This simulation uses a simulation language, continuous system modeling program (CSMP) [9], and models one of the gyro stabilized gimbals of the AIROscope balloon gondola used by Ames Research Center [2]. Several of the filters analyzed by DISC were modeled, and various tests with sensor noise, torque disturbance, gyro drift and joystick commands were made to evaluate the system performance.

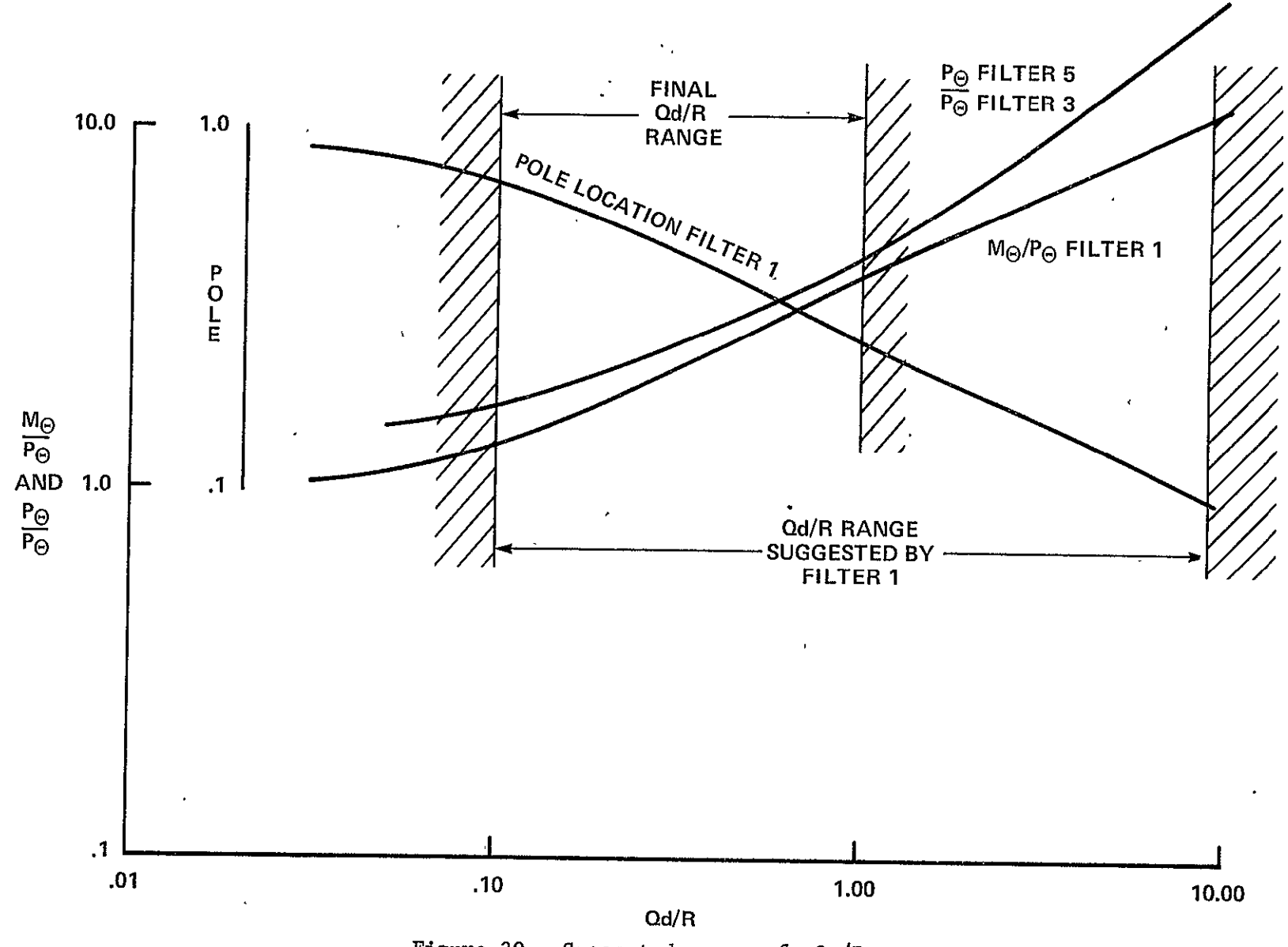

Figure 30.- Suggested range of Q_d/R.

Figure 31 is a schematic block diagram of the simulation. The basic gyro stabilization is simulated in detail including:

1. Gyro dynamics
2. Gyro demodulator and prefilter
3. Gyro stabilization compensation
4. Torque motor with back EMF
5. Saturation levels for: gyro; gyro demodulator and preamp; compensation amplifier; power amplifier; and torque motor

The video sensor integration and interpolation are simulated by an integration and averaging process where

$$\theta_I(t_{i+1}) = \int_{t_i}^{t_{i+1}} \theta \, dt \tag{58}$$

and the video sensor output is

$$v_{so} = \frac{\theta_I(t_{i+1}) - \theta_I(t_i)}{T_{VSI}} \tag{59}$$

and $T_{VSI} \triangleq$ video sensor integration time.

The time delay associated with the interpolation is not simulated nor is the multi-star processing done in the VIP microprocessor. The multi-star processing time delay is simulated as one complete cycle of the VIP microprocessor. The asynchronous operation of the video sensor and VIP microprocessor is simulated. Appendix B contains a computer listing of the complete simulation with filter 4 (θ,D,θ_s), and values for the simulation constants.

From the discussion of the continuous filter, it was concluded that the filter could be designed separately from the gyro stabilization. If the discrete filter properly models the processing time delays, response to disturbance torques is determined by the gyro stabilization dynamics,

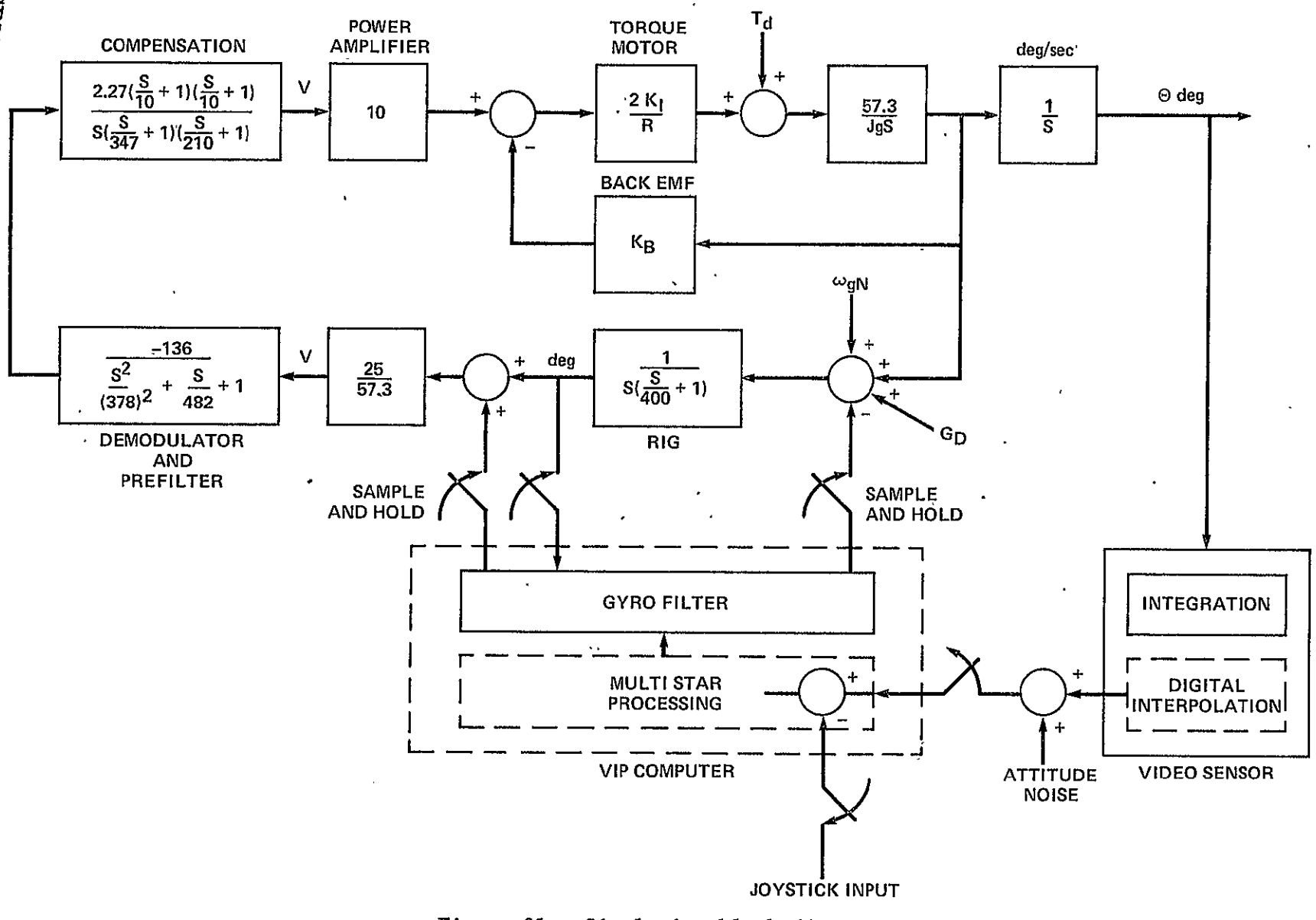

Figure 31.- Simulation block diagram.

and system noise response (θ) depends primarily on the filter noise performance. System response (θ) to joystick commands depend on both the filter and gyro dynamics.

Figure 32 shows the response of the basic gyro stabilization without video sensor feedback or the gyro filter to a step disturbance torque. Figures 33-35 show the response of the complete system to a step disturbance torque for filters with zero time delay and for those with one- and two-unit time delays, and with the video sensor integration time set at 0.25 sec and the VIP microprocessor cycle time set at 0.4 sec. The responses consist of the basic gyro stabilization dynamics in between the filter updates every 0.4 sec. The response with filter 3 (θ,θ_s), which models one-unit delay, is rapid and most completely approximates the disturbance response of the gyro stabilization. This result was expected since one-unit delay most closely represents the actual delay.

Figures 36-38 show the response to a step-disturbance torque with the video sensor integration time set at 0.9 sec and the VIP microprocessor cycle time set at 0.4 sec. The response with filter 5 ($\theta,\theta_{s1},\theta_{s2}$), which includes two-unit delays, is best, and the two-unit delays most closely represent the actual time delay. In this case, T_{VSI} = 0.9 sec and T_{VIP} = 0.4 sec, the response with filter 1 (θ) has a long term instability. Table 9 summarizes the disturbance torque

TABLE 9. TIME REQUIRED TO SETTLE WITHIN ±0.1 ARC SEC FOR T_Q = 0.1 FT LB (FILTER GAINS = 0.62)

System	T_{VSI} = 0.25 sec T_{VIP} = 0.4 sec	T_{VSI} = 0.9 sec T_{VIP} = 0.4 sec
Filter 1 (θ)	4.4 sec	Long term instability
Filter 3 (θ,θ_s)	2.0 sec	11.4 sec
Filter 5 ($\theta,\theta_{s1},\theta_{s2}$)	16.5 sec	2.3 sec

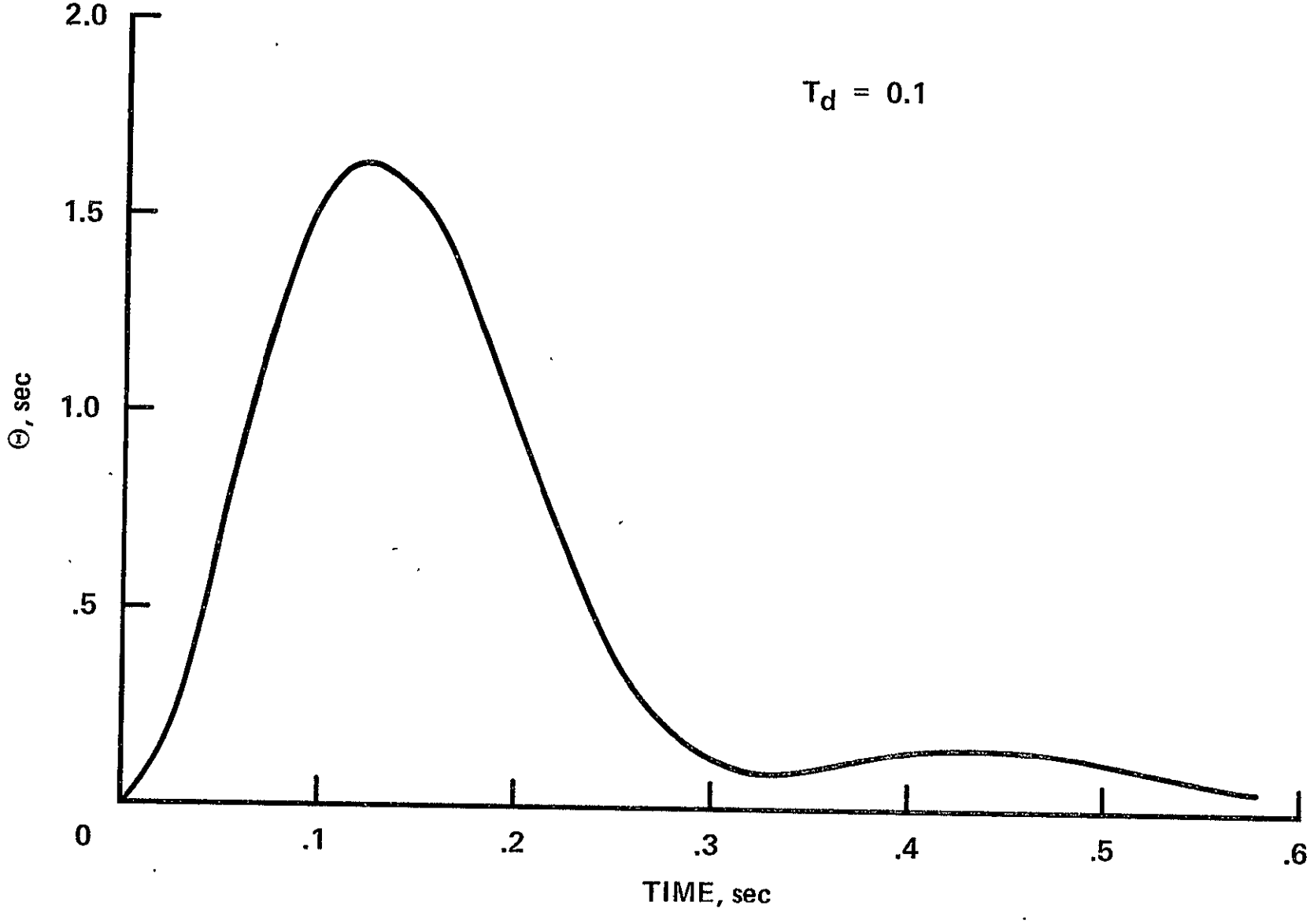

Figure 32.- Gyro stabilization T_d response.

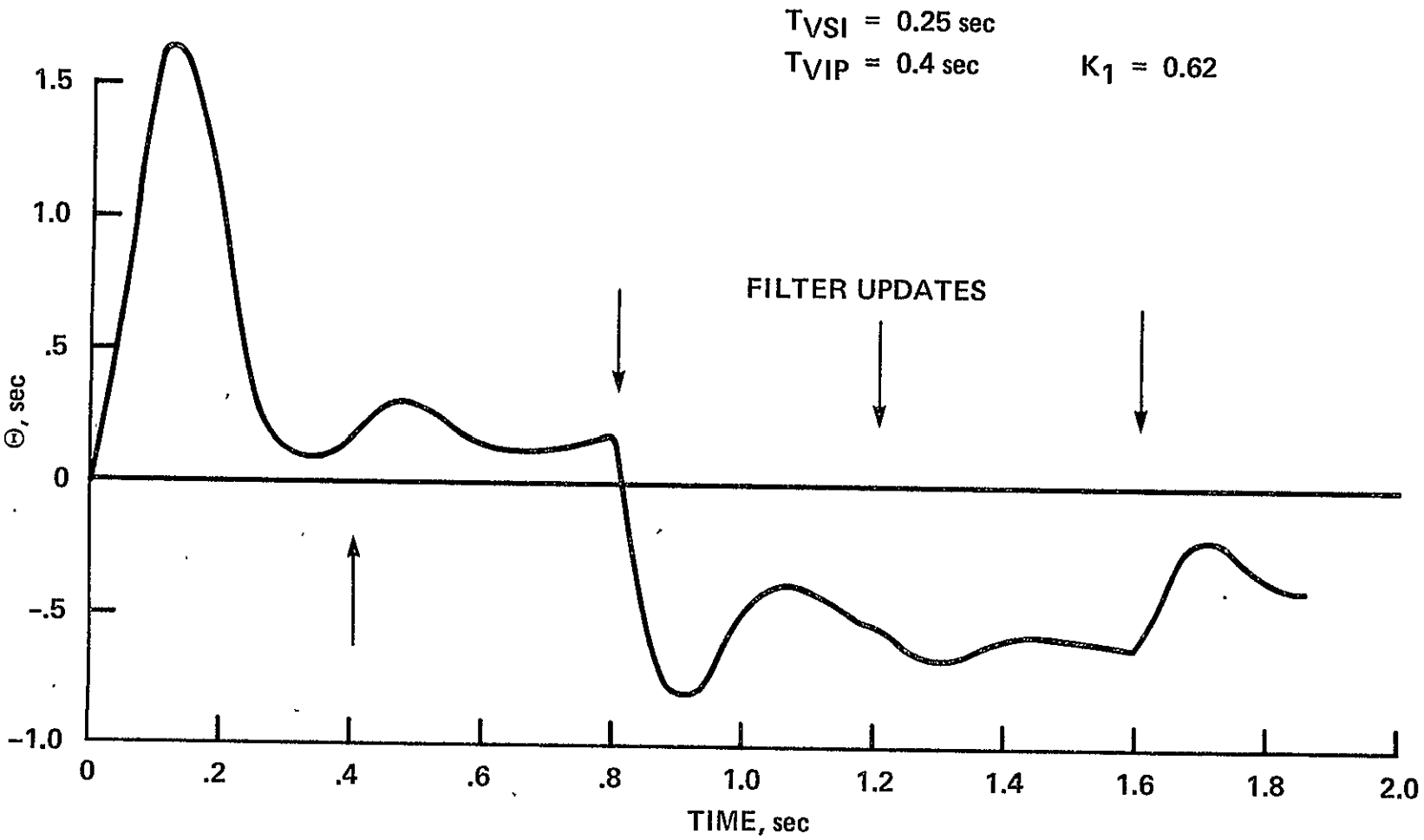

Figure 33.- Filter 1 (θ) T_d response.

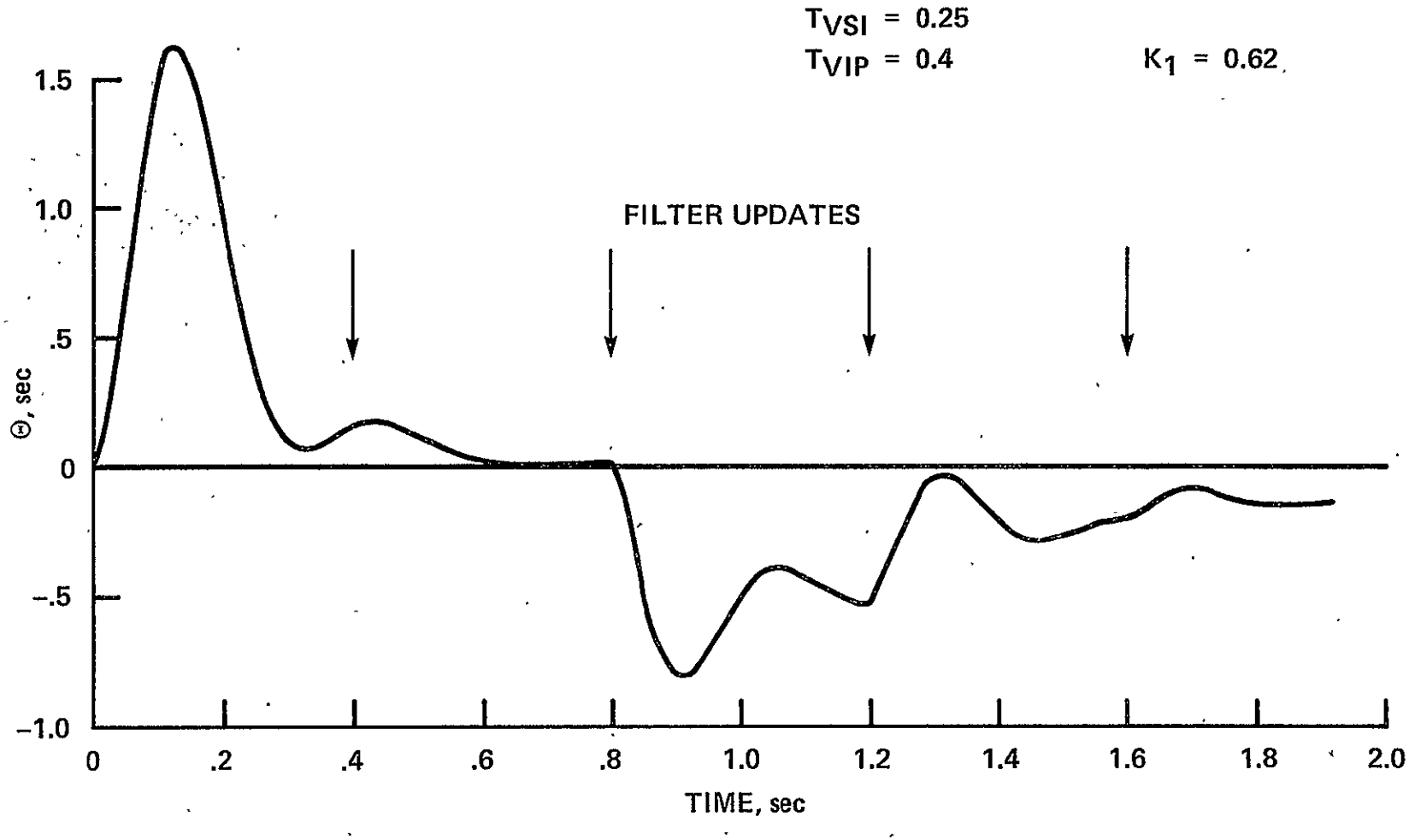

Figure 34.- Filter 3 (θ,θ_s) T_d response.

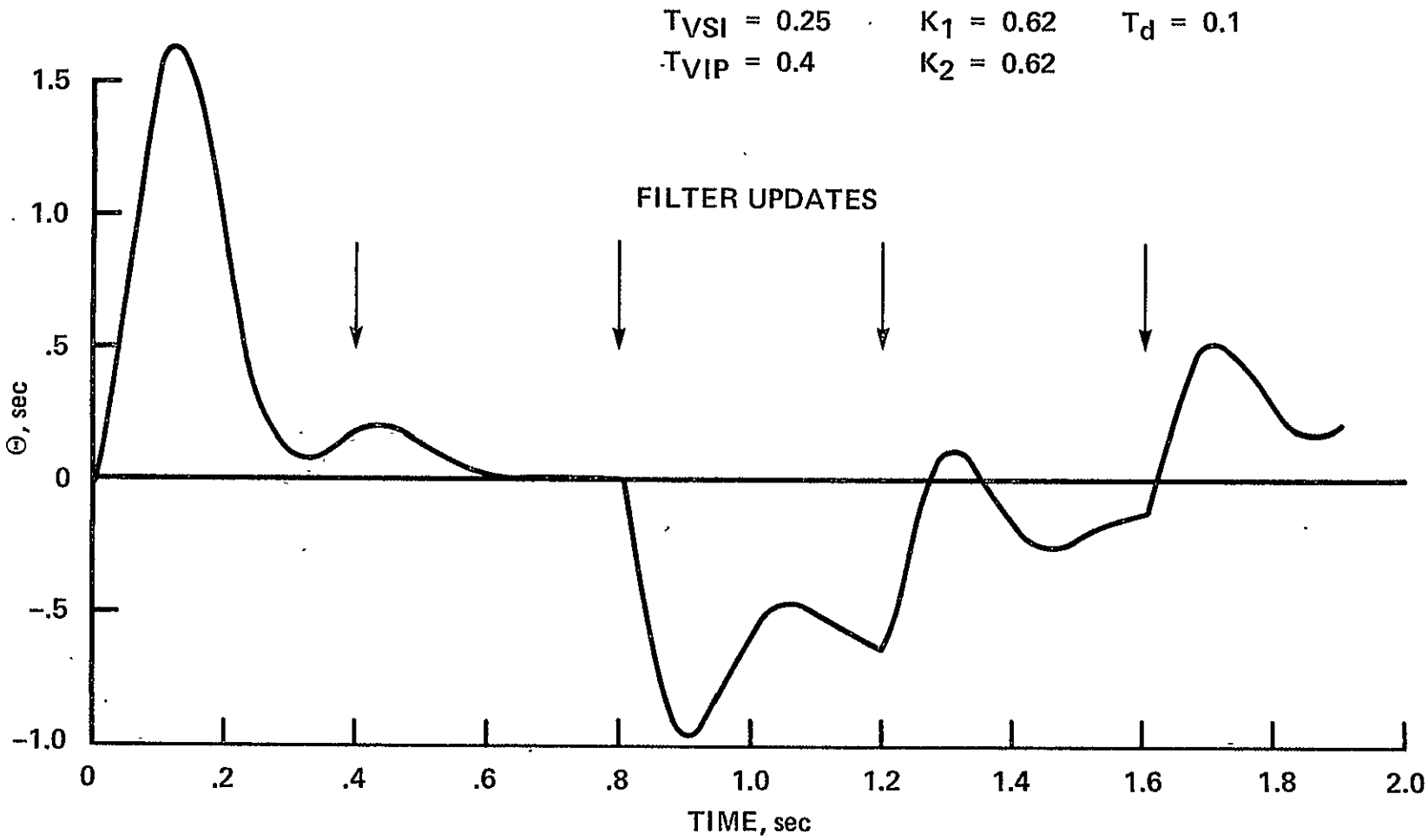

Figure 35.- Filter 5 (θ,θ_{s1},θ_{s2}) T_d response.

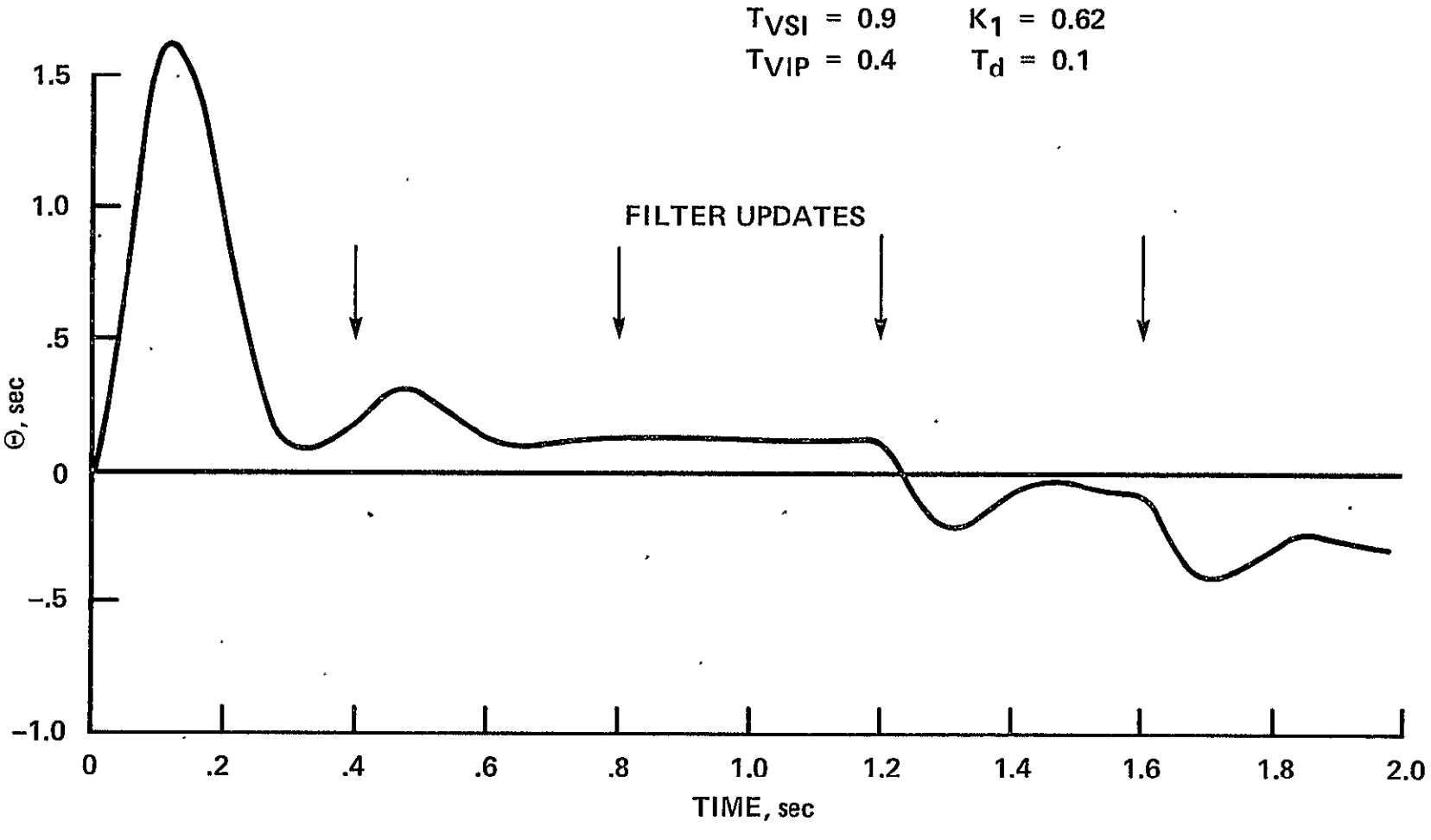

Figure 36.- Filter 1 (θ) T_d response.

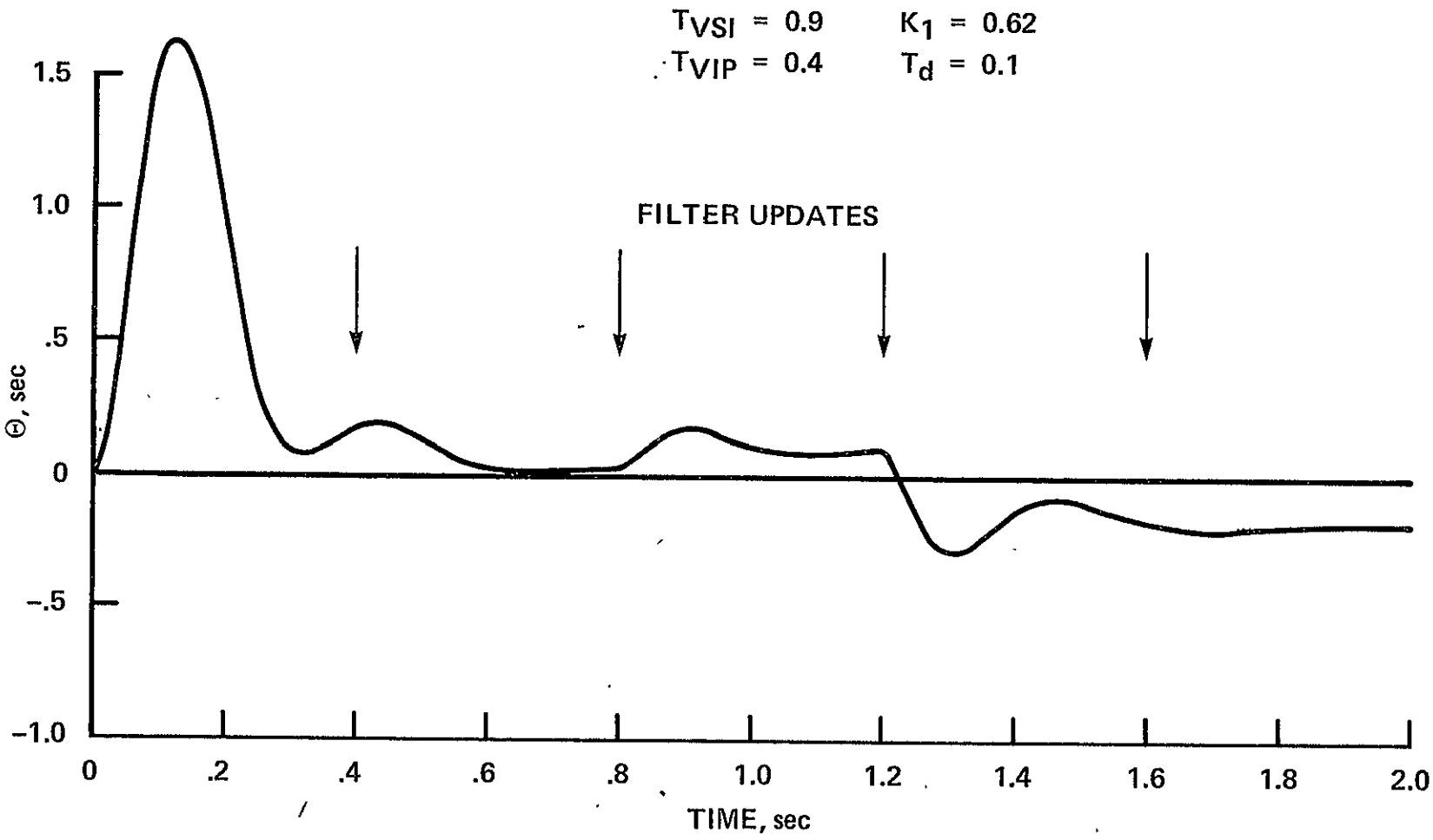

Figure 37.- Filter 3 (θ,θ_s) T_d response.

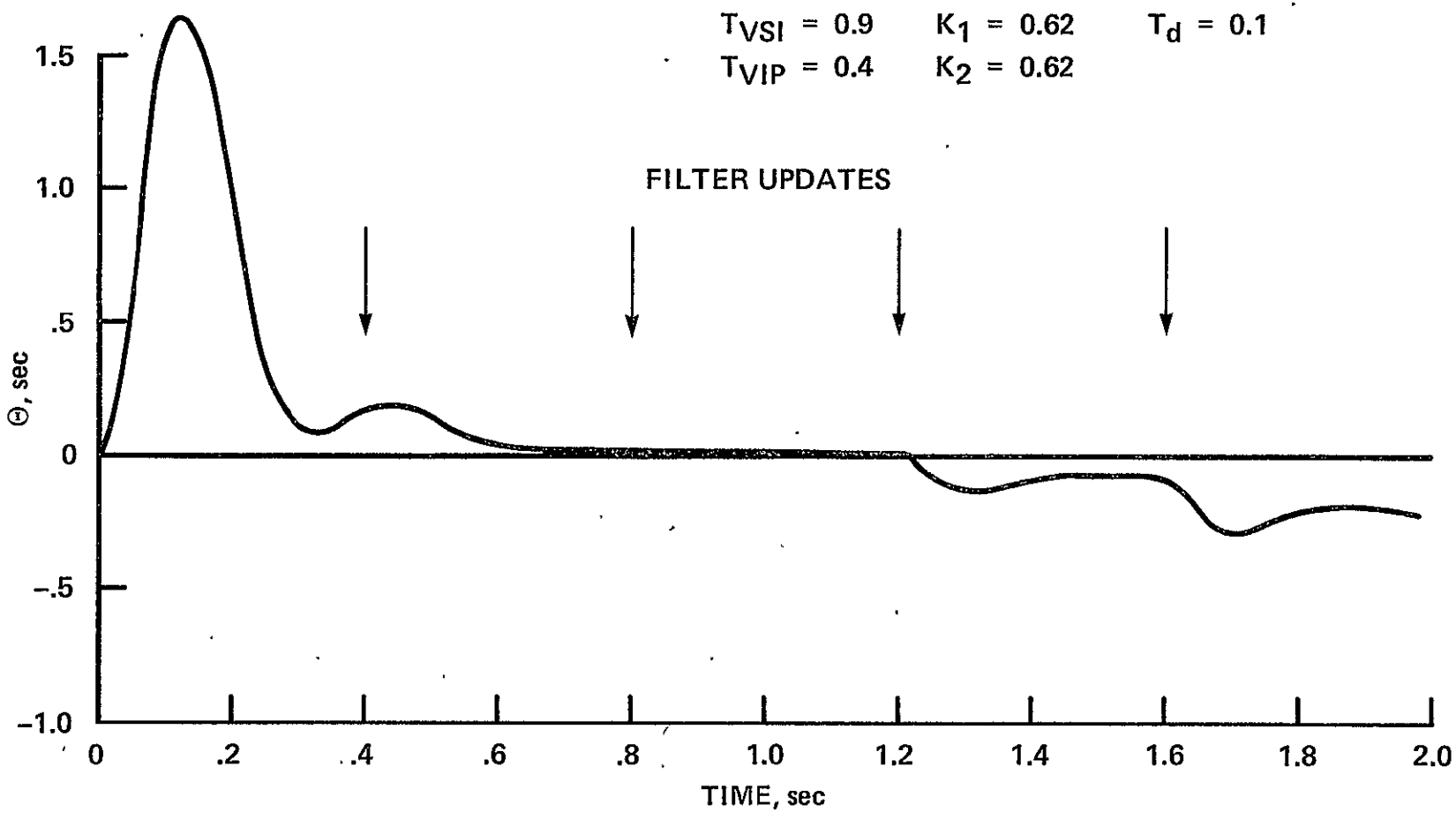

Figure 38.- Filter 5 (θ,θ_s) T_d response.

responses for the three filters and two video sensor integration times. The responses (filter 3 for T_{VSI} = 0.25 sec, and filter 5 for T_{VSI} = 0.9 sec) are somewhat longer than the basic gyro stabilization response since we have chosen to model the variable time delays (asynchronous operation of the video sensor and VIP microprocessor) as unit delays in the filters. The responses are adequate, however, and verify the basic approach.

For the joystick response, figures 39-41 show the system response to a 36 arc sec joystick command with T_{VSI} = 0.25 sec and T_{VIP} = 0.4 sec. As expected, filter 3 (θ,θ_s), which models one-unit delay, provides the best response. Figures 42-44 show similar responses for T_{VSI} = 0.9 sec and for this case, filter 5 ($\theta,\theta_{s1},\theta_{s2}$) provides the best response. Table 10 summarizes the responses to the joystick commands. The results verify the choice of filter from the disturbance response for the two different video sensor integration times.

For the system noise response, filter 3 (θ,θ_s) was used with T_{VSI} = 0.25 sec and T_{VIP} = 0.4 sec. Attitude noise is added to the output of the simulated video sensor, as shown in the simulation block diagram, figure 31, and gyro rate noise is added to the input to the rate integrating gyro. To properly simulate the values of gyro rate

TABLE 10. TIME REQUIRED TO SETTLE TO 36 ±1 ARC SEC JOYSTICK STEP AT T = 0 (FILTER GAINS = 0.62)

Filter	T_{VSI} = 0.25 sec T_{VIP} = 0.4 sec	T_{VSI} = 0.9 sec T_{VIP} = 0.4 sec
1 (θ)	6.3 sec	Unstable
3 (θ,θ_s)	1.6 sec	>20 sec
5 ($\theta,\theta_{s1},\theta_{s2}$)	18.2 sec	5.8 sec

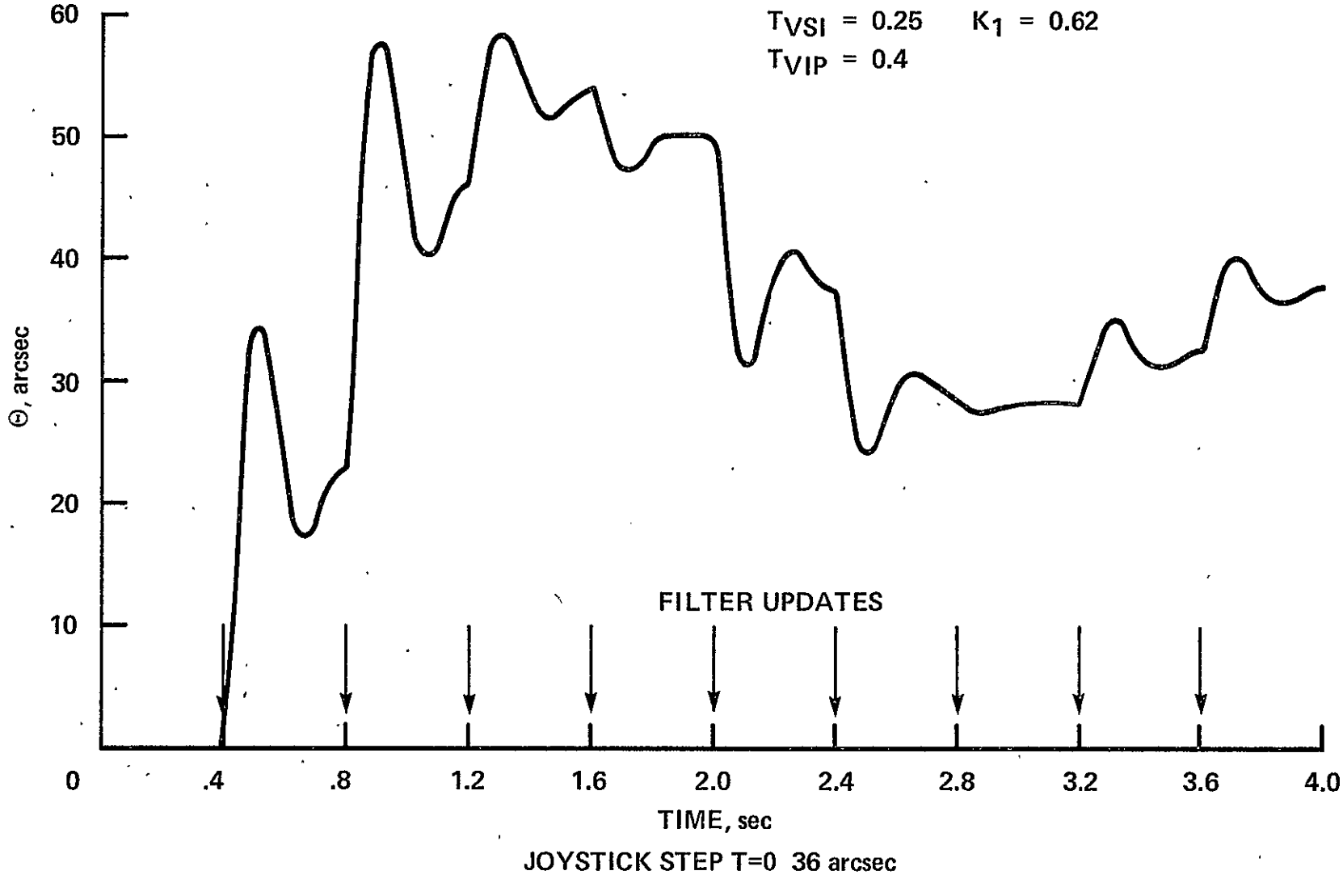

Figure 39.- Filter 1 (θ) joystick response.

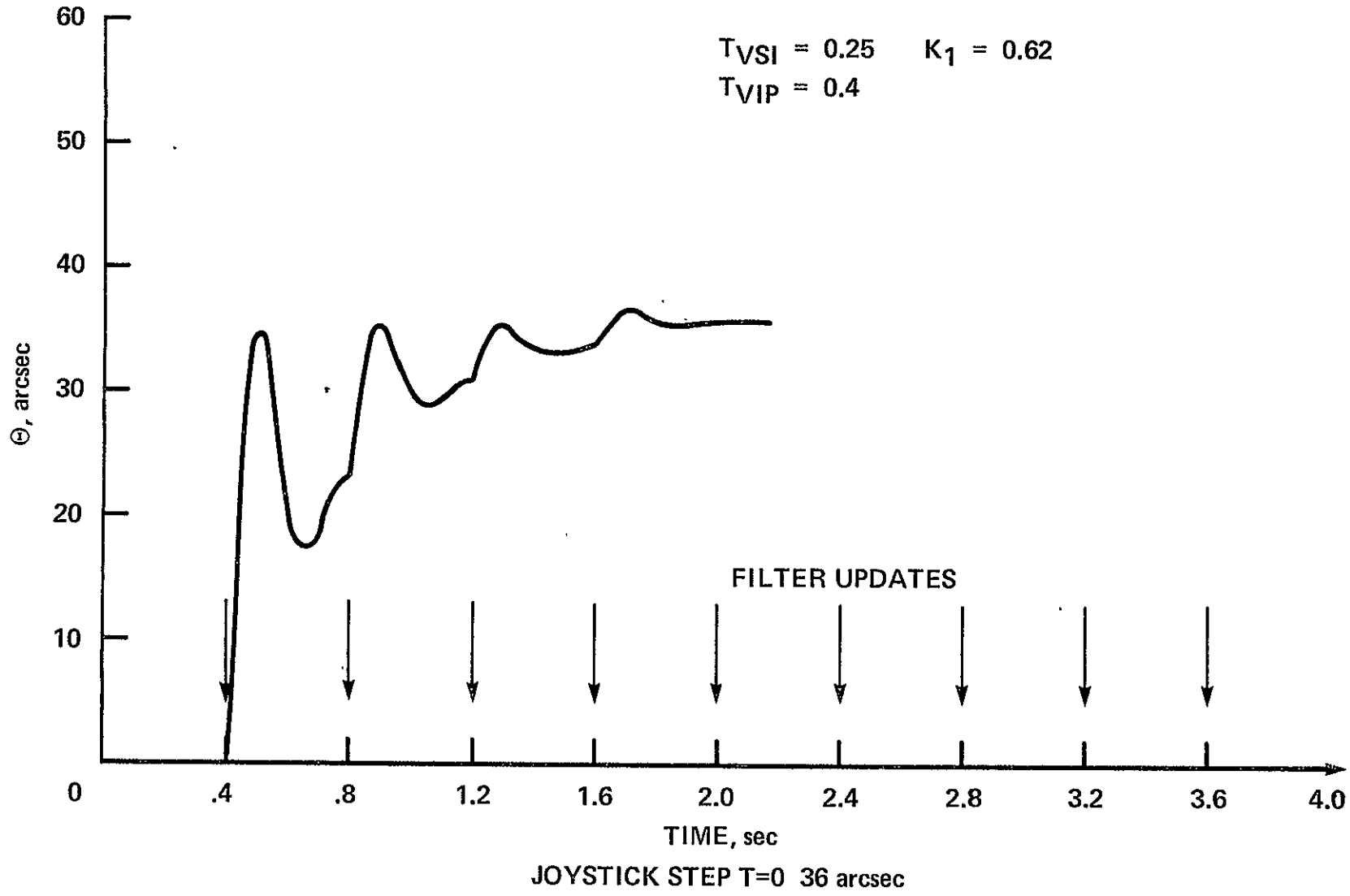

Figure 40.- Filter 3 (θ,θ_s) joystick response.

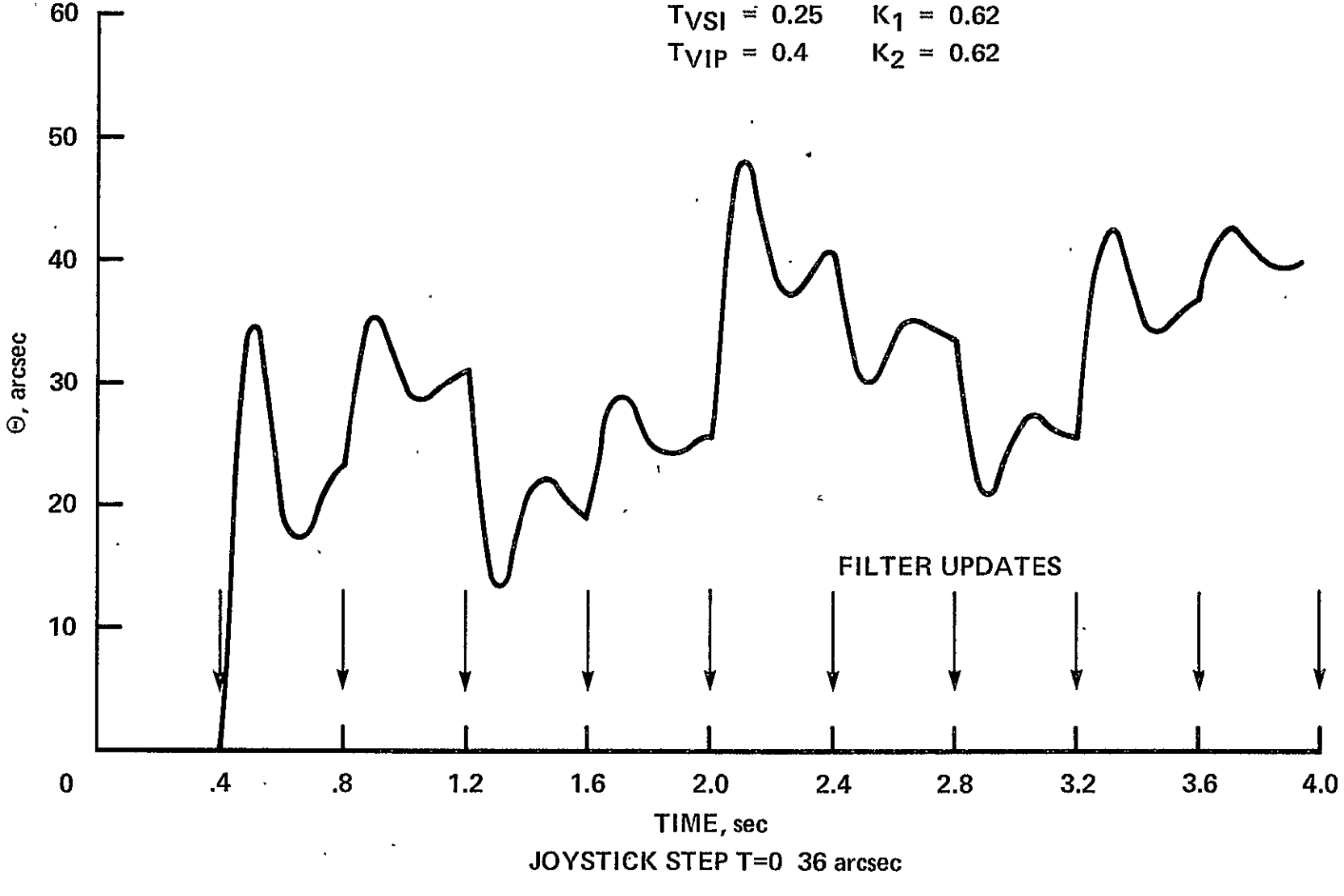

Figure 41.- Filter 5 ($\theta,\theta_{s1},\theta_{s2}$) joystick response.

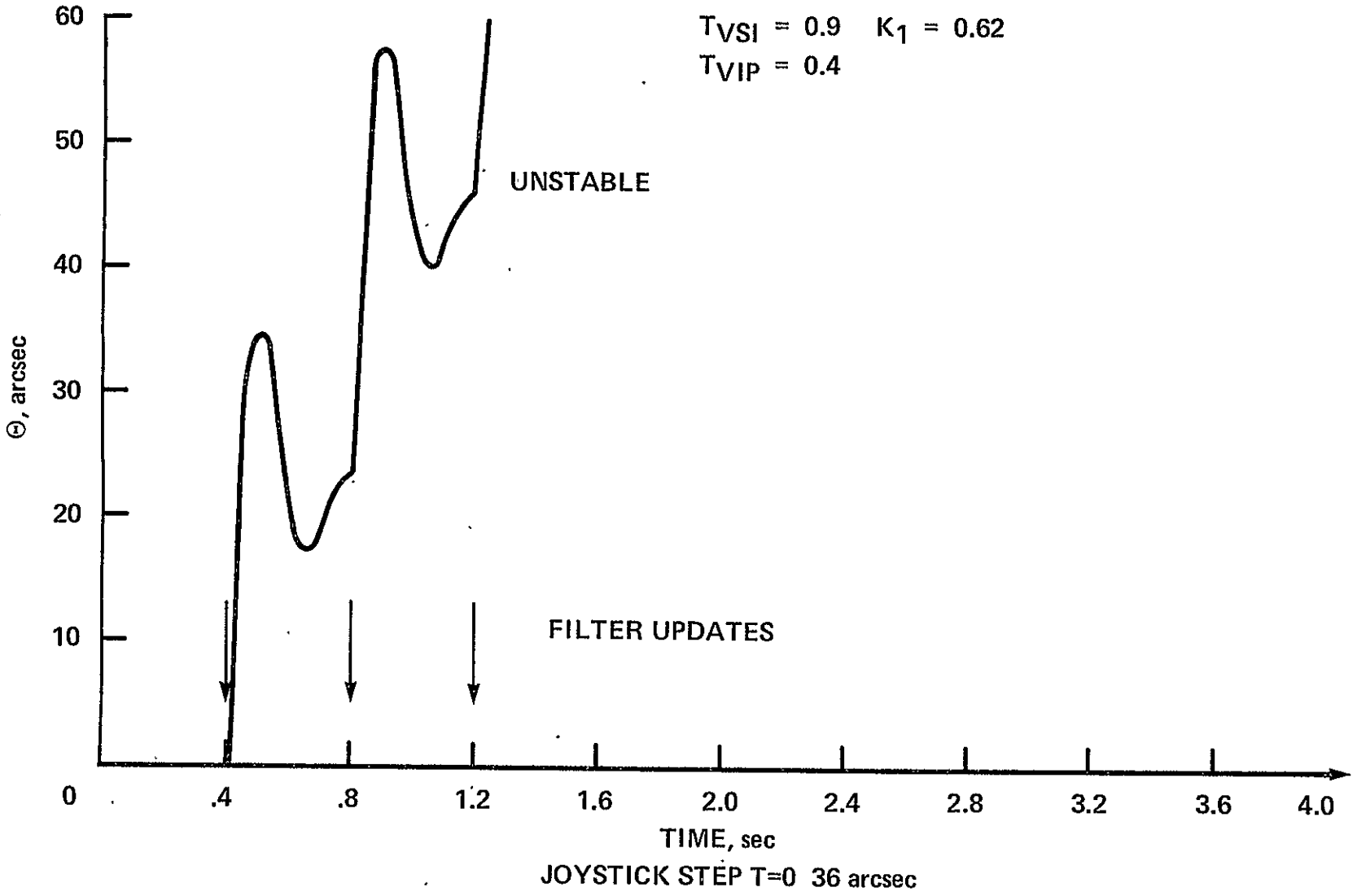

Figure 42.- Filter 1 (θ) joystick response.

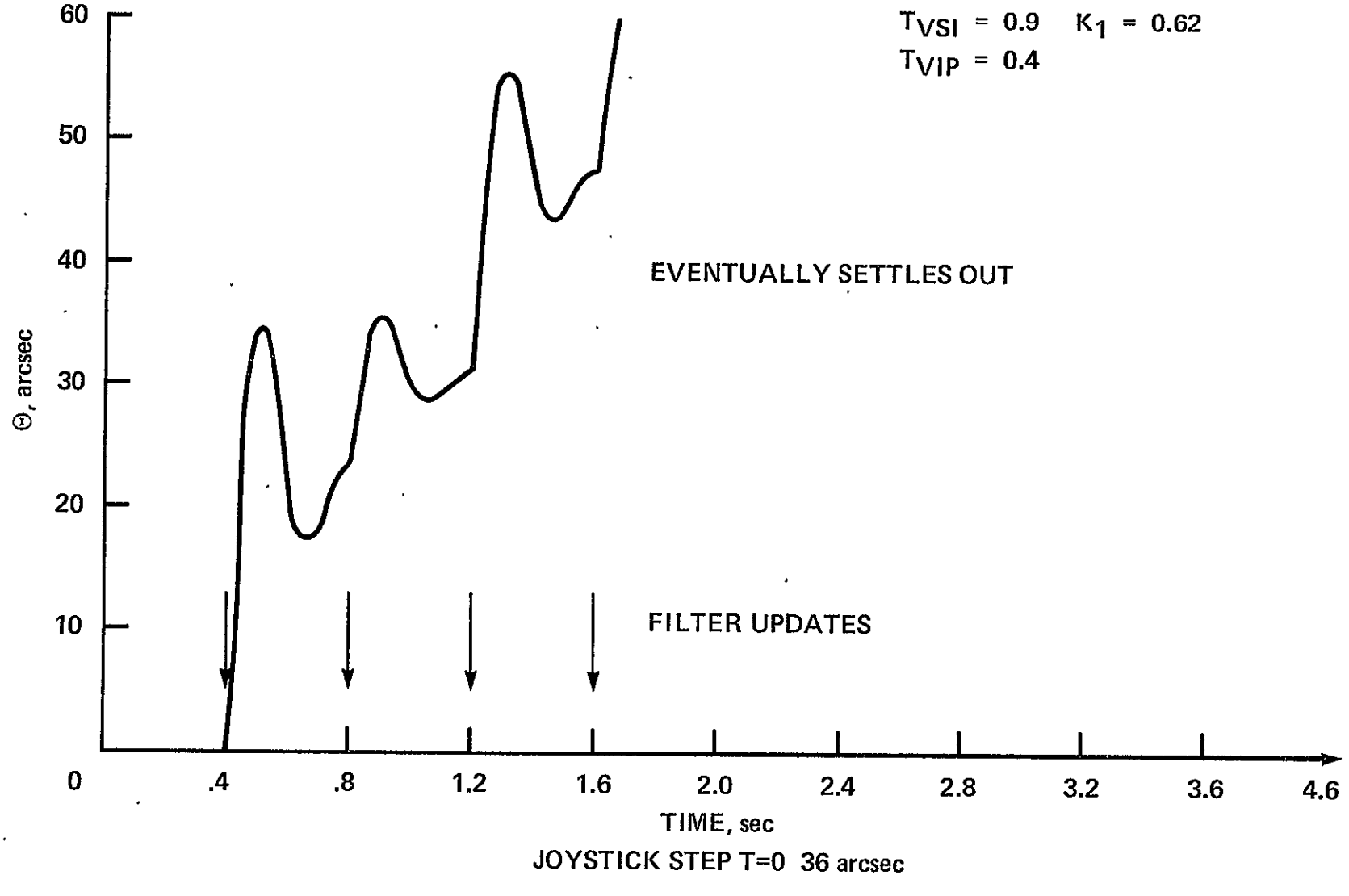

Figure 43.- Filter 3 (θ,θ_s) joystick response.

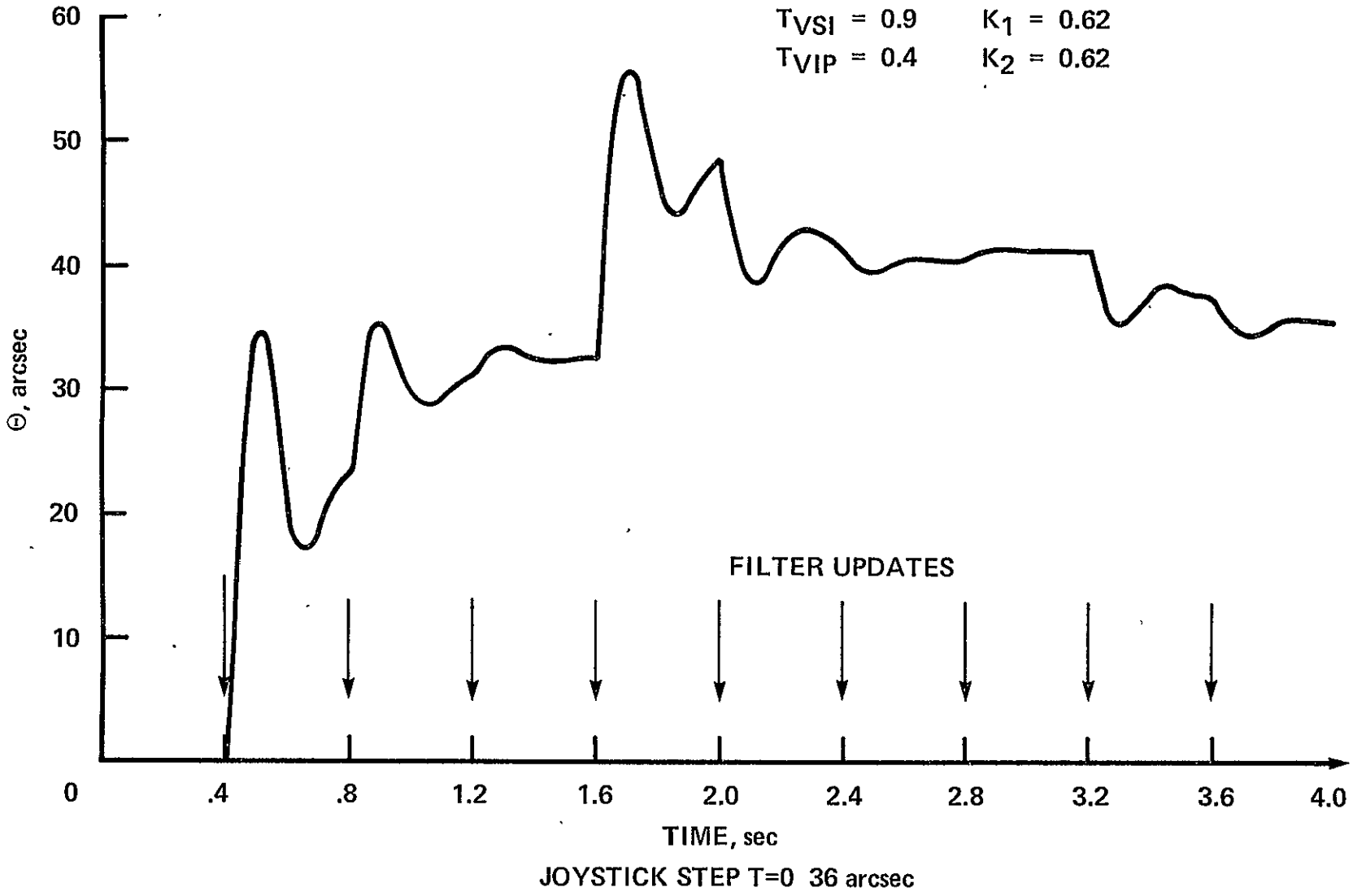

Figure 44.- Filter 5 (θ,θ_{s1},θ_{s2}) joystick response.

noise (Q_d) used in the DISC analysis, it was necessary to consider the integration time of the digital simulation [10] and $\chi(k) = Q_d/\Delta t$. Since $\Delta t = 0.005$ sec, the standard deviation of the gyro rate noise used in the simulation is 14.1 times the standard deviation of the gyro noise used in the DISC analysis. In table 11, the noise performance predicted by DISC and the actual simulation noise performance are compared. The standard deviation of θ was computed from the simulation results using a large number of data points at equally spaced time intervals and represents an approximation. Nevertheless the simulation results agree quite closely with the DISC analysis verifying the conclusion that the filter noise performance determines the overall system noise performance.

In order to verify the basic approach taken to the filter design with the simulation, the drift term was not included in the filter models. To evaluate system performance with the drift estimator, filter 4 (θ,D,θ_s) is used with $T_{VSI} = 0.25$ sec and $T_{VIP} = 0.4$ sec. The system response to a drift step with drift estimator gains of -0.55 and -0.10 is compared in table 12. The lower gain on the drift estimate results in slower filter dynamics in agreement with the DISC analysis, and the gain of -0.55 is used for the joystick command and disturbance torque responses to provide adequate dynamic response. Figure 45 shows the system response to a disturbance torque response and figure 46 shows the system response to a joystick command using filter 4 (θ,D,θ_s) with the drift estimator gain of -0.55. These responses compare directly to figures 34 and 40, and in both cases the response time is significantly longer due to the effect of the drift estimator on the filter poles.

Noise response with filter 4 (θ,D,θ_s) is shown in table 13, and compares well with the values given in table 12 (no drift estimator) for

TABLE 11. NOISE RESPONSE: FILTER 3 (θ,θ_s);
T_{VSI} = 0.25 SEC, T_{VIP} = 0.4 SEC

Q_d	R	$\sqrt{M_\theta}$	$\sqrt{P_\theta}$	K	θ simulation standard deviation
1	1	1.6	1.3	0.62	1.3
10	1	4.6	3.3	0.92	3.1
1	10	2.7	1.9	0.27	1.8
100	1	14.1	10.0	0.99	8.1
1	100	3.4	3.2	0.1	2.2

TABLE 12. RESPONSE TO DRIFT STEP: FILTER 4 (θ,D,θ_s);
T_{VSI} = 0.25 SEC, T_{VIP} = 0.4 SEC; K_1 = 0.62

Drift gain	Time to reach steady state ±10%
-0.55	6.8 sec
-0.1	12.8 sec

TABLE 13. NOISE RESPONSE: FILTER 4 (θ,D,θ_s);
T_{VSI} = 0.25 SEC, T_{VIP} = 0.4 SEC

Q_d	R	K_1	K_2	θ simulation standard deviation
1	1	0.62	-0.55	1.8
10	1	0.92	-0.55	3.4
1	10	0.27	-0.55	8.3
1	100	0.1	-0.55	60.5

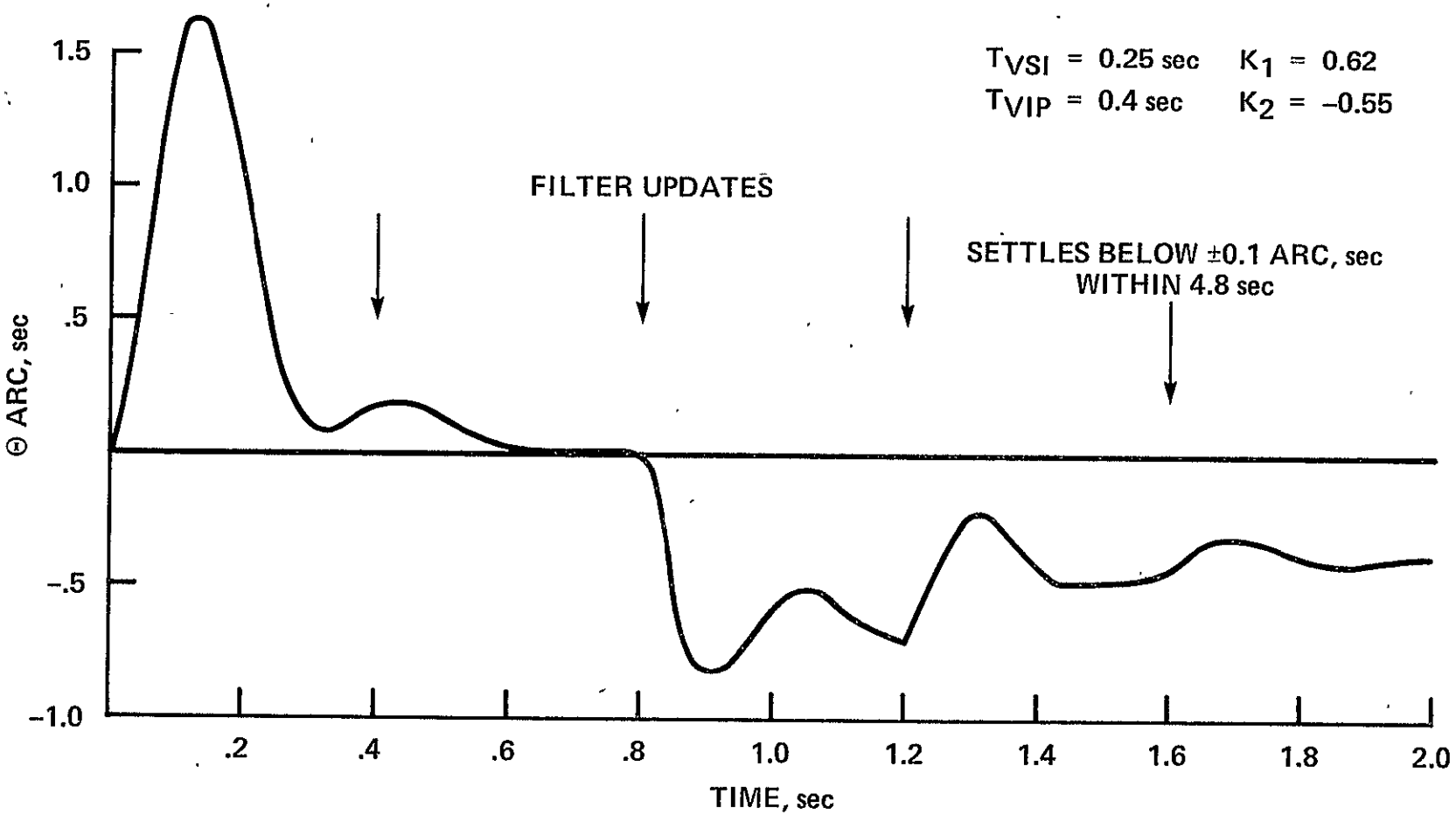

Figure 45.- Filter 4 (θ,D,θ_s) T_d response.

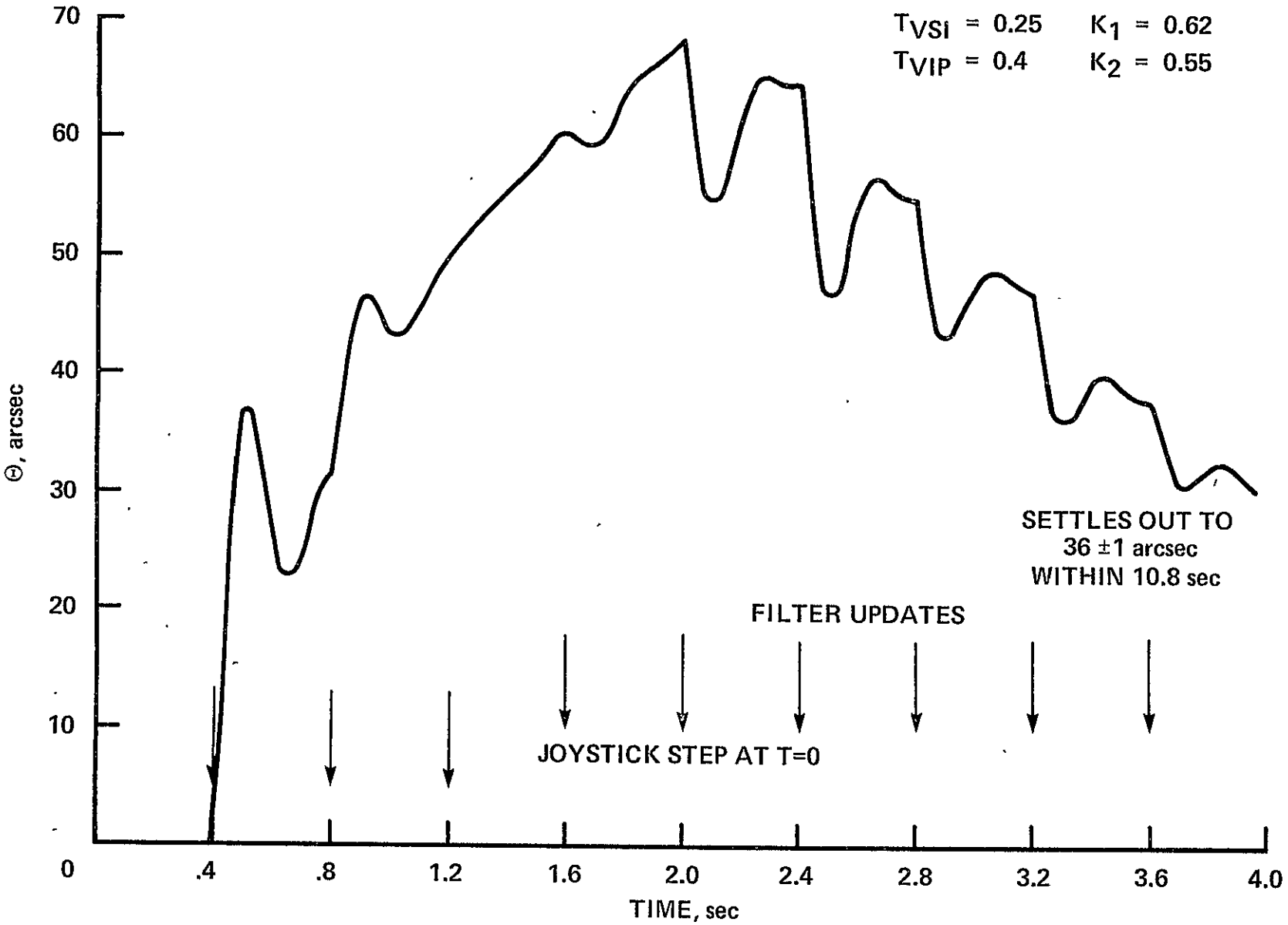

Figure 46.- Filter 4 (θ,D,θ_s) joystick response.

$Q_d = 1$, $R = 1$, and $Q_d = 10$, $R = 1$. For the larger values of R/Q_d, the noise response is much worse than the values in table 11. Since inclusion of the drift estimator in the filter causes longer responses to disturbance torques and to joystick commands, and poorer noise performance, it may be desirable to use filters without the drift estimator during periods when low noise performance or rapid slewing with joystick commands is desired.

I. Summary

The approach taken to the gyro filtering design has been validated by the simulation. A discrete, steady-state Kalman filter is developed that uses the rate integrating gyro. Assumption of asynchronous operation of the video sensor and VIP microprocessor lead to the use of unit time delays in the filter modeling the actual variable delay. DISC has been used to analyze the six filter models, and the DISC data can be used for two approaches to the overall system design.

1. Select filter gains and estimate system performance given levels of sensor noise.

2. Select sensor noise levels and, therefore, sensor quality and cost based on desired system performance.

Once the sensor noise levels and system performance have been determined, the gyro filtering technique can be summarized as follows:

1. Select filter gains from the DISC analysis based on noise and dynamic performance of desired system.

2. Store filter models (as given in fig. 13 and figs. 17-21) and gains in the VIP microprocessor memory.

3. Implement filter model selection algorithm in the VIP microprocessor based on the video sensor integration time control setting.

An additional consideration to the filter model selection is the inclusion of the drift estimator. As noted in the simulation results, the drift estimator causes poor disturbance torque response and slower response to joystick commands. It may be desirable to include the drift estimator only when joystick commands, or low-noise pointing, are not required. The drift estimate could then be stored and used as a gyro input, but it would not be continuously updated at each computer cycle.

CHAPTER V. CONCLUSIONS

Multi-star processing and gyro filtering techniques for the advanced VIP system have been developed and evaluated. The multi-star processing technique uses linearized, small-angle equations consistent with the limitations of the VIP microprocessor. A minimum of two guide stars (guide star pair) are required to uniquely determine the three-axis pointing error signals. Guide star pairs and pointing error equations must be selected based on the multi-star processing equation's singularities. When more than one guide star pair is available, the three-axis pointing error signal from each pair can be averaged to reduce the noise and steady-states errors in the pointing error signals. Consideration must be given to the number of guide star pairs used, since computation time increases proportionally to N, and the reduction in errors is proportional to the $\sqrt{N}$. As noted in the gyro filtering analysis; time delays must be included in the filter model, and the noise performance (θ) of the filter decreases with increased time delay. A further consideration for the multi-star processing is the sensitivity of the roll-pointing error signals as the guide stars get closer to the desired pointing direction. An analysis is presented that allows roll guide star selection based on desired roll-pointing error performance.

The approach taken to the gyro filtering development is the use of a discrete, steady-state Kalman filter. A unique feature is the use of the integration provided by the gyro stabilization's RIG as an integral part of the filter. Considerations are developed with a continuous filter to show how the filter can be designed and evaluated separately from the basic gyro stabilization. Time delays associated with the multi-star processing and video sensor operation are modeled in the filter as

unit delays of the VIP microprocessor based on the assumption of asynchronous operation. Six filter models and their hardware implementations are developed. Various combinations of attitude (θ), drift, and unit time delays are modeled. The DISC analysis can be used for selection of filter gains based on system performance requirements. An alternate use of the DISC analysis is the selection of sensor noise levels necessary to achieve a desired system performance; however, the DISC analysis strongly suggests an acceptable range of Q_d/R in order to obtain a reasonable compromise between filter noise performance (θ) and dynamics.

A digital simulation of a typical gyro stabilized gimbal is developed and is used to validate the approach taken to the gyro filtering. Disturbance torque and joystick command responses are evaluated with two video sensor integration times and zero-, one-, or two-unit time delays included in the filters. The results confirm the use of the unit time delays and provide a comparative means of selecting the filter to use with a selected sensor integration time. A filter model with a drift estimate is included in the simulation, and degraded noise performance and dynamic response result, consistent with the DISC analysis. It is concluded that the drift estimator should not be included when precise joystick maneuvers or low noise pointing are required.

Specific contributions of this work include:

1. Development of unique multi-star processing equations which can be used to obtain three-axis pointing error signals from a guide star pair.

2. Development of selection criteria for equations and guide star pairs and for the multi-star processing that are based on equation singularities and resulting error performance.

3. Development of a unique, discrete Kalman filter that uses the stabilization gyros integration.

4. Development of a design approach to the gyro filtering that separates the design aspects of the Kalman filter and the gyro stabilization.

5. Development of a practical approach to the inclusion of unit time delays in the Kalman filter.

While the prime objectives of this work have been accomplished, there are several areas where further effort could prove useful:

1. Development and evaluation of a technique that would allow the measurement and use of the actual time delays in the filter equations at each update.

2. Consideration of synchronous operation of the VIP microprocessor and the video sensor, and an analysis of the resulting performance tradeoffs.

3. Consideration of a more complex method of slewing with the joystick during automatic pointing. For instance, it may be possible to introduce slewing commands without exciting the filter dynamics by placing a simultaneous joystick command into the filter and at the gyro output into the gyro stabilization.

APPENDIX A

DISC DATA FOR FILTERS 1-6

FILTER 1 (θ)

Q_d	R	M_θ	P_θ	K	Poles
0.1	0.1	0.16	0.06	0.62	0.38
1	0.1	1.09	0.09	0.92	0.08
10	0.1	10.10	0.10	0.99	0.01
100	0.1	100.10	0.10	1.00	0
0.1	1	0.37	0.27	0.27	0.73
1	1	1.62	0.62	0.62	0.38
10	1	10.92	0.92	0.92	0.08
100	1	100.99	0.99	0.99	0.01
0.1	10	1.05	0.95	0.09	0.90
1	10	3.70	2.70	0.27	0.73
10	10	16.18	6.18	0.62	0.38
100	10	109.2	9.2	0.92	0.08
0.1	100	3.21	3.11	0.03	0.97
1	100	10.51	9.51	0.09	0.91
10	100	37.02	27.02	0.27	0.73
100	100	161.80	61.80	0.62	0.38

FILTER 2 (θ,D): $D_N = 0.1$, $T = 0.25$

Q_d	R	M_θ	P_θ	K	Poles
0.1	0.1	0.23	0.07	0.69 -0.55	0.40 0.77
1	0.1	1.19	0.09	0.92 -0.28	0.08 0.93
10	0.1	10.36	0.10	0.99 -0.10	0.01 0.98
100	0.1	100.89	0.10	1.00 -0.03	0 0.99
0.1	1	0.66	0.40	0.40 -0.25	0.77 ± 0.09j
1	1	1.83	0.65	0.65 -0.19	0.38 0.92
10	1	11.22	0.92	0.92 -0.10	0.08 0.98
100	1	101.80	0.99	0.99 -0.03	0.01 0.99
0.1	10	2.77	2.17	0.22 -0.09	0.88 ± 0.09j
1	10	4.71	3.20	0.32 -0.08	0.74 0.92
10	10	16.83	6.27	0.63 -0.06	0.38 0.98
100	10	110.10	9.17	0.92 -0.03	0.08 0.99
0.1	100	13.84	12.16	0.12 -0.03	0.94 ± 0.06j
1	100	17.42	14.84	0.15 -0.03	0.92 ± 0.04j
10	100	40.36	28.75	0.29 -0.03	0.73 0.98
100	100	163.87	62.10	0.62 -0.02	0.38 0.99

FILTER 2 (θ,D): $D_N = 1$, $T = 0.25$

Q_d	R	M_θ	P_θ	K	Poles
0.1	0.1	0.38	0.08	0.79 -1.45	0.42 ± 0.17j
1	0.1	1.41	0.09	0.93 -0.81	0.09 0.78
10	0.1	10.93	0.10	0.99 -0.30	0.01 0.92
100	0.1	102.62	0.10	1.00 -0.10	0 0.98
0.1	1	1.17	0.54	0.54 -0.68	0.65 ± 0.21j
1	1	2.28	0.69	0.69 -0.55	0.40 0.77
10	1	11.88	0.92	0.92 -0.28	0.08 0.92
100	1	103.56	0.99	0.99 -0.10	0.01 0.98
0.1	10	5.07	3.36	0.34 -0.26	0.80 ± 0.16j
1	10	6.60	3.98	0.40 -0.25	0.77 ± 0.09j
10	10	18.25	6.46	0.65 -0.19	0.38 0.92
100	10	112.16	9.18	0.92 -0.10	0.08 0.97
0.1	100	25.34	20.22	0.20 -0.09	0.89 ± 0.1j
1	100	27.75	21.72	0.22 -0.09	0.88 ± 0.09j
10	100	47.10	32.02	0.32 -0.08	0.74 0.92
100	100	168.34	62.74	0.63 -0.06	0.38 0.98

FILTER 2 (θ,D): $D_N = 0.1$, $T = 0.5$

Q_d	R	M_θ	P_θ	K	Poles
0.1	0.1	0.30	0.08	0.75 -0.50	0.50 ± 0.05j
1	0.1	1.29	0.09	0.93 -0.27	0.08 0.85
10	0.1	10.62	0.10	0.99 -0.10	0.01 0.95
100	0.1	101.69	0.10	1.00 -0.03	0 0.98
0.1	1	0.90	0.47	0.47 -0.23	0.71 ± 0.17j
1	1	2.03	0.67	0.67 -0.18	0.39 0.85
10	1	11.52	0.92	0.92 -0.09	0.08 0.95
100	1	102.61	0.99	0.99 -0.03	0.01 0.98
0.1	10	3.93	2.82	0.28 -0.09	0.84 ± 0.13j
1	10	5.62	3.60	0.36 -0.08	0.80 ± 0.01j
10	10	17.49	6.36	0.64 -0.06	0.38 0.95
100	10	111.05	9.17	0.92 -0.03	0.08 0.98
0.1	100	19.80	16.52	0.17 -0.03	0.91 ± 0.08j
1	100	22.63	18.45	0.19 -0.03	0.90 ± 0.07j
10	100	43.55	30.34	0.30 -0.03	0.73 0.95
100	100	165.94	62.40	0.62 -0.02	0.38 0.98

FILTER 2 (θ,D): $D_N = 1$, $T = 0.5$

Q_d	R	M_θ	P_θ	K	Poles
0.1	0.1	0.63	0.09	0.86 -1.17	0.28 ± 0.25j
1	0.1	1.77	0.10	0.95 -0.73	0.10 0.60
10	0.1	11.80	0.10	0.99 -0.30	0.01 0.85
100	0.1	105.19	0.10	1.00 -0.10	0 0.95
0.1	1	1.85	0.65	0.65 -0.59	0.53 ± 0.27j
1	1	2.95	0.75	0.75 -0.50	0.50 ± 0.05j
10	1	12.88	0.93	0.93 -0.27	0.08 0.85
100	1	106.17	0.99	0.99 -0.10	0.01 0.95
0.1	10	7.70	4.35	0.435 -0.24	0.72 ± 0.21j
1	10	9.03	4.75	0.48 -0.23	0.71 ± 0.17j
10	10	20.32	6.70	0.67 -0.18	0.39 0.35
100	10	115.20	9.20	0.92 -0.09	0.08 0.95
0.1	100	37.40	27.22	0.27 -0.09	0.84 ± 0.13j
1	100	39.32	28.22	0.28 -0.08	0.84 ± 0.13j
10	100	56.18	35.97	0.36 -0.08	0.8 ± 0.01j
100	100	174.89	63.62	0.64 -0.06	0.38 0.95

FILTER 3 (θ,θ_s): $\varepsilon = 0.00001$

Q_d	R	M_θ	P_θ	K	Poles
0.1	0.1	0.26	0.16	0.62 0.62	0 0.38
1	0.1	2.09	1.09	0.916 0.916	0 0.08
10	0.1	20.10	10.10	0.99 0.95	0 0.01
100	0.1	200.10	100.10	0.99 1.44	0 0
0.1	1	0.47	0.37	0.27 0.27	0 0.73
1	1	2.62	1.62	0.62 0.62	0 0.38
10	1	20.91	10.91	0.92 0.91	0 0.08
100	1	200.99	100.99	0.99 0.99	0 0.01
0.1	10	1.15	1.05	0.1 0.10	0 0.91
1	10	4.70	3.70	0.27 0.27	0 0.73
10	10	26.18	16.18	0.62 0.62	0 0.38
100	10	209.16	109.16	0.92 0.92	0 0.08
0.1	100	3.31	3.21	0.03 0.03	0 0.97
1	100	11.51	10.51	0.09 0.09	0 0.91
10	100	47.02	37.02	0.27 0.27	0 0.73
100	100	261.80	161.80	0.62 0.62	0 0.38

FILTER 4 (θ,θ_S,D): D_N = 1, T = 0.25, ϵ = 0.00001

Q_d	R	M_θ	P_θ	K	Poles
0.1	0.1	1.01	0.38	1.15 -1.45 0.79	0.42 ± 0.17j 0
1	0.1	3.36	1.41	1.14 -0.81 0.93	0 0.08 0.78
10	0.1	23.46	10.93	1.07 -0.30 0.99	0 0.01 0.92
100	0.1	210.28	102.63	1.02 -0.10 0.98	0 0 0.98
0.1	1	2.25	1.17	0.71 -0.68 0.54	0.65 ± 0.21j 0
1	1	4.55	2.28	0.83 -0.55 0.69	0 0.40 0.77
10	1	24.55	11.88	0.99 -0.28 0.92	0 0.08 0.92
100	1	211.26	103.56	1.01 -0.10 0.99	0 0.01 0.98
0.1	10	7.49	5.07	0.40 -0.26 0.34	0.80 ± 0.16j 0
1	10	10.09	6.60	0.46 -0.25 0.40	0.77 ± 0.09j 0
10	10	31.82	18.25	0.69 -0.19 0.65	0 0.38 0.92
100	10	220.27	112.16	0.94 -0.09 0.92	0 0.08 0.98
0.1	100	31.65	25.34	0.22 -0.09 0.20	0.89 ± 0.10j 0
1	100	35.06	27.75	0.24 -0.09 0.22	0.88 ± 0.09j 0
10	100	64.19	47.10	0.34 -0.08 0.32	0 0.74 0.92
100	100	279.16	168.35	0.64 -0.06 0.63	0 0.38 0.98

FILTER 4 (θ,θ_s,D): D_N = 1, T = 0.5, ε = 0.00001

Q_d	R	M_θ	P_θ	K	Poles
0.1	0.1	2.16	0.63	1.45 -1.17 0.86	0.28 ± 0.25j 0
1	0.1	4.99	1.77	1.31 -0.73 0.95	0 0.09 0.60
10	0.1	27.16	11.80	1.14 -0.30 0.99	0 0.01 0.85
100	0.1	220.79	105.19	1.05 -0.10 0.97	0 0 0.95
0.1	1	4.39	1.85	0.95 -0.59 0.65	0.53 ± 0.27j 0
1	1				
10	1	28.55	12.88	1.06 -0.27 0.93	0 0.08 0.85
100	1	221.86	106.17	1.03 -0.10 0.99	0 0.01 0.95
0.1	10	13.13	7.70	0.55 -0.24 0.44	0.72 ± 0.21j 0
1	10	15.64	9.03	0.59 -0.23 0.47	0.71 ± 0.17j 0
10	10	37.88	20.32	0.76 -0.18 0.67	0 0.39 0.85
100	10	231.75	115.20	0.97 -0.09 0.92	0 0.08 0.95
0.1	100	51.03	37.40	0.32 -0.09 0.27	0.84 ± 0.13j 0
1	100	54.00	39.31	0.32 -0.09 0.28	0.84 ± 0.13j
10	100	81.13	56.18	0.40 -0.08 0.36	0.80 ± 0.01j 0
100	100	296.95	174.88	0.67 -0.06 0.64	0 0.38 0.95

FILTER 5 ($\theta, \theta_{s1}, \theta_{s2}$): $\epsilon = 0.01$

Q_d	R	M_θ	P_θ	K	Poles
0.1	0.1	0.36	0.26	0.62	0.01
				0.62	0.01
				0.62	0.37
1	0.1	3.09	2.09	0.92	0.01
				0.92	0.02
				0.92	0.06
10	0.1	30.09	20.09	0.99	$0.00 \pm 0.1j$
				1.00	
				0.99	0.01
100	0.1	300.09	200.09	0.99	$-0.00 \pm 0.00j$
				1.00	
				0.99	0
0.1	1	0.57	0.47	0.27	0.01
				0.27	0.01
				0.27	0.72
1	1	3.61	2.61	0.62	0.01
				0.62	0.01
				0.62	0.37
10	1	30.91	20.91	0.91	0.01
				0.92	0.02
				0.92	0.06
100	1	300.99	200.99	0.99	$0.00 \pm 0.01j$
				1.00	
				0.99	0.01
0.1	10	1.23	1.13	0.01	0.01
				0.01	0.01
				0.01	0.90
1	10	5.66	4.66	0.27	0.01
				0.27	0.01
				0.27	0.72
10	10	36.11	26.11	0.62	0.01
				0.62	0.01
				0.62	0.37
100	10	309.14	209.14	0.91	0.01
				0.92	0.02
				0.92	0.06
0.1	100	3.35	3.25	0.03	0.01
				0.03	0.01
				0.03	0.97
1	100	12.33	11.33	0.10	0.01
				0.10	0.01
				0.10	0.90
10	100	56.56	46.56	0.27	0.01
				0.27	0.01
				0.27	0.73
100	100	361.13	261.13	0.62	0.01
				0.62	0.01
				0.62	0.37

FILTER 6 ($\theta, \theta_{S1}, \theta_{S2}, D$): $D_N = 1$, $T = 0.25$, $\varepsilon = 0.01$

Q_d	R	M_θ	P_θ	K	Poles
0.1	0.1	2.11	1.01	1.51	$0.42 \pm 0.17j$
				-1.44	
				1.16	0.01
				0.79	0.01
1	0.1	6.08	3.36	1.34	0.01
				-0.81	0.02
				1.15	0.06
				0.93	0.78
10	0.1	37.83	23.46	1.14	$0.00 \pm 0.01j$
				-0.30	
				1.08	0.01
				0.99	0.92
100	0.1	323.18	210.28	1.05	$-0.00 \pm 0.01j$
				-0.10	0
				1.03	0.98
				1.00	
0.1	1	3.90	2.23	0.87	$0.64 \pm 0.21j$
				-0.68	0.01
				0.71	
				0.54	0.01
1	1	7.62	4.53	0.97	0.01
				-0.55	0.01
				0.84	0.39
				0.70	0.77
10	1	39.07	24.55	1.06	0.01
				-0.28	0.02
				1.00	0.06
				0.92	0.92
100	1	324.21	211.26	1.04	$0.00 \pm 0.01j$
				-0.10	
				1.03	0.01
				0.99	0.98
0.1	10	10.51	7.31	0.46	$0.80 \pm 0.16j$
				-0.26	
				0.40	0.01
				0.34	0.01
1	10	14.44	9.97	0.52	$0.77 \pm 0.09j$
				-0.25	
				0.46	0.01
				0.40	0.01
10	10	47.19	31.73	0.74	0.01
				-0.19	0.01
				0.70	0.37
				0.65	0.92
100	10	333.62	220.25	0.96	0.01
				-0.09	0.02
				0.95	0.06
				0.92	0.98

FILTER 6 (θ,θ_{s1},θ_{s2},D): D_N = 1, T = 0.25, ε = 0.01

(Concluded)

Q_d	R	M_θ	P_θ	K	Poles
0.1	100	38.40	30.88	0.25	0.89 ± 0.10j
				-0.09	
				0.22	0.01
				0.20	0.01
1	100	43.01	34.37	0.26	0.88 ± 0.09j
				-0.09	
				0.24	0.01
				0.22	0.01
10	100	82.60	63.46	0.36	0.01
				-0.08	0.01
				0.34	0.73
				0.32	0.92
100	100	394.51	278.40	0.66	0.01
				-0.06	0.01
				0.65	0.37
				0.63	0.98

FILTER 6 ($\theta, \theta_{s1}, \theta_{s2}, D$): $D_N = 1$, $T = 0.5$, $\varepsilon = 0.01$

Q_d	R	M_θ	P_θ	K	Poles
0.1	0.1	5.18	2.16	2.03	0.27 ± 0.25j
				-1.17	
				1.45	0.01
				0.86	0.01
1	0.1	10.27	5.00	1.67	0.01
				-0.73	0.02
				1.32	0.07
				0.95	0.60
10	0.1	46.70	27.16	1.28	0.00 ± 0.01j
				-0.30	0.01
				1.15	
				0.99	0.85
100	0.1	347.39	220.79	1.10	-0.00 ± 0.00j
				-0.10	0
				1.06	0.95
				1.00	
0.1	1	8.75	4.37	1.24	0.52 ± 0.27j
				-0.59	
				0.95	0.01
				0.65	0.01
1	1	13.04	6.88	1.25	0.50 ± 0.03j
				-0.50	
				1.00	0.01
				0.75	0.01
10	1	48.41	28.54	1.19	0.01
				-0.27	0.02
				1.07	0.06
				0.93	0.85
100	1	348.56	221.86	1.09	0.00 ± 0.01j
				-0.10	
				1.05	0.01
				0.99	0.95
0.1	10	20.93	12.97	0.67	0.72 ± 0.21j
				-0.24	
				0.55	0.01
				0.44	0.01
1	10	24.86	15.48	0.70	0.70 ± 0.17j
				-0.23	
				0.59	0.01
				0.48	0.01
10	10	59.75	37.77	0.85	0.01
				-0.18	0.01
				0.77	0.38
				0.67	0.85
100	10	359.31	231.72	1.01	0.01
				-0.09	0.02
				0.97	0.06
				0.92	0.95

FILTER 6 (θ,θ_{s1},θ_{s2},D): D_N = 1, T = 0.5, ϵ = 0.01

(Concluded)

Q_d	R	M_θ	P_θ	K	Poles
0.1	100	67.43	50.05	0.36	0.84 ± 0.14j
				-0.09	
				0.32	0.01
				0.28	0.01
1	100	71.59	53.01	0.37	0.84 ± 0.13j
				-0.09	
				0.33	0.01
				0.29	0.01
10	100	110.22	80.17	0.44	0.01
				-0.08	0.01
				0.40	0.78
				0.36	0.81
100	100				

APPENDIX B

COMPUTER SIMULATION LISTING

Filter 4 (θ,D,θ_s)

```
****CONTINUOUS SYSTEM MODELING PROGRAM****
*****TSS/360 VERSION 1 MODIFICATION 2*****
*********PROBLEM INPUT STATEMENTS*********
  INIT
        THAVE=0.0
        THCCD1=0.0
        TINT=0.0
        THAVD=0.0
        THAVD1=0.0
        TDC=0.0
        GFILO=0.0
        UGD=0.0
        THEST=0.0
        THESTD=0.0
        DESTD=0.0
        GCMD=0.0
        THS1D=0.0
  DYNAM
        THET=INTGRL(TIC,OMEC)
        OMEC=INTGRL(OMIC,T)
        T=(TD-TST+TM)*57.3/JG
        TM=KI*ILIM
        ILIM=LIMIT(ILIMM,ILIMP,I)
        I=(VCPP-VB)*2./R
        VB=KB*UREL
        UREL=OMEG-GAMD
        TST=0.0
        VCPP=PWAG*(VCB-VCO)
        VCO=LIMIT(VCM,VCP,VCCC)
        VCCC=INTGRL(VCCCIC,VCC)
        VCC=LEDLAG(ZCC,PCC,VC)
        VC=LEDLAG(ZC,PC,VFOO)
        VFOO=(VFO+VFB)*GC
        VFO=LIMIT(VFM,VFP,VF)
        VF=CMPXPL(VFIC1,VFIC2,VF1,VF2,VDEMOD)
        VDEMOD=4.*34.*25.*OGO*VF2*VF2/57.3
        OGO=OG+GFILO
        OG=RCALPL(OGIC,OGPP,OGI)
        OGI=INTGRL(OGIIC,GIN)
        GIN=OMEG+GD+GCMD+GN
        GN=GAUSS(1,GYM,GSDEV)
        GD=0.0
        TD=0.0
        JYST=0.0
        VCB=0.0
        VFB=0.0
```

```
      WOG=0.0
      THETA=3600.*THET
      OMEGA=3600.*OMEG
      THCCD=INTGRL(0.0,THET)
PROCED THAV,THCCD1=BLOCKA(TINT,TCCD,TIME,THCCD)
      IF(TIME-TINT)1,2,2
    1 GO TO 3
    2 THAV=(THCCD-THCCD1)/TCCD
      THCCD1=THCCD
      TINT=TINT+TCCD
      GO TO 3
    3 CONTINUE
ENDPRO
      CCDN=GAUSS(1,CCDM,CSDEV)
      THAVE=THAV+CCDN
PROCED THAVD,GFILO,GCMD=BLOCKG(TDC,TIMP,TIME,FG1,FG2,THAVE,JYST,OG)
      IF(TIME-TDC)4,5,5
    4 GO TO 6
    5 DOG=OG-OGD
      THAVD=THAVD1
      ERROR=JYST+THAVD-THESTD
      THEST=FG1*ERROR+THESTD+DOG
      GFILO=THEST-OG
      DEST=ERROR*FG2+DESTD
      GCMD=-1.0*DEST
      THAVD1=THAVE
      THESTD=THEST
      DESTD=DEST
      OGD=OG
      TDC=TDC+TIMP
      GO TO 6
    6 CONTINUE
ENDPRO
TITLE  AIROSCOPE I-1 ELVATION SIMULATION
TIMER DELT=.005,FINTIM=25.,PRDEL=.02,OUTDEL=.02
METHOD RKSFX
PRINT THETA,OMEGA,GCMD,OGO,GN,THAVE,THAVD,GFILO
INCON VCCCIC=0.0
INCON TIC=0.0,OMIC=0.0
INCON VFIC1=0.0,VFIC2=0.0
INCON OGIC=0.0,OGIIC=0.0
PARAM JG=31.,KI=1.79,KB=.0424,R=4.
PARAM ILIMM=-10.,ILIMP=10.
PARAM VCM=-15.,VCP=15.
PARAM PWAC=10.
PARAM ZC=.1,PC=.00476
PARAM ZCC=.1,PCC=.00288
PARAM CC=2.27
PARAM VFM=-15.,VFP=15.
PARAM VF1=.39,VF2=376.
PARAM OGM=-6.,OGP=6.
PARAM OGPP=.0025
PARAM GYM=6.0,GSDEV=.00021
PARAM CCDM=0.0,CSDEV=.002788
PARAM FG1=.1
PARAM FG2=-.55
PARAM TCCD=.25
PARAM TIMP=.4
END
STOP
```

FILTER4

REFERENCES

1. Deboo, G. J.; Parra, G. T.; and Hedlund, R. C.: AIROscope Stellar Acquisition. Proceedings of the Telescope Systems for Balloon-Borne Research Symposium, NASA TM X-62,379, 1974.
2. Murphy, J. P.; and Lorell, K. R.: The AIROscope Pointing and Stabilization System. Proceedings of the Telescope Systems for Balloon-Borne Research Symposium, NASA TM X-62,379, 1974.
3. Bryson, A. E., Jr.; and Kortüm, W.: Estimation of the Local Attitude of Orbiting Spacecraft. *Automatica*, vol. 6, 1971.
4. Farrenkopt, R. L.: Generalized Results for Precision Attitude Reference Systems Using Gyros. AIAA Mechanics and Control of Flight Conference, Anaheim, Calif., Aug. 1974.
5. Katz, P.; and Powell, J. D.: Selection of Sampling Rate for Digital Control of Aircrafts. SUDAAR No. 486, Sept. 1974.
6. Murphy, J. P.; Lorell, K. R.; and Swift, C. D.: A Computer Aided Telescope Pointing System Utilizing a Video Star Tracker. NASA TM X-73,079, Dec. 1975.
7. Saloman, P. M.; and Goss, W. C.: A Microprocessor Controlled CCD Star Tracker. AIAA 14th Aerospace Sciences Meeting, Washington, D. C., Jan. 1976.
8. Sage, A. P.; and Melsa, J. L.: *Estimation Theory with Applications to Communications and Control*, McGraw-Hill Book Co., Inc., 1971.
9. System 360 Continuous System Modeling Program (360A-CX-16X). User's Manual, IBM Application Program Note, H20-0367-1, 1967.
10. Bryson, A. E., Jr.; and Ho, Y. C.: *Applied Optimal Control*, Blaisdell Publishing Co., 1969.